

University of Glasgow  
Department of Electronics and Electrical Engineering

# Monolithic Integration of Semiconductor Ring Lasers

Sándor Fürst

June 2008

A thesis submitted to the University of Glasgow in accordance with the requirements for the degree of Doctor of Philosophy in the Faculty of Engineering, Department of Electronics and Electrical Engineering.

## Abstract

The interest in semiconductor ring lasers (SRLs) has been steadily growing in the last few years because of several unique properties such as ultrafast directional bistability, stable single mode operation and potential for integration. However, most of the mode dynamical behavior as well as the optimum device design are still far from a complete understanding. This thesis reports on the design, technological development and characterization of SRLs emitting at  $1.55\ \mu\text{m}$ , which are monolithically integrated with a number of other optical elements such as tunable couplers, optical amplifiers, Bragg reflectors and distributed feedback lasers (DFBs). A detailed analysis on the device design is presented with particular emphasis on its robustness with respect to fabrication tolerances and to the optical feedback from the output waveguides. The complete processing technology is developed with a focus on selective dry etching to achieve very accurate control of the waveguide bending losses. Three completely novel and monolithically integrated SRL devices are fabricated and characterized. The first is a master-slave device based on the monolithic integration of an SRL with a DFB that shows highly efficient cavity enhanced four-wave mixing up to detuning frequencies of 1.5 THz. In a second geometry, a Bragg reflector defined on one of the output waveguides selects the lasing mode of the SRL. The device shows world-record wavelength switching speeds as low as 450 ps and strong immunity to thermal fluctuations of the grating. The third device is an SRL with tunable couplers for active Q-switching applications. Pulses as short as 120 ps at a repetition rate of 1.8 GHz are obtained by injecting only a few mA of current into the tuning section.

## Acknowledgments

Foremost, I would like to thank my supervisor Dr. Marc Sorel. He has guided and supported me throughout these years, he always managed to inspire and motivate me. His supervisory skills, passion for science and ultra fast thinking are second to none. Next I would like to thank all the support from my lovely fiancée Krisz. Without her I would be definitely less today. I owe the biggest thank to my family, they never questioned my decisions and they always gave their maximum support wholeheartedly. Also thanks to my second supervisor, Prof. Dave Hutchings.

During these years I was fortunate to get to know so many nice, knowledgeable and helpful people: Francesca showed me the tricks and tips of fabrication. Barry always managed to cheer me up but he also had very helpful advices – no matter if my question was on ales, on science or the combination of the two. Apart from being a very friendly chap, asking Corrie have always resulted in getting ten questions back, which twisted my way of thinking onto the correct path. Also thanks to Steven and Michael for their valuable help and friendship. I need to thank Gaga, we have known each other and been friends for many years. With us it is utterly true that four eyes see more than two: collaboration with him results in more efficient, enjoyable, faster and better work.<sup>1</sup>

I need to dedicate a separate paragraph to all the Italian friends, not because they deserve it but because they are so many. These people were always friendly, cheered me up, distracted me from work and they made these years unforgettable: Vito, Gianmauro, 2 Micheles, Davide, Oberdan, Marco, Carla, Luigi. The list would not be complete without mentioning the others: Jerome, Franziska, Élodie, Janis, Ravi, Ines, Julia, Dadou, Virginie. Thank you all for the good memories!

Thanks for the technical staff of the University of Glasgow. Their knowledge and experience is the biggest strength of the department. Thanks for all the collaborating partners as well, I think this network has qualities which are second to none and this collaboration will be fruitful for many years to come, therefore special thanks to Alessandro Sciré, Salvador Balle, Antonio Perez, Guido Giuliani, Siyuan Yu and Jan Danckaert.

Even though I do not dare to put down their name in writing, I would also thank the metal bands whose music helped me through the writing up stage.

Finally, I would acknowledge EPSRC for financial support of the RAPTOR project.

---

<sup>1</sup>Of course there is a price to pay in our free time, our fuel intake (i.e. pálinka) gets increased a lot.

# Declaration and Copyright

## **Declaration**

Unless otherwise acknowledged, the content of this thesis is the original and sole work of the author. No portion of this work has been submitted by the author in support of an application for any other degree or qualification, at this or any other university or institute of learning. The views expressed in this thesis are those of the author, and not necessarily those of the University of Glasgow.

Sándor Fürst

## **Copyright**

Attention is drawn to the fact that the copyright of this thesis rests with the author. This copy of the thesis has been supplied on condition that anyone who consults it is understood to recognize that its copyright rests with the author and that no quotation from the thesis and no information derived from it may be published without the prior written consent of the author.

# Contents

<b>1</b>	<b>Introduction</b>	<b>1</b>
1.1	Semiconductor ring lasers . . . . .	1
1.2	Literature review . . . . .	3
<b>2</b>	<b>Device design</b>	<b>7</b>
2.1	Material and waveguides . . . . .	7
2.1.1	Material selection . . . . .	7
2.1.2	Horizontal confinement . . . . .	8
2.1.3	Shallow etched waveguide design . . . . .	11
2.2	Couplers . . . . .	13
2.2.1	Available coupling techniques . . . . .	13
2.2.2	Evanescent field couplers . . . . .	14
2.2.3	Fabrication tolerance . . . . .	17
2.2.4	Tunability . . . . .	19
2.3	Effect of bending loss . . . . .	22
2.4	Threshold current and quantum efficiency . . . . .	22
2.5	Distributed feedback mirror . . . . .	26
<b>3</b>	<b>Fabrication</b>	<b>28</b>
3.1	Overview of the process steps . . . . .	28
3.2	Sample preparation . . . . .	29
3.2.1	Cleaning techniques . . . . .	29
3.2.2	Marker definition . . . . .	31
3.3	Quantum well intermixing . . . . .	33
3.3.1	Sputtered silica QWI . . . . .	33
3.3.2	QWI modulation . . . . .	36
3.3.3	QWI related problems . . . . .	36
3.4	Lithography . . . . .	38

3.4.1	Automated layer generation . . . . .	38
3.4.2	Electron beam lithography . . . . .	39
3.4.3	Proximity error correction . . . . .	40
3.5	Dry etching . . . . .	43
3.5.1	Selective reactive ion etching of InP . . . . .	44
3.5.2	Effect of RIE lag . . . . .	45
3.6	Contact metallization . . . . .	49
3.7	Final steps . . . . .	51
3.8	Full process flow chart . . . . .	52
<b>4</b>	<b>Basic characterization</b>	<b>55</b>
4.1	Material characterization . . . . .	55
4.1.1	Basic material properties . . . . .	55
4.1.2	Cw characteristic of RWG lasers. . . . .	57
4.1.3	Waveguide loss/gain . . . . .	58
4.2	Bending loss assessment . . . . .	60
4.2.1	Half ring lasers . . . . .	60
4.2.2	Cw characterization of SRLs with different radii . . . . .	62
4.3	Couplers . . . . .	63
4.3.1	Passive couplers . . . . .	63
4.3.2	Tunability . . . . .	64
4.4	DFB lasers . . . . .	68
4.4.1	Cw characterization . . . . .	68
4.4.2	Tuning properties . . . . .	68
4.5	Operating regimes of semiconductor ring lasers . . . . .	72
4.5.1	Directionality . . . . .	72
4.5.2	Modal properties . . . . .	76
4.6	Conclusions . . . . .	76
<b>5</b>	<b>Feedback in SRLs</b>	<b>79</b>
5.1	Transfer function of SRLs . . . . .	79
5.1.1	Measuring the transfer function . . . . .	79
5.1.2	Measurement analysis . . . . .	82
5.1.3	Asymmetric four port device . . . . .	84
5.1.4	Effect of amplified spontaneous emission noise . . . . .	86
5.2	Mode selection in SRLs . . . . .	87
5.2.1	Modal thresholds . . . . .	88

5.2.2	Doublets in the bidirectional regime . . . . .	90
5.2.3	Doublet evolution versus mode number . . . . .	92
5.2.4	Coupled cavity effect in large SRLs . . . . .	93
5.3	Feedback effect on operational regimes . . . . .	94
5.4	Mode locking induced by feedback . . . . .	99
5.5	Multi-wavelength stability . . . . .	100
5.6	Conclusions . . . . .	105
<b>6</b>	<b>Integrated SRLs</b>	<b>106</b>
6.1	SRLs subjected to weak external injection . . . . .	106
6.1.1	Cavity enhanced FWM . . . . .	107
6.1.2	Unidirectional mode-locking . . . . .	109
6.1.3	Integration of an SRL and a DFB . . . . .	112
6.1.4	Master-slave configuration . . . . .	114
6.1.5	Applications . . . . .	116
6.2	Rapid tunability by wavelength selective feedback . . . . .	120
6.2.1	Design and cw characterization . . . . .	120
6.2.2	High speed performance . . . . .	124
6.2.3	Applications . . . . .	125
6.3	Q-switching in SRLs . . . . .	128
6.3.1	Tunable coupler devices . . . . .	128
6.3.2	Q-switched operation . . . . .	133
6.3.3	Applications . . . . .	135
<b>7</b>	<b>Summary and conclusions</b>	<b>137</b>
7.1	Summary and Conclusion . . . . .	137
7.2	Future work . . . . .	139
<b>A</b>	<b>List of used materials</b>	<b>141</b>
<b>B</b>	<b>Basic equations for semiconductor lasers</b>	<b>143</b>
<b>C</b>	<b>Measurements on the linewidth enhancement factor</b>	<b>145</b>
<b>D</b>	<b>List of equipment used</b>	<b>148</b>
<b>E</b>	<b>Acronyms</b>	<b>150</b>

# List of Figures

2.1	IQE grown wafer structure mainly used to fabricate ring lasers. . .	8
2.2	Three options for waveguiding in SRLs and their related problems. .	9
2.3	Effective refractive index difference as a function of the upper cladding thickness at the etched areas. . . . .	11
2.4	Modal loss for the fundamental $TE_{00}$ and the first order $TE_{01}$ modes as a function of the waveguide width. . . . .	12
2.5	Mode profile for $2\ \mu\text{m}$ wide waveguide when it is etched down to the core. . . . .	13
2.6	Schematic of available coupling techniques. . . . .	14
2.7	Illustration of an evanescent field coupler with part of the ring cavity and outputs. . . . .	15
2.8	Result of a 3D simulation of $1\ \mu\text{m}$ gap coupler on the IQE material. .	16
2.9	Coupling length corresponding to different gap widths between the waveguides. . . . .	16
2.10	Simulated effective refractive index difference as a function of upper cladding thickness and output coupling ratio on a directional coupler for two different gaps. . . . .	17
2.11	Coupling ratio as a function of length with fabrication tolerances. .	19
2.12	Simulation results on the coupling ratio for different coupler lengths and the concept of tunability. . . . .	21
2.13	Coupling ratio as a function of coupler length for different group index differences. . . . .	21
2.14	Simulated bending loss as a function of bending radius for different etching depths. . . . .	23
2.15	A typical configuration of a racetrack cavity SRL with the different loss factors. . . . .	23
2.16	Calculated ring laser performance vs. ring radius for different coupler lengths and upper cladding thicknesses. . . . .	24

2.17	Threshold currents and external quantum efficiencies of racetrack shaped SRLs varying the radius of the ring and the length of the coupler to keep the cavity length fixed. . . . .	25
2.18	Simulated stop-band of a 2D grating. . . . .	27
3.1	Illustration on the main fabrication steps. . . . .	30
3.2	Alignment accuracy of gold and etched markers. . . . .	32
3.3	Illustration of the sputtered silica QWI technique. . . . .	34
3.4	Illustrating the PL measurement setup, and PL spectra taken from as-grown and annealed samples. . . . .	35
3.5	Measured PL peak shift as a function of annealing with the corresponding temperature profile. . . . .	35
3.6	Optical micrograph of patterned sputtered silica on top of a sample. . . . .	37
3.7	Example on automated mask generation. . . . .	39
3.8	Residual HSQ resist thickness after development at different doses. . . . .	41
3.9	Energy density in a PMMA resist on top of semiconductor after electron beam exposure. . . . .	42
3.10	Illustration of PEC and an SEM image of a PMMA grating with poor contrast resulting from proximity error. . . . .	43
3.11	Optical micrograph of an underdeveloped alignment cross showing dose assignment by PEC. . . . .	44
3.12	SEM image of etched waveguide and gratings using the optimized process. . . . .	46
3.13	AFM trace about etched surface when etching reached the stop-etch layer. . . . .	46
3.14	SEM image of a (not fully) etched 300 nm-gap coupler showing the effect of RIE lag. . . . .	47
3.15	Etch depth inside coupler gaps as a function of coupler gap width an etch time. . . . .	48
3.16	Cross-sectional SEM image of a grating and contrast enhanced image showing the etch profile inside the recess of the grating. . . . .	48
3.17	Optical micrograph of TLM patterns on InGaAs. . . . .	50
3.18	Specific contact resistance as a function of annealing temperature. . . . .	51
3.19	Schematic of the lasers glued to a sub-mount. . . . .	52
3.20	Final FP laser facet. . . . .	53
3.21	Full process flow chart for the fabrication of SRLs. . . . .	54

4.1	Threshold current density as a function of cavity length for the material MR2256. . . . .	57
4.2	LI characteristic of a 1 mm long FP laser as a function of temperature. . . . .	58
4.3	Gain (or loss) as a function of waveguide bias extracted from three section laser measurements. . . . .	59
4.4	SEM image of a half ring laser without contact metallization and schematic of devices. . . . .	60
4.5	Measured and simulated half ring laser thresholds and external quantum efficiencies. . . . .	61
4.6	Threshold currents of half ring lasers fabricated on the IQE material. . . . .	62
4.7	Threshold current and lasing wavelength at $1.1 \times I_{th}$ as a function of SRL radii. . . . .	63
4.8	SEM image of a point coupler designed for coupling ratio measurements. . . . .	64
4.9	Setup for transmission measurements. . . . .	64
4.10	Measured coupling ratios and designed values for different coupler length. . . . .	65
4.11	Coupling ratio as a function of the tuning current. . . . .	66
4.12	Coupling ratio as a function of the tuning voltage. . . . .	67
4.13	Designed and measured lasing wavelength of DFBs as a function of pitch size. . . . .	69
4.14	Optical spectrum of a DFB. . . . .	69
4.15	Tunability of DFBs as a function of lasing wavelength. . . . .	70
4.16	Modulation response of a DFB at a frequency of 1 GHz. . . . .	71
4.17	Setup used for testing SRLs. . . . .	72
4.18	LI curves of a 300 $\mu\text{m}$ radius ring laser with one 300 $\mu\text{m}$ long coupler for the two directions. . . . .	73
4.19	Simulated operating regimes of SRLs. . . . .	75
4.20	Wavelength distribution as a function of wavelength and current. . . . .	77
4.21	directional extinction ratio and side mode suppression ratio as a function of ring current. . . . .	77
5.1	Optical micrograph of a 300 $\mu\text{m}$ -radius ring laser with the corresponding measurement setup. . . . .	80
5.2	Detected power at port #3 and #4. . . . .	81
5.3	Zoom in of the measured lines. . . . .	81

5.4	Transfer functions of unperturbed ring, ring with a strong point reflection, ring with a weak point reflection and ring coupled to a weak Fabry-Perot filter. . . . .	82
5.5	Theoretical results for the power collected at port # 3. . . . .	84
5.6	Transmission measurement of a cavity line of an asymmetric four port device. . . . .	85
5.7	Doublet separation as a function of the wavelength. . . . .	85
5.8	Theoretical detuning between doublets. . . . .	86
5.9	Measured envelope signal at port #4 for different bias currents. . .	87
5.10	Measured envelope signal at port #3 for different bias currents. . .	88
5.11	LI curve and corresponding lasing wavelength. . . . .	89
5.12	Illustrative figure on the two solution branches imposed by cavity defects. . . . .	90
5.13	Doublet evolution in the bidirectional regime. . . . .	91
5.14	Optical spectra of a 300 $\mu\text{m}$ -radius SRL for the two directions. . . .	92
5.15	Heterodyne measurement of the modes of the lasing direction. . . .	93
5.16	Wavelength map of a 5.2 mm cavity length SRL. . . . .	94
5.17	Average jump in wavelength for different SRLs. . . . .	95
5.18	Directional extinction ratio versus symmetric feedback. . . . .	96
5.19	LI curve when a current of 10.5 mA is injected into both of the output waveguides. . . . .	97
5.20	Operational regimes as a function of ring current and change in feedback level. . . . .	98
5.21	RF spectra measured in Region 4. . . . .	98
5.22	RF and optical spectra of the two directions under symmetric feedback. 100	
5.23	Mode locking map as a function of the current injected into the output arms. . . . .	101
5.24	RF and optical spectra of the two directions at a current of 16.9 mA, 142 mA and 12.5 mA, injected into the CW output, the ring and the CCW output, respectively. . . . .	101
5.25	Examples of RF spectra under strong feedback. . . . .	102
5.26	Probability of switching into the CW direction, when the current is quickly increased. . . . .	103
5.27	Stable wavelengths and directions versus ring current. . . . .	104
5.28	Optical microscope image of a folded mode-locked ring laser. . . . .	104

6.1	Optical micrograph of the 34.5 GHz FSR ring laser and the corresponding experimental setup used to measure the FWM signal. . . .	107
6.2	Injection into the 43 <sup>rd</sup> mode away from the lasing peak (a detuning of 1.53 THz, 12.5 nm) gives a visible conjugate FWM signal. . . .	108
6.3	Measured power of the FWM signal as a function of detuning from the ring lasing mode. . . . .	109
6.4	Measured and fitted conversion efficiency as a function of detuning.	110
6.5	Cascaded locking of several cavity modes of the SRL by FWM. . . .	110
6.6	Optical and RF spectra when the injection is tuned to the adjacent cavity mode of the main lasing wavelength. . . . .	111
6.7	SEM image of an SRL integrated to a DFB. . . . .	112
6.8	Optical spectra of the integrated SRL and DFB. . . . .	113
6.9	The resulting optical spectrum when the ring and DFB are operated together. . . . .	113
6.10	Optical injection locking map. . . . .	115
6.11	RF spectra in the chaotic regime. . . . .	116
6.12	Optical spectra with two color injection showing simultaneous conversion of multiple input wavelengths. . . . .	118
6.13	SEM image of the ring laser monolithically integrated next to a DBR.	121
6.14	Grating assessment. . . . .	121
6.15	Subthreshold wavelength map taken from output1 as a function of the DBR current. . . . .	122
6.16	Optical spectra at 2 mA, 3 mA and 5 mA of DBR current. . . . .	123
6.17	Lasing wavelength, DBR peak reflection wavelength and SMSR as a function of DBR current. . . . .	123
6.18	Setup to for high speed measurements. . . . .	124
6.19	Measured time trace of switching from $\lambda_1 = 1560.4$ nm to $\lambda_2 = 1559.9$ nm. . . . .	125
6.20	Optical spectrum during modulation when four wavelengths were addressed. . . . .	126
6.21	Measured and simulated threshold currents of 200 $\mu$ m ring radius SRLs with different coupler lengths. . . . .	129
6.22	LI curves of the 150 $\mu$ m-long coupler device at different coupler currents. . . . .	130
6.23	Measured and simulated threshold currents. . . . .	130
6.24	Output power as a function of coupler current when the SRL current is fixed. . . . .	131

6.25	Simulated output power as a function of coupling coefficient for different ring currents. . . . .	133
6.26	SEM image of the device, used for Q-switching experiments. . . . .	134
6.27	Optical spectra and time trace of 240 MHz switching . . . . .	134
6.28	Time traces of Q-switching experiments. . . . .	135
C.1	Measured frequency response for varying SRL current. . . . .	146
C.2	Measured linewidth enhancement factor vs. SRL current . . . . .	147

# List of Tables

2.1	Comparison of the three available coupling techniques. . . . .	14
4.1	Summary of threshold current densities obtained from broad area laser measurements. . . . .	56
A.1	Material <i>3186</i> , a $1.3\ \mu\text{m}$ wafer for fabrication assessment. . . . .	141
A.2	Structure of the $1.55\ \mu\text{m}$ wafers <i>2032</i> , <i>2254</i> and <i>2256</i> used for fabrication assessment and early results on ring lasers. . . . .	142

# List of publications

## Journal papers

S. Fürst and M. Sorel, “Cavity-enhanced four-wave mixing in semiconductor ring lasers,” *IEEE Photonics Technology Letters* **20**(5), pp. 366–368, 2008.

S. Fürst, S. Yu, and M. Sorel, “Fast and digitally wavelength-tunable semiconductor ring laser using a monolithically integrated distributed Bragg reflector,” submitted to *IEEE Photonics Technology Letters*, 2008.

S. Fürst, A. Perez S., A. Scire, S. Balle, and M. Sorel, “Modal structure, directional and wavelength jumps of integrated semiconductor ring lasers: Experiment and Theory,” submitted to *Applied Physics Letters*, 2008.

S. Fürst and M. Sorel, “Q-switching in semiconductor ring lasers,” in preparation, 2008.

## Conference publications

S. Fürst, M. Sorel, A. Scirè, G. Giuliani, and S. Yu, “Technological challenges for cw operation of small-radius semiconductor ring lasers,” in *Photonics Europe*, (Strasbourg, France), 3–7 April, 2006.

S. Fürst, C. Farmer, L. Hobbs, R. DeLaRue, and M. Sorel, “Native oxidation of aluminum-containing III-V compound layers for increased current and optical confinement in semiconductor lasers,” in *The 19th annual meeting of the IEEE Laser and Electro-Optic Society*, (Montreal, Canada), 28 October – 3 November, 2006.

S. Fürst and M. Sorel, “Four-wave mixing in semiconductor ring lasers subjected to optical injection,” in *European Semiconductor Laser Workshop*, (Berlin, Germany), 14–15 September, 2007.

S. Fürst, G. Mezösi, and M. Sorel, “Semiconductor micro-ring lasers,” in *Semiconductor and Integrated Optoelectronics*, (Cardiff, Wales, UK), 31 March – 2 April, 2008.

S. Fürst, G. Mezösi, S. Yu, and M. Sorel, “Monolithic integration of semiconductor ring lasers with distributed Bragg gratings,” in *Conference on Lasers and Electro-Optics*, (San Jose, CA, USA), 4–9 May, 2008.

S. Fürst, S. Yu, and M. Sorel, “Wavelength tunability of an integrated semiconductor ring laser with sub-ns switching time,” in *International Semiconductor Laser Conference*, (Sorrento, Italy), **WB8**, 14–18 September, 2008.

### Other publications

G. Giuliani, M. Sorel, S. Fürst, A. Scire, S. Yu, and J. Danckaert, “Laser a semiconduttore con cavità ad anello per la realizzazione di memorie ottiche,” in *Fotonica 2007*, (Mantova, Italy), **B6.4**, 21–23 May 2007.

G. Giuliani, F. Bragheri, S. Fürst, M. Sorel, A. Scire, J. Danckaert, and S. Yu, “Optically addressable bistable memory based on semiconductor ring lasers: experimental results,” in *9th International Conference on Transparent Optical Networks — ICTON 2007*, (Rome, Italy), **Mo.C2.4**, 1–5 July 2007.

S. Yu, Z. Wang, G. Giuliani, S. Fürst, and M. Sorel, “Optically triggered monostable and bistable flip-flop operation of monolithic semiconductor ring laser,” *Photonics in Switching 2007*, (San Francisco, CA, USA), 19–22 August 2007.

S. Yu, Z. Wang, S. Fürst, and M. Sorel, “All-optical data processing using directional monostability in semiconductor ring laser,” in *European Conference on Optical Communication 2007*, (Berlin, Germany), **P039**, 16–20 September 2007.

G. Giuliani, S. Yu, Z. Wang, G. Yuan, B. Li, M. I. Memon, S. Fürst, and M. Sorel, “All-optical flip-flop and digital inverter functions using a monolithic semiconductor ring laser,” in *European Conference on Optical Communication 2007*, (Berlin, Germany), **P046**, 16–20 September 2007.

M. J. L. Vidal, F. Bragheri, A. Trita, G. Giuliani, S. Fürst, M. Sorel, and S. Yu, “Semiconductor micro-ring lasers for bistable all-optical memory: tech-

nology and experimental results,” in *European Semiconductor Laser Workshop*, (Berlin, Germany), 14–15 September, 2007.

G. Giuliani, M. J. L. Vidal, F. Bragheri, S. Fürst, M. Sorel, A. Scire, J. Danckaert, and S. Yu, “Bistable digital all-optical memory based on semiconductor micro-ring laser,” in *2nd European Optical Society Topical Meeting: Optical Microsystems — OMS 2007*, (Capri, Italy), 30 September – 3 October 2007.

Z. Wang, G. Yuan, S. Yu, G. Giuliani, S. Fürst, and M. Sorel, “Optically monostable operation of a monolithic semiconductor ring laser using an external optical injection,” in *Asia-Pacific Optical Communications — APOC 2007*, (Wuhan, China), **6783-69**, 1–5 November 2007.

A. Scire, A. Perez, S. Fürst, J. Javaloyes, R. Zambrini, M. Sorel, and S. Balle, “Semiconductor ring laser modelling,” in *Workshop on Nonlinear Dynamics in Semiconductor Lasers*, (Berlin, Germany), 19–21 November 2007.

M. J. L. Vidal, S. Fürst, G. Mezósi, M. Sorel, A. Perez, A. Scire, S. Balle, and G. Giuliani, “Experimental and theoretical analysis of the optical spectra of directionally bistable semiconductor ring lasers,” in *SPIE Photonics Europe 2008*, (Strasbourg, France), **6997-77**, 7–10 April 2008.

A. Trita, S. Fürst, G. Mezósi, M. Sorel, M. J. L. Vidal, S. Yu, F. Bragheri, I. Cristiani, S. Yu, Z. Wang, and G. Giuliani, “Time-domain response to ps optical pulse trigger of an all-optical flip-flop based on semiconductor ring laser” in *SPIE Photonics Europe 2008*, (Strasbourg, France), **6997-76**, 7–10 April 2008.

K. Thakulsukanant, B. Li, S. Yu, S. Fürst, and M. Sorel, “All-optical label swapping using bistable semiconductor ring laser,” in *Conference on Lasers and Electro-Optics — CLEO 2008*, (San Jose, CA, USA), **CThH7**, 4–9 May 2008.

G. Mezósi, S. Fürst, and M. Sorel, “Active Q-switching in semiconductor ring lasers,” in *Conference on Lasers and Electro-Optics — CLEO 2008*, (San Jose, CA, USA), **CWL5**, 4–9 May 2008.

A. Trita, G. Mezósi, F. Bragheri, S. Yu, S. Fürst, I. Cristiani, W. Elsaesser, and M. Sorel, “Switching time and response to ps optical trigger pulse of

all-optical flip-flop based on a monolithic semiconductor ring laser,” in *International Semiconductor Laser Conference*, (Sorrento, Italy), **TuC4**, 14–18 September, 2008.

G. Mezósi, M. J. Strain, M. Sorel, S. Fürst, S. Yu, and Z. Wang, “Directional bi-stability in micro-ring and micro-disk lasers,” in *International Semiconductor Laser Conference*, (Sorrento, Italy), **TuC5**, 14–18 September, 2008.

M. Zanola, G. Mezósi, S. Fürst, M. Sorel, and G. Giuliani, “Dynamic characterization of semiconductor ring lasers: frequency response and linewidth enhancement factor,” in *International Semiconductor Laser Conference*, (Sorrento, Italy), **P27**, 14–18 September, 2008.

A. Perez, S. Fürst, A. Scire, J. Javaloyes, S. Balle, and M. Sorel, “Modal structure of integrated semiconductor ring lasers with output waveguides,” in *International Semiconductor Laser Conference*, (Sorrento, Italy), **P28**, 14–18 September, 2008.

A. Trita, G. Mezósi, F. Bragheri, J. Yu, S. Fürst, W. Elssser, I. Cristiani, M. Sorel, and G. Giuliani “Dynamic operation of all-optical flip-flop based on a monolithic semiconductor ring laser,” submitted to *European Conference on Optical Communication 2008*, (Brussels, Belgium), 21–25 September 2007.

# Chapter 1

## Introduction

### 1.1 Semiconductor ring lasers

This thesis investigates the design, technology development, characterization and monolithic integration of SRLs emitting at  $1.55\ \mu\text{m}$ . Conventional Fabry-Perot (FP) lasers or DFBs only support standing-wave longitudinal modes, while SRLs operate in a traveling wave regime and support two lasing counter-propagating modes. For decades, the coexistence of two directional modes inside the ring cavity has been regarded as a negative feature because of the potential modal instabilities and the added degree of complexity in the modeling of the devices. However, it has been recently discovered that the gain competition between the two counter-propagating traveling waves in SRLs leads to stable unidirectional operation, in which only one of the directions is selected while the other becomes strongly suppressed. In this scenario, the SRL behaves as an optical bistable in the two lasing directions, since the lasing direction can be set or switched by an external optical signal. Since the directional mode switching does not involve major changes in the carrier population inversion, the switching speed is much faster than the carrier recombination time that sets a major limitation in the majority of the switching or modulation processes. This effect has triggered a lot of renewed interest in SRLs for applications in all-optical signal processing and optical memories. Furthermore, SRLs do not require cleaved facets and are therefore very attractive for monolithic integration into photonic integrated circuits (PICs). All these features enable the design of a large variety of novel devices, most of which can not be realized with conventional FP or DFB geometries.

Since SRLs differ quite substantially from FP lasers both in the technology and the design, the first part of the thesis defines a set of design and fabrication

procedures to realize robust devices with good performance and high yield. In particular, the issues related to the bending losses and the output coupling mechanisms are investigated in detail. An extensive part of the work is also devoted to the understanding of the longitudinal modal behaviour of the devices and to its fine structure when the SRL is subjected to weak feedback effects from the output waveguides. The acquired technological and device know-how is used in the last part of the work to fabricate three integrated devices that show the potential of SRLs for designing novel geometries with unique functionalities.

The first geometry consists of the integration of a DFB laser and a SRL, where the DFB optically injects and locks the SRL. Because of the unidirectional behavior of the ring laser, this design is equivalent to a master-slave configuration without the requirement of an optical isolator to isolate the master (DFB) from the slave (SRL). Besides the typical dynamical scenario already reported in bulk master-slave devices such as stable locking, bifurcations, optical chaos and coherence collapse, the device exhibits efficient cavity enhanced four-wave mixing (FWM). This effect is completely novel and allows the generation of very narrow linewidth micro- and millimeter-waves in a simple and integrated manner.

A second device is an integrated rapidly tunable ring laser, consisting of an SRL and a tunable distributed Bragg reflector (DBR) defined on one of the output waveguides of the SRL. The DBR is external to the ring cavity, and it only selects one of the longitudinal modes of the SRL. The concept therefore enables very fast tuning by separating the mechanism (the ring cavity) that defines stable lasing mode frequencies from the tuning mechanism (the grating) that only selects one of these stable frequencies. Furthermore, this concept does not require phase matching sections and provides a device geometry suitable for further integration. The devices show wavelength switching speed below 0.5 ns and a very strong immunity of the lasing wavelength from the thermal fluctuations of the grating.

Another class of devices can be designed by using tunable couplers to control the amount of power extracted from the ring cavity. Here, the quality factor or Q-factor of the laser can be directly controlled, therefore enabling active Q-switching. The first demonstration of active Q-switching in integrated semiconductor lasers is presented in the last part of the thesis.

The thesis is organized in an incremental manner, going from design and fabrication to characterization of single SRLs and integrated devices, thereupon the chapters are organized as follows:

**Chapter 2** presents the SRL design considerations, including selection of material, waveguide design, couplers, gratings. The bending losses that limit the

minimum device dimensions are theoretically investigated as a function of the material layer structure and waveguide geometry. Evanescent field couplers are chosen as the preferred solution for output coupling, and their fabrication tolerances and tunability are presented.

**Chapter 3** reports on the technological development. A selective dry etching technique is developed to minimize bending losses and to achieve precise control over the etching depth. The whole fabrication is discussed in detail where major process development was carried out.

**Chapter 4** introduces preliminary results on basic SRL characterization, bending loss assessment, passive couplers and DFBs.

**Chapter 5** gives an explanation for the peculiar mode selection rules, seen in SRLs. It is shown that the periodic wavelength-switching is caused by reflections coming from the output facets. Operational regimes of SRLs are studied, as well as the effects of feedback.

**Chapter 6** is divided into three main sections, each corresponding to one of the integrated devices previously discussed, namely the integration of an SRL with a DFB, a DBR and a tunable coupler.

## 1.2 Literature review

The very first published ring laser was reported by a research group in California in 1976 and the circular cavity<sup>1</sup> was provided by four cleaved facets providing total internal reflection at the single GaAs/AlGaAs heterojunction/air interface and output beam was obtained by surface grating [1]. Soon after the first truly ring shaped ring laser was also demonstrated by a Tokyo group where rings did not have an output coupler so only scattered emission could be observed [2].

Many attribute the first publication about ring lasers to Liao and Wang because that was the first ring shaped laser with an incorporated y-junction output coupler as well [3,4], however, the idea of integrating SRLs was taken further only ten years later but then by several groups.

---

<sup>1</sup>Throughout the thesis any type of semiconductor laser where the light can propagate in a circular manner will be called ring lasers, i.e.: a self explanatory name like "square ring laser" is referred to a square shaped ring laser.

Thomas Krauss, under the supervision of Peter Laybourn at the University of Glasgow, was working on (first) the y-junction coupler type deep etched devices [5]. He also made shallow etched devices and compared the coupler type configurations: using y-junction, directional and multi-mode interference couplers [6,7,8]. Because ring lasers at the time were regarded as ideal integrated sources the most important factor was to have an efficient output coupler from the ring cavity. He also noted that ring lasers were single mode and it was contributed to the traveling wave operation since they do not suffer from spatial hole burning – the main source of multi-longitudinal behavior in FP lasers. He was the first one as well who draw attention to the multi-mode interference (MMI) couplers and he claimed they are superior in efficiency and insensitivity to fabrication tolerances.

A major contribution to the field of ring lasers comes from Hohimer et. al from the Sandia National Laboratories, Albuquerque, New Mexico [9,10]. At that time it was a general thought that ring lasers can only be forced to unidirectional regime<sup>2</sup> so a few patents are also under his name for ring lasers like the *ying-yang* shaped cavity where one direction is fed back to the other using y-junction couplers [11]. Although, this configuration suffered from intra-cavity back reflections and lasing resulted in a FP type lasing spectrum, he was the first who recognized the problems caused by back-reflections from the output mirrors [12]. Also he recognized that ring lasers can be promising mode-locked sources since the cavity length (and thus the mode-locked frequency) is defined by lithography [13]. The idea later was led further (possibly by his student) to create most likely the first integrated device employing a ring laser to generate millimeter wave electrical signals in an all optical manner [14]. Interestingly a lot later, in 2005, the idea of using the ying-yang shaped geometry was picked up again at the same university where they were using shallow etched, evanescent field output couplers and y-junction couplers in the middle to smoothen out the directional switching [15].

The optoelectronics group at the Cornell University (Ithaca, NY, USA) and their industrial partners (such as IBM and Hewlett-Packard) also took interest in ring lasers. Their research was focused on triangular ring lasers with two deep-etched corner mirrors and the third corner mirror was provided by precise cleaving [16,17]. The research was led by Joseph Ballantyne who also had the idea (with the relevant patent currently under his name) of creating a unidirectional ring laser by placing a so called "optical diode" inside the ring cavity. Tapering out a waveguide and connecting with a normal waveguide results in preferential transmission into one direction; using this technique ring lasers were successfully forced

---

<sup>2</sup>Unidirectional operation caused by cross-gain saturation was not yet discovered at that time.

to unidirectional operation [18]. It is worth to note that the configuration does not break the reciprocity rule since the light is arriving from the tapered section gets reflected to higher order radiating modes outside of the waveguide. However – unlike when using magnetic techniques<sup>3</sup> –, connecting two waveguides with different width is the same as connecting two unmatched transmission lines, which results in a limited suppression of the non-lasing direction, because the roundtrip gain for the two directions stays the same – the power of one mode is radiated out. Later in their research, they discovered that on 20% of their devices they get better<sup>4</sup> unidirectional lasing without using any intracavity forcing mechanisms [19]. The effect was attributed to the fact that they were using multi-mode waveguides and the lasing modes of the two directions are spatially displaced. Today we know that in fact, they were the first ones who discovered unidirectional operation in SRLs that is caused by cross-gain saturation.

The SRL research after Thomas Krauss and Siyuan Yu (he was working on mode-locked ring lasers [20]) was continued by Marc Sorel at the University of Glasgow. He was the first one to recognize that removing feedback from the output facets result in a transition to unidirectional behavior [21]. Furthermore, they were the first ones to measure and investigate several operating regimes of the ring lasers including bidirectional, alternate oscillations and unidirectionality. Moreover they established a model, which predicted the various operating regimes [22, 23, 24].

Back in 1994 Eindhoven based Philips started to fabricate ring lasers as well with early designs on MMI couplers and MMI combining sections to have maximum efficiency [25]. Later on the group called COBRA started to work on integrated ring lasers at the Eindhoven University of Technology. They focused on multiple wavelength generation using monolithic integration of several semiconductor optical amplifiers (SOAs) and an arrayed waveguide grating (AWG) in a ring configuration [26, 27]. They further moved on to make the smallest ring lasers at the time. Coupling two ring resonators resulted in a small and ultra-fast all optical memory element with switching speeds of 20 ps as published in the Nature [28]. Later on the same group started to work on quantum dot (QD) ring lasers due to several advantages as they had already discussed in [28]. The reported large ring lasers show signs of unidirectionality [29], however, the spectrum is not reported, only said that it was similar to the FP ones, so no real conclusion can be made for explaining the low directional extinction ratio (DER) and side mode suppression

---

<sup>3</sup>The magneto-optic based optical isolators or diodes are based on a polarizator and inverting and non-inverting polarization rotation elements.

<sup>4</sup>In terms of the ratio of the powers of the two directions, termed directional extinction ratio.

ratio (SMSR) values.

Apart from the mentioned research groups, a few other single publications came from several companies, universities and research institutes throughout the years. For the sake of completeness, they are reported here as well: Dzurko (Spectra Diode Labs) with similar design as the very first ring laser [30], Han (University of Illinois) with y-junction and square ring lasers from [31, 32], Hansen (Bell Labs) with continuous-wave (cw) and mode-locked operated buried heterostructure ring lasers [33], Kim (Korean Advanced Institute of Science and Technology) with square ring lasers [34] and Griffel (Sarnoff Corporation) with racetrack devices [35] were all contributing to the field of ring laser research.

# Chapter 2

## Device design

Ring lasers can be fabricated on any material system, their unique property comes from unique design, not from material properties. A deciding factor on the device performance – however – mainly comes from the successful merging of available technologies and powerful design. This chapter addresses the design considerations needed to successfully fabricate state of the art ring lasers.

### 2.1 Material and waveguides

#### 2.1.1 Material selection

Owing to the nature of the project, the lasing wavelength was fixed to be in the ITU-C band (1525–1565nm). Given the wavelengths, the material choice is limited to Aluminum ( $\text{Al}_x\text{Ga}_y\text{In}_{1-x-y}\text{As-InP}$ ) or phosphorus ( $\text{Ga}_x\text{In}_{1-x}\text{As}_y\text{P}_{1-y}\text{-InP}$ ) quaternaries. The wafer structures used to fabricate the devices were multiple quantum well (QW) Aluminium quaternaries. Not only were these the only available lasing materials for 1.55  $\mu\text{m}$  operation but they possess a few advantages over standard phosphorus quaternary material. One to mention is the better thermal behavior because of the reduced carrier leakage [36], resulting from a larger conduction band offset:  $\Delta E_c = 0.72\Delta E_g$  in Al-quaternary and  $\Delta E_c = 0.4\Delta E_g$  in phosphorus quaternary. Furthermore, having Al-containing layers in the core region gives rise to a selective dry etch process that plays a significant role in etch-depth control, as will be discussed in detail in Section 3.5.

The latest material to fabricate most of the devices is a commercially available (IQE, see ref. [37]) molecular beam epitaxy (MBE) grown Al quaternary wafer, of which structure is reported in Fig. 2.1. The strained QWs and barriers (layers 6,7

Layer	Material	Group	Repeat	Mole Fraction (x)	Mole Fraction (y)	Strain (ppm)	PL (nm)	Thickness ( $\mu\text{m}$ )	Dopant	Type	CV Level ( $\text{cm}^{-2}$ )
16	GaIn(x)As			0.530		0		0.2000	Zinc	P	> 1.5E19
15	GaIn(x)As(y)P			0.710	0.620	0	1300 +/-50	0.0500	Zinc	P	> 3.0E18
14	InP							0.1000	Zinc	P	> 1.5E18
13	InP							1.5000	Zinc	P	= 1.0E18
12	GaIn(x)As(y)P			0.850	0.330	0	1100 +/-20	0.0200	Zinc	P	= 1.0E18
11	InP							0.0500	Zinc	P	= 7.0E17
10	[Al(x)Ga]In(y)As			0.900	0.530	0		0.0600	Zinc	P	= 4.0E17
9	[Al(x)Ga]In(y)As			0.720 to 0.900	0.530	0		0.0600	Undoped	U/D	
8	[Al(x)Ga]In(y)As			0.440	0.490	-3000	1100 +/-20	0.0100	Undoped	U/D	
7	[Al(x)Ga]In(y)As	1	5	0.240	0.710	12000	1530	0.0060	Undoped	U/D	
6	[Al(x)Ga]In(y)As	1	5	0.440	0.490	-3000	1100 +/-20	0.0100	Undoped	U/D	
5	[Al(x)Ga]In(y)As			0.900 to 0.720	0.530	0		0.0600	Undoped	U/D	
4	[Al(x)Ga]In(y)As			0.900	0.530	0		0.0600	Silicon	N	= 1.0E18
3	[Al(x)Ga]In(y)As			0.860 to 0.900	0.530	0		0.0100	Silicon	N	= 1.0E18
2	InP							0.5000	Silicon	N	= 1.0E18
1	InP							0.3000	Silicon	N	= 3.0E18
SUBSTRATE											

Figure 2.1: IQE grown wafer structure mainly used to fabricate ring lasers.

and 8) are sandwiched between two 60 nm–thick InAlGaAs graded index separate confinement (GRINSC) layers, with the inclusion of two additional 60 nm–thick  $\text{Al}_{0.423}\text{Ga}_{0.047}\text{In}_{0.53}\text{As}$  layers<sup>1</sup>. The role of them is to decrease the leakage of carriers from the QWs back into the InP cladding layers since they have a larger bandgap ( $\sim 1.6\text{ eV}$ ) than the surrounding InP cladding ( $\sim 1.42\text{ eV}$ ) [38]. Increasing Al content in the  $(\text{Al}_x\text{In}_{1-x}\text{As})$  ternary results in larger bandgap, however the layer must be lattice matched to InP, which is met at the condition of  $x = 0.47$ . Such large Aluminum content makes the growth difficult and the layer can be degraded by the humidity of the air. This effect can be significantly reduced by a small addition of Gallium, while keeping the lattices matched [39].

Most of the process development and early devices were fabricated on two other aluminium quaternaries totaling four 2-inch wafers. The structures are reported in Appendix A, one of them in Table A.1 (a  $1.3\ \mu\text{m}$  material) and a  $1.55\text{--}\mu\text{m}$  material whose structure is reported in Table A.2. The latter was also reported in [40, Hin Yong Wong] and all of them were grown at the University of Sheffield.

## 2.1.2 Horizontal confinement

Vertical confinement is given by the material itself<sup>2</sup>, however, horizontal confinement is up to design consideration. Gain guided ring lasers were never fabricated, and this approach was not even considered due to several disadvantages (need for corner mirrors, pulsed operation, not single lateral mode lasing, etc.). For index guiding, three wave guiding options can be considered: shallow etched or ridge wave-guides (RWGs), deep etched or rib waveguides, and buried heterostructure

<sup>1</sup>For further reference when I talk about *core*, all the Aluminum containing layers are included.

<sup>2</sup>Thanks to the very fortunate material properties of compound semiconductors.

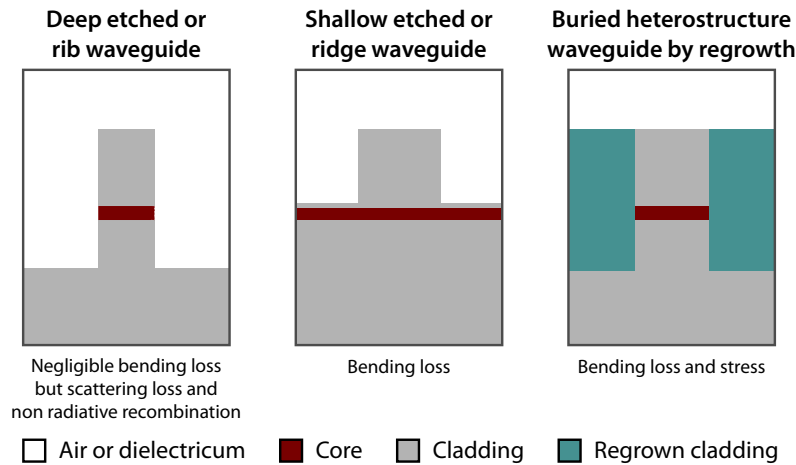


Figure 2.2: Three options for waveguiding in SRLs and their related problems.

waveguides using regrowth as illustrated in Figure 2.2.

Deeply etched waveguides are giving strong optical confinement due to the large index contrast at the semiconductor/air interface, however it poses several loss sources. Due to the nature of the fabrication (lithography and dry etching), the sidewalls of the waveguides are never perfectly smooth. The emerging roughness is on the nanometer scale – well below the wavelength of the laser inside the semiconductor –, which give rise to scattering of the light. It was shown that the amount of scattering is proportional to the intensity of the light at the air/semiconductor interface [41, 42] and to the power of four of the RMS of the surface roughness [43]. Therefore, for deeply etched waveguides, the larger the scattering loss the narrower the waveguide is but truly single mode operation<sup>3</sup> can only be achieved with relatively narrow waveguides so this effect can not be avoided, only reduced by improving the quality of the sidewalls. Furthermore, the core – where the actual recombination of the carriers takes place – has non-crystalline boundaries full with dangling bonds resulting in non-radiative recombination centres as an additional loss source. The resulting extra current (instead of photons) produces phonons, an extra source of localized heat, which quickly raises the temperature of the core and the surrounding area thus degrading device performance and lifetime as well. There are techniques to decrease the amount of unnecessary surface states by passivating the dangling bonds (see [44] for an example for further details) that complicates

<sup>3</sup>By truly single mode operation I mean that the waveguide is not only single mode because of very high losses of the higher order modes but the waveguide itself – without any losses – would not support the modes apart from the fundamental one.

fabrication, although not the non-radiative recombination is the main argument against using deep etched waveguides.

According to [45], backscattering enhances the coupling between the two counter-propagating modes and forces the ring laser to operate in the bidirectional multi-mode regime [46], which makes the ring lasers to lose all their attractive features, and truly – none of the reported deep etched ring lasers show clear unidirectional characteristics. Apart from tunability the laser as a stand-alone single wavelength source has to be of high quality: eg. narrow linewidth, wavelength stability and high SMSR. High SMSR values can only be achieved when there is weak coupling between the two counter-propagating modes (as will be proven in Chapter 5)<sup>4</sup>.

The only attractive feature for deep etching would be the negligible bending loss. Bending loss occurs when a waveguide is bent and – due to the small refractive index difference between a core and cladding – the mode is pushed to the outer radii of the waveguide (even if it is only a planar waveguide) and the solution of the wave equation is not an evanescent tail for the field anymore, but a radiating sinusoidal mode [47]. It is not negligible for shallow etched waveguides (their only drawback) but that issue is carefully addressed later in this chapter in Section 2.3. Finally, introducing strong coupling with strong intra-cavity disturbance raises some issues as well, again, against using rib waveguides (will be explained in more detail in Section 2.2).

Coming to regrowth, even if the technology was available in the framework of this project it is not straightforward that regrowth would be a winning technology for the fabrication of ring lasers: the properties of regrowth are dependent on the crystal orientation, which is constantly changing for a ring shaped laser, thus the resulting layer would be surely full with dislocations and therefore stress causing limited lifetime. On top of that, the refractive index difference provided by the regrown layer does not support strong enough confinement to avoid bending losses: the only ring laser fabricated using regrowth was 3 mm in diameter [33]. The alternative solution would require a square shaped geometry by using corner mirrors. This approach, however, is feasible for shallow etched waveguides as well with much simpler fabrication and no real drawbacks, and the possibility was carefully investigated by the collaborating partners in Bristol within the framework of this project. Drawbacks with this configuration to mention are complex fabrication and – most importantly –, strong intra-cavity disturbance by corner mirrors as shown in [48].

---

<sup>4</sup>Deductively, cross-gain saturation between the counter-propagating modes can be counter-balanced by strong coupling between the two directions.

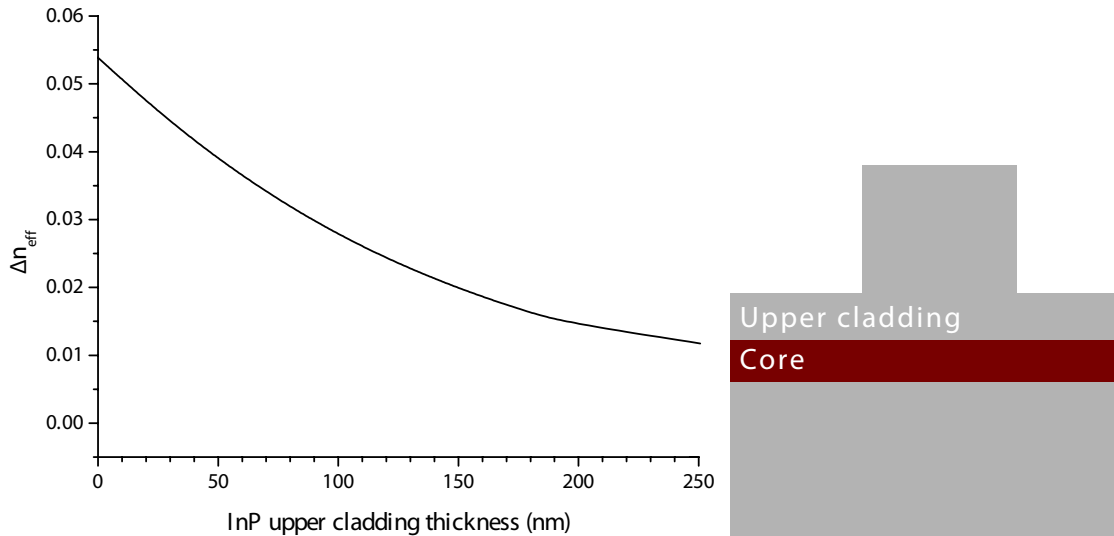


Figure 2.3: Effective refractive index difference as a function of the upper cladding thickness at the etched areas.

### 2.1.3 Shallow etched waveguide design

Two dimensions have to be decided during the design stage of shallow etched waveguides: width and etching depth. The naming convention of the directions are as follows: the direction of propagation or longitudinal direction is called  $z$ . The lateral plane is given by the  $x$ - $y$  plane on a normal right-handed Cartesian coordinate system, where  $x$  is perpendicular to the plane of epitaxial growth and pointing upwards (away from substrate towards the metalorganic vapour phase epitaxy (MOCVD) layers).

Using a 1D mode solver along the  $x$  axis, calculating the modal indexes for the etched and un-etched parts, and then taking their differences as a function of the etch depth gives Figure 2.3. The effective refractive index difference – as shown – quickly rises as the etching depth increases, which indicates an increase in the confinement giving a benefit on the lower bending losses. However, etching into the core is not advisable at all because not only all the benefits of the shallow etched waveguides are lost but a half etched core gives a pear shaped mode profile with a strong substrate loss, so from now on all the simulations are concentrating on the case when the waveguide is etched down (or almost down) to the core.

The most important factor for deciding the waveguide width is that it has to be as wide as possible (for ease of fabrication) but still it must only support the fundamental mode (to avoid modal birefringence). Etching closer to the core

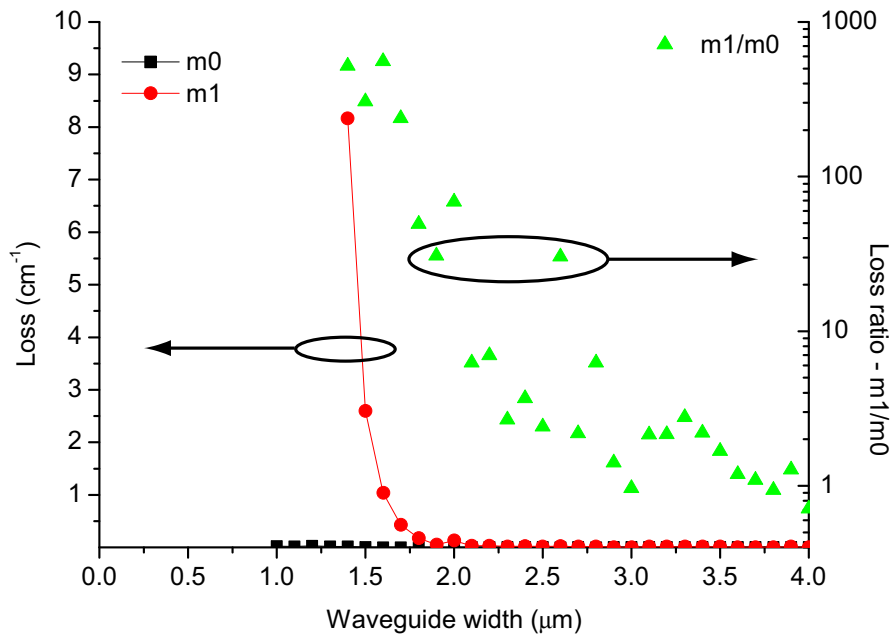


Figure 2.4: Modal loss for the fundamental  $\text{TE}_{00}$  and the first order  $\text{TE}_{01}$  modes as a function of the waveguide width when etched down to the core. Green triangles indicate their ratio.

increases confinement, which prevents single mode behavior unless the waveguide dimensions are shrunk so only the case when it is etched down to the core is considered. In Fig. 2.4 the modal losses are plotted for the fundamental and the first order modes as a function of the waveguide width. Using the figure as a guide,  $2 \mu\text{m}$  waveguide width was chosen (as standard) to ensure single mode operation even when it is etched down to the core. It is worth to note that at a waveguide width of  $2 \mu\text{m}$ , a loss ratio of around ten is expected, however, bending the waveguide with a radius of  $300 \mu\text{m}$  increases this figure by two orders of magnitude. The effects of bent waveguides, however, will be discussed later in the chapter (Section 2.3). Finally, the resulting mode profile was given by a 2D ( $x$ - $y$  plane) mode solver and plotted in Fig. 2.5.

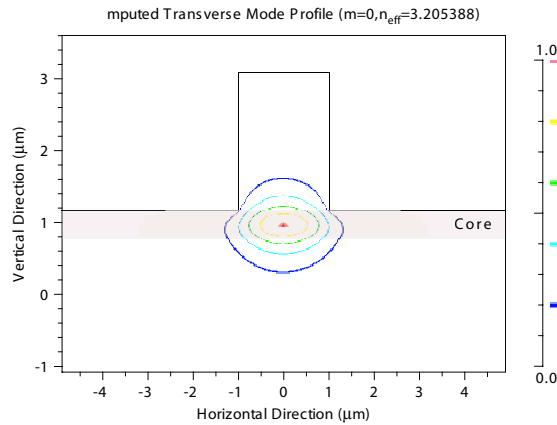


Figure 2.5: Mode profile for  $2\ \mu\text{m}$  wide waveguide when it is etched down to the core.

## 2.2 Couplers

### 2.2.1 Available coupling techniques

The most important part of ring lasers are the output couplers. Not only they extract power from the cavity but they have a strong influence on the laser behavior: the most important factors on deciding the appropriate coupler configuration are coupling efficiency, back reflection to the cavity, configurability (the available coupling ratios), fabrication tolerance and tunability. The available coupling techniques can be classified as follows: y-junction couplers (alternatively x-junction couplers), MMI couplers, evanescent field or directional couplers. Several ring lasers can be found in the literature using one of the three techniques.

Evanescent field coupling was chosen over other coupling configurations because it has several advantages. First of all, any type of back reflection strongly affects the ring laser behavior and the cavity is the least disturbed using evanescent field couplers as the result of the simulation shows in Fig. 2.6. The coupling ratio can not be chosen for y-junction couplers and limited number of ratios can be designed using MMI couplers while evanescent couplers can be designed to any ratio. Fabrication tolerances are relaxed for MMI couplers [7]. Despite the fact that directional couplers are more sensitive to fabrication tolerances, the fabrication errors can be greatly reduced using various techniques as will be discussed in Chapter 3. The properties of different coupler configurations are summarized in Table 2.1.

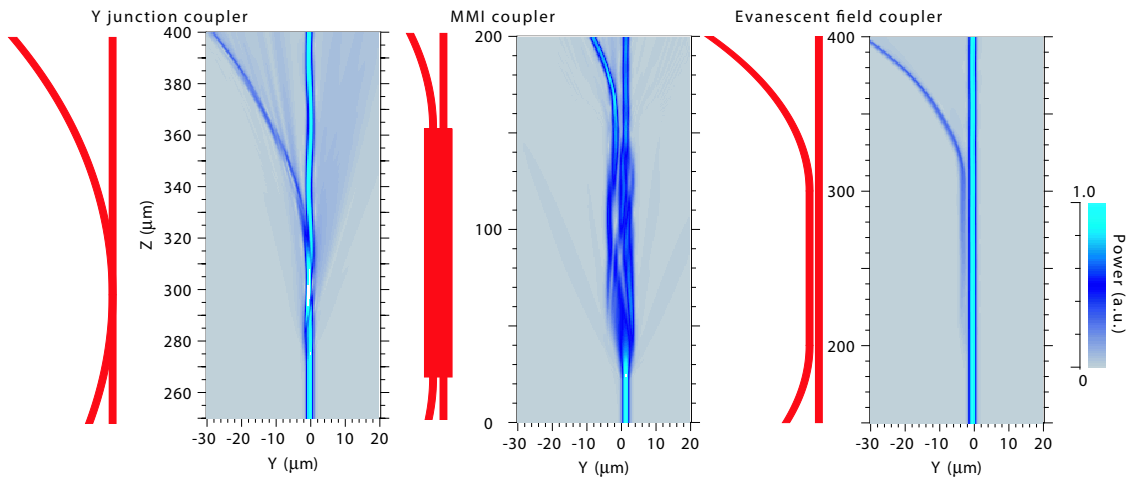


Figure 2.6: Schematic of available coupling techniques and the corresponding simulation using beam propagation method.

Table 2.1: Comparison of the three available coupling techniques.

Coupling type	y-junction	MMI	evanescent field
Intracavity back reflection	strong	weak	negligible
Coupling ratio	weak	strong	any
Fabrication tolerance error	insensitive	less sensitive	very sensitive
Size	very short	long	coupling dependent
Tunability	no	no	yes

## 2.2.2 Evanescent field couplers

The principle of directional couplers are discussed in detail in any of the text books discussing coupled mode theory such as in [47]. If two dielectric waveguides are closely separated in such a way that the evanescent tails of the guided modes are overlapping a coupled oscillator-like effect happens: there is a periodic power exchange between the guided modes as they propagate along the  $z$  direction. In the symmetric case, where phase matching occurs, the power in the output waveguide is proportional to  $\sin^2 Cz$  where  $C$  is the coupling term that is proportional to the overlap integral of tails of the supported modes and so exponentially decreases with increasing (optical) distance between the two waveguides. In any case, the power coupling ratio can be expressed as a function of the beat length and the length of

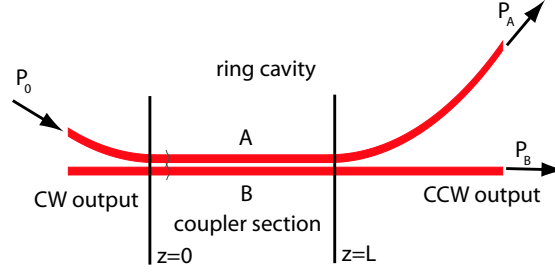


Figure 2.7: Illustration of an evanescent field coupler with part of the ring cavity and outputs.

the coupler as follows:

$$\frac{P_B}{P_0} = \sin^2 \frac{\pi L}{2L_{100}}, \quad (2.1)$$

where  $P_B$  is the coupled power,  $P_0$  is the input power,  $L$  is the length of the coupler and  $L_{100}$  is the beat length, as illustrated in Figure 2.7. Considering the lossless case, the power, which stays in the input waveguide is:

$$P_A = \cos^2 \frac{\pi L}{2L_{100}}. \quad (2.2)$$

In a more complicated structure than coupled slab waveguides, the numerical solution gets more difficult, however there are simulation engines, which give accurate results on 3D structures without making any simplification. A set of 3D BPM simulations were run on different geometries. As an example, Fig. 2.8 shows the power transfer with  $2 \mu\text{m}$  wide waveguides at a distance of  $1 \mu\text{m}$  when it is etched down to the core with the IQE structure. The layer refractive indexes were calculated using the equations from [49].

Other gap widths were simulated as well and the coupling lengths  $L_{100}$  were extracted, the results are plotted in Fig. 2.9. To achieve reasonably high coupling and small devices it is required to fabricate sub micrometer size coupling gaps, however the same figure goes down to below 100 nm gaps for deep etched devices due to the strong confinement.

There is an evanescent coupler type configuration that was not mentioned before: vertical coupling. With the design of a new material a separate low-doped layer can be added for passive wave-guiding. The design would contain two stacked waveguide layers with active waveguide layer above a passive waveguide layer. The output waveguide is made in the passive layer underneath the active ring for easier and controllable access of the SRL. In this structure the gap between the waveguides

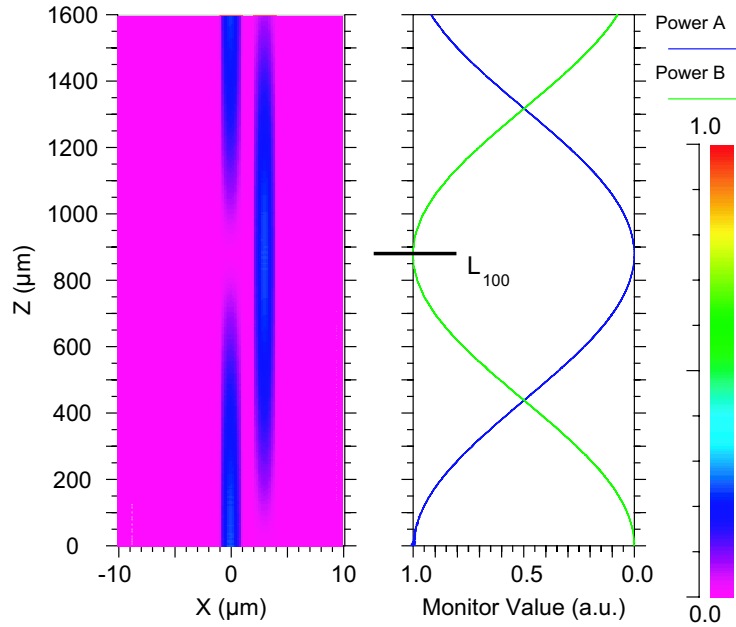


Figure 2.8: Result of a 3D simulation of  $1\ \mu\text{m}$  gap coupler on the IQE material. The contour plot on the left shows power profile from an  $x$ - $z$  slice from the middle of the core, while the right graph shows the corresponding waveguide powers.

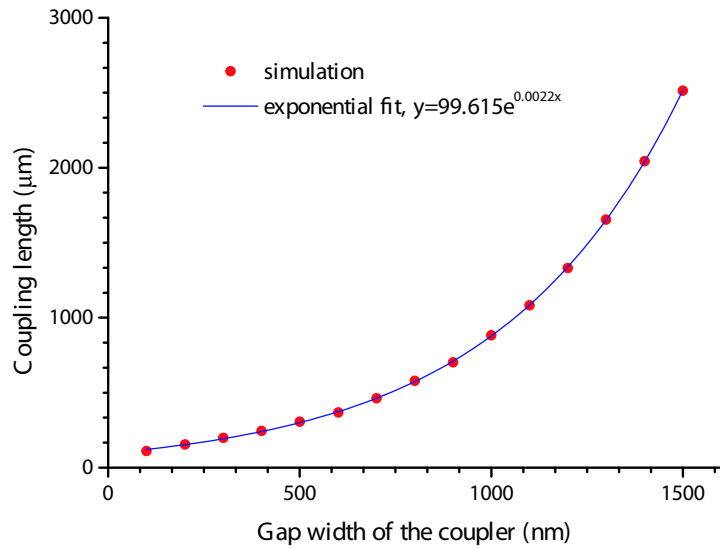


Figure 2.9: Coupling length corresponding to different gap widths between the waveguides.

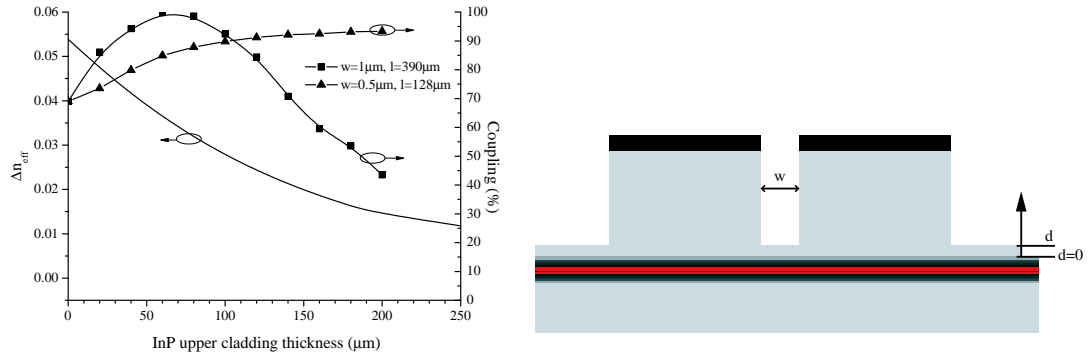


Figure 2.10: Simulated effective refractive index difference (plain curve) as a function of upper cladding thickness outside the waveguides ( $d$ ), and output coupling ratio on a directional coupler for two different gaps ( $w = 1 \mu\text{m}$  and  $0.5 \mu\text{m}$ ). The initial coupling was set to 70 % corresponding to a coupler length ( $l$ ) of  $390 \mu\text{m}$  and  $128 \mu\text{m}$ , respectively.  $d = 0$  corresponds to the top complete etching of the upper cladding.

forming the coupler is defined by epitaxy and therefore is extremely accurate. Different coupling ratios can be achieved by changing the length of the coupler. This approach requires however a very careful material design and growth and the use of an inductive coupled plasma (ICP) dry etch machine.

### 2.2.3 Fabrication tolerance

Despite the fact that directional couplers possess many advantages, they are sensitive to fabrication originated errors. The main source of error comes from the etching depth. Fig. 2.3 have already reported the relationship between the  $\Delta n_{eff}$  and the etching depth and once again the coupling factor has a direct relationship with the *optical* distance of the waveguides: decreased  $\Delta n_{eff}$  decreases confinement and increases coupling. The behavior of two – practically also interesting –, couplers was simulated as a function of the error in the etch depth, as shown in Fig. 2.10. The couplers were designed to provide a theoretical coupling factor value of 70 % when the upper cladding is completely etched away, with  $2 \mu\text{m}$  wide waveguides at distances of  $1 \mu\text{m}$  and  $0.5 \mu\text{m}$  over a length of  $390 \mu\text{m}$  and  $128 \mu\text{m}$ , respectively.

As the etching depth is decreased, the decrease in  $\Delta n_{eff}$  quickly reduces the

coupling length and thus increase the coupling factor. Since in the directional coupler there is a periodical exchange of power from one waveguide to the other, for upper cladding thicknesses greater than 65 nm and a gap of 1  $\mu\text{m}$ , the coupled out light starts to couple back into the input waveguide, decreasing therefore the coupling factor.<sup>5</sup> An error of only 65 nm in the depth leads to a change of the coupling ratio from 70 % to 100 %, preventing laser action. As the coupler's gap is decreased, the coupling ratio becomes less sensitive to etch depth variations, as shown in Fig. 2.10 for a gap of 0.5  $\mu\text{m}$ . An etch depth error of more than 300 nm leads to a solution when the two waveguides are acting as one wide and multi-mode waveguide, showing a mixed characteristic of an evanescent field and an MMI coupler.

Etching deeper than the core was not considered because the developed dry etch stop process stops the etching on top of the core – and the so called reactive ion etching (RIE) lag tends to decrease the etch speed in confined regions such as the gap between the coupler, as will be discussed in Section 3.5.

Let us now consider a lithography originated error in the width of the waveguides. There are two effects present at the same time: confinement is decreased for narrower waveguides so a larger part of the mode travels in the evanescent tail, which would increase coupling, and with narrower waveguides the gap width increases. Also considering fabrication, the waveguide dimensions are usually well defined, the error originates mainly from the leaned waveguide sidewalls inside the etched gap. The latter case was simulated for 500 nm and 1  $\mu\text{m}$  gap waveguides with an absolute error of  $\pm 100$  nm inside the gap as a function of the length of the coupler. Fig. 2.11 details the two cases, where the light blue and red straight lines are the  $\pm 100$  nm error bars, with a narrower gap ( $-100$  nm) giving larger coupling. The two cases are giving roughly the same absolute errors in coupling, which is explained by the counteracting effect from the narrowing of the waveguide.

Evanescent field couplers are indeed very sensitive to fabrication tolerances. Only an error of 100 nm in either the etch depth or the gap width causes significant errors in the designed coupling factor. The etch depth inside coupler is the most critical part, which can severely affect the coupling ratio and it can even result in a multi-mode waveguide like solution.

---

<sup>5</sup>It is worth noting that the coupling factor is weakly affected by variations in the outer etching depth but strongly changes as the etching depth in the gap between the waveguides varies.

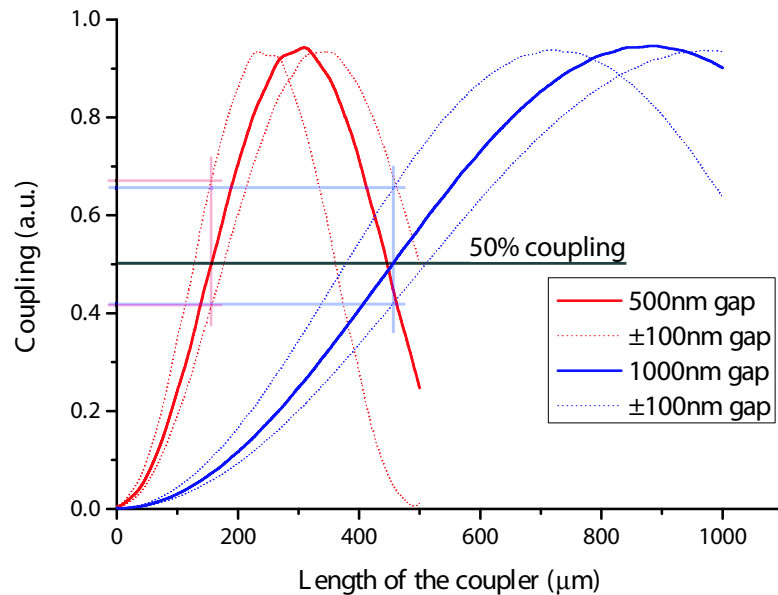


Figure 2.11: Coupling ratio as a function of length (plain curves) with a  $\pm 100$  nm error in the coupling gaps (dotted curves) for  $2 \mu\text{m}$  wide waveguides (original width) for two original coupling gap widths: 500 nm (blue curves) and  $1 \mu\text{m}$  (red curves) when the upper cladding is completely etched away.

## 2.2.4 Tunability

So far only the phase matched condition was discussed, however a refractive index change induces a phase mismatch between the guided modes inside the two waveguides and reduces the coupled power. The group index of a waveguide can be changed by either an applied voltage or injected current due to the electro-optic effects [50,51]. This tunability of the output coupling of a ring lasers give freedom on the output power – and even raises some possible applications such as Q-switched ring lasers, where the switching window is not achieved by saturable absorption but by a tunable coupler with a 100% initial coupling, which prevents the ring from lasing action. The switching could be achieved with voltage or very little current, thus it is expected to work faster than inducing high absorption by current injection. Furthermore, the reverse bias or forward current – inducing dephasing – leads to extra loss or gain on an active material, respectively.

According to [47], the maximum power that can be coupled (considering the

single mode case) equals to

$$\frac{P_B}{P_{0 \max}} = \frac{|C|^2}{C^2 + \Delta k^2/4}, \quad (2.3)$$

where  $C$  is the overlap integral of the fields and  $\Delta k$  is the wavenumber difference of the two guided modes in the two waveguides of the coupler. Considering that

$$\Delta k = \frac{\Delta n}{\lambda_0} \quad (2.4)$$

the maximum of the coupling can be expressed as

$$\frac{P_B}{P_{0 \max}} = \frac{|C|^2}{C^2 + \left(\frac{\Delta n}{2\lambda_0}\right)^2}. \quad (2.5)$$

The effect of an effective refractive index change on one of the waveguides of the coupler was simulated by using 2D beam propagation method. The coupling factor is plotted for different waveguide length in Fig. 2.12 as a function of the group index difference. In the symmetric case, a length of 835  $\mu\text{m}$ , 525  $\mu\text{m}$  and 265  $\mu\text{m}$  gives an initial coupling ratio of 100 %, 70 % and 30 %, respectively. A small change in the refractive index quickly reduces the coupling ratio, following a *sinc*-like function. The reason for this is revealed in Fig. 2.13, where the coupled power is plotted as a function of the length of the couplers for different group index changes. Inducing a refractive index change in one of the waveguides not only decreases the maximum achievable power coupling ratio but decreases the beat length as well, which is not predicted by Eqn. 2.5. For reasons of clarity Eqn. 2.5 was fitted to the simulation results that give the worst case scenario: no matter how long the coupler is, the coupling ratio can not go above the black line in Fig. 2.12.

Despite the simple idea, not many articles can be found in the literature about integrated<sup>6</sup> tunable couplers or switches (apart from [52]), and the reason for that is not obvious. Using deep etching requires very stringent fabrication to fabricate sub 100 nm gaps between the waveguides for reasonable coupling. Using shallow etching – on the other hand –, reduces the electrical resistance between the two waveguides so the index change caused by either reverse biasing or current injection will be visible in both of the waveguides.

---

<sup>6</sup>Integrated on active material.

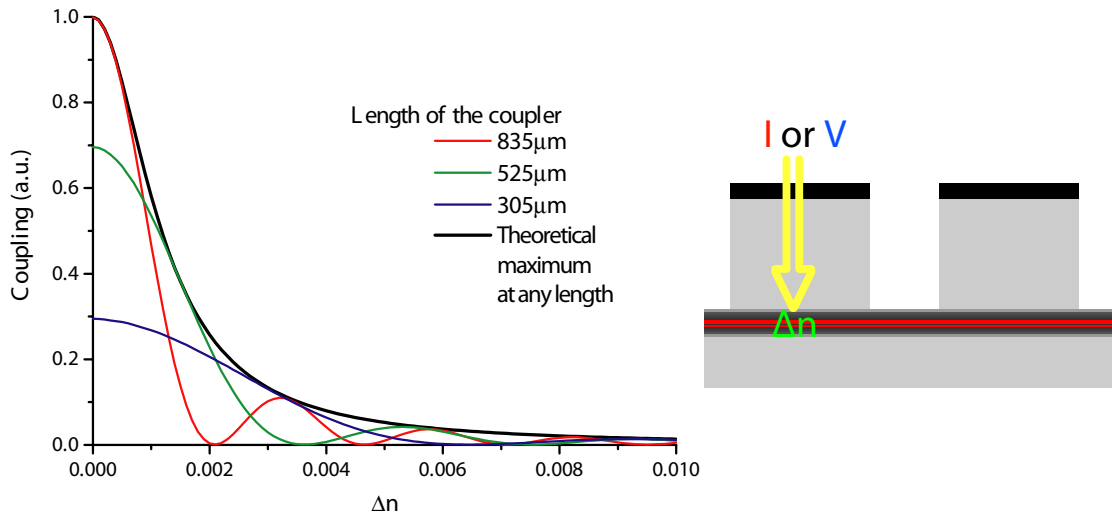


Figure 2.12: Simulation results on the coupling ratio for different coupler lengths (left) and the concept of an integrated tunable coupler (right).

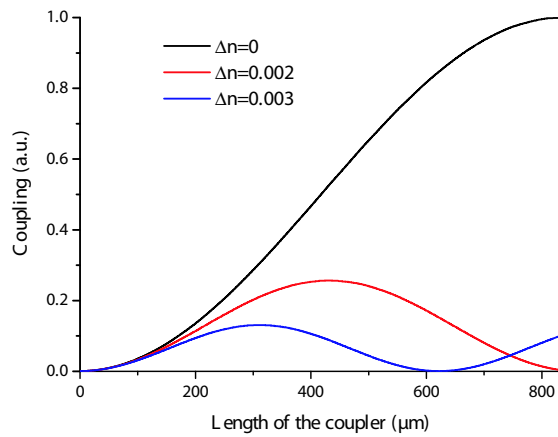


Figure 2.13: Coupling ratio as a function of coupler length for different group index differences.

## 2.3 Effect of bending loss

The main limitation for miniaturizing shallow-etched ring lasers is the bending loss: changes in the direction of propagation invariably lead to some radiation. A numerical analysis on the bending loss in small radius ring lasers was performed by Nabiev, using a powerful mathematical technique, the WKB-method [53]. He found that a  $\Delta n = 0.1$  effective refractive index difference is adequate for negligible bending losses down to a radius of  $50 \mu\text{m}$  and the losses for higher order modes are 1–2 orders of magnitudes higher.

A mode calculation was performed on waveguides with different bend radii using a combined method of BPM analysis and coordinate transformation to map a curved waveguide onto a straight waveguide. The simulations generate complex effective refractive indexes for the guided modes, from which the bending loss can be calculated (Figure 2.14). A complete etching of the upper cladding allows negligible bending losses down to a radius of  $250 \mu\text{m}$ .<sup>7</sup> A decrease in the etching depth of – only –  $50 \text{ nm}$  and  $100 \text{ nm}$ , increases this figure to  $400 \mu\text{m}$  and  $700 \mu\text{m}$ , respectively.

## 2.4 Threshold current and quantum efficiency

With known material properties the cw performance (such as threshold current and external quantum efficiency) of the ring lasers can be predicted to be able to determine the trends and geometry. The usual "gain equals loss" equation (please refer to Appendix B) is modified for racetrack shaped cavity ring lasers to include both curved and straight sections for the couplers (see Figure 2.15):

$$(L + 2R\pi) n\Gamma_w g_{th} = L_{cav}\alpha_0 + \ln \frac{1}{\cos^2 \frac{\pi L}{2L_{100}}} + 2\pi R\alpha_b(R), \quad (2.6)$$

where  $L$  is the length of the coupler,  $L_{100}$  corresponds to the half beat length of the directional coupler (100% coupling factor),  $R$  is the radius of the curved sections,  $L_{cav} = 2L + 2R\pi$  is the total length of the cavity and  $\alpha_b(r)$  is the bending loss using the values from Section 2.3.

The logarithmic term in Eqn. 2.6 accounts for the loss originated by the output power coupling ( $\alpha_c$ ) and describes the periodic behavior of directional couplers as a function of their lengths. In Eqn. 2.6, it is assumed that the directional coupler is bandgap-shifted and left unpumped to avoid refractive index modulation of the coupler and coupling dependence to the pumping current.

<sup>7</sup>The same figure goes down to  $200 \mu\text{m}$  for the IQE material, where  $\Delta n = 0.064$ .

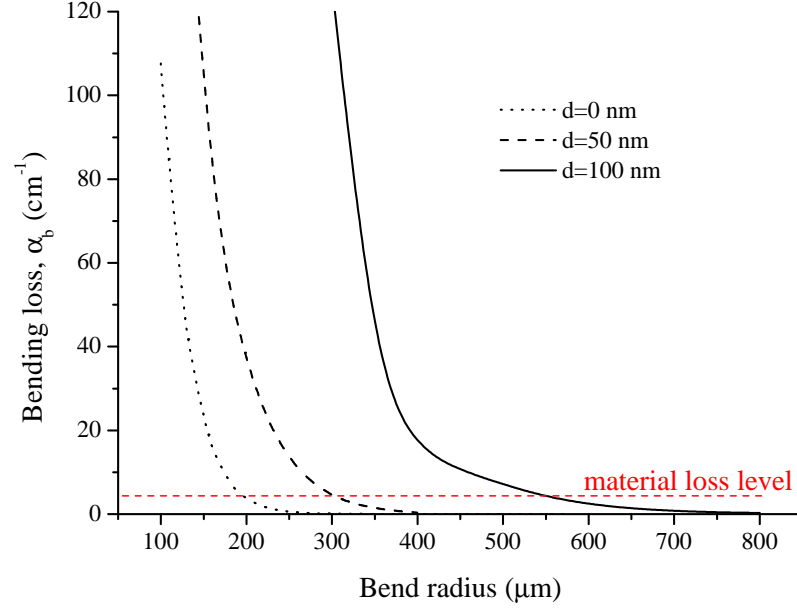


Figure 2.14: Simulated bending loss as a function of bending radius in  $2\ \mu\text{m}$ -wide waveguides for different etching depths.  $d$  corresponds to the upper cladding thickness at the etched areas.

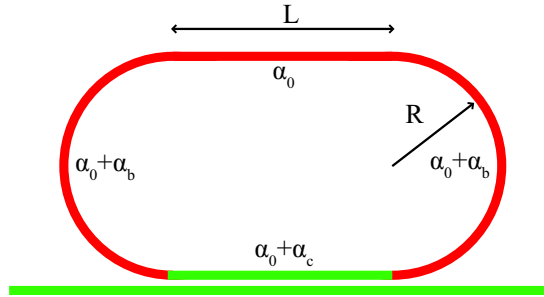


Figure 2.15: A typical configuration of a racetrack cavity SRL with the different loss factors.  $L$  is the length of the coupler,  $R$  is the ring radius,  $\alpha_0$  is the material loss,  $\alpha_b$  is the bending loss and  $\alpha_c$  is the loss of the coupling (because power is coupled to the output). The green part indicates that the coupler and output waveguides are passivated.

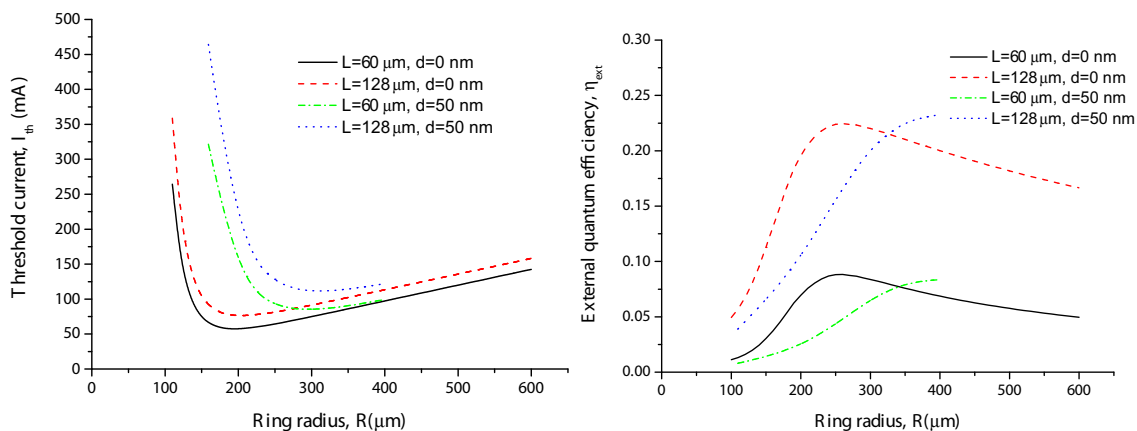


Figure 2.16: Calculated ring laser performance vs. ring radius for different coupler lengths ( $L$ ), and for upper cladding thicknesses ( $d$ ) of 0 and 50 nm. In the case of complete removal of the upper cladding ( $d = 0$ ), the coupling ratio is 20 % and 70 % at coupler lengths ( $L$ ) of 60 and 128  $\mu\text{m}$ , respectively.

As an example, threshold currents and external quantum efficiencies were calculated for different ring laser radii at fixed coupling length using the parameters of the material *2032* (obtained from [54]) and the results are plotted in Fig. 2.16. A minimum value in threshold current of 57 mA is achieved at a radius of approximately 190  $\mu\text{m}$  at a coupling factor of 20 % ( $w = 0.5 \mu\text{m}$ ). The radius can be further decreased to approximately 150  $\mu\text{m}$  without suffering a major penalty in the threshold current (74 mA). All these figures were calculated with a directional coupler gap of 0.5  $\mu\text{m}$ . Note that the minimum threshold current is not at the same radius as the maximum external quantum efficiency, so there is a trade-off between the minimum threshold current and the highest quantum efficiency.

Let us now focus on the fixed cavity length figures. 0.5  $\mu\text{m}$  couplers were chosen for the 100 GHz and 50 GHz cavities corresponding to 925  $\mu\text{m}$  and 1850  $\mu\text{m}$  total cavity length, respectively. Varying both the radius of the ring and the length of the coupler the length of the cavity can be kept constant. The predicted threshold currents and external quantum efficiencies are shown in Fig. 2.17. The maximum ring radii are limited to 145  $\mu\text{m}$  and 290  $\mu\text{m}$ , corresponding to 100 GHz and 50 GHz free spectral ranges (FSRs), respectively. Further increase in the cavity length can not be achieved without changing the FSR. In these cases the external quantum efficiencies decrease close to zero because the couplers exist only at one point of the full ring cavity. For 50 GHz, the peak in both threshold current and external

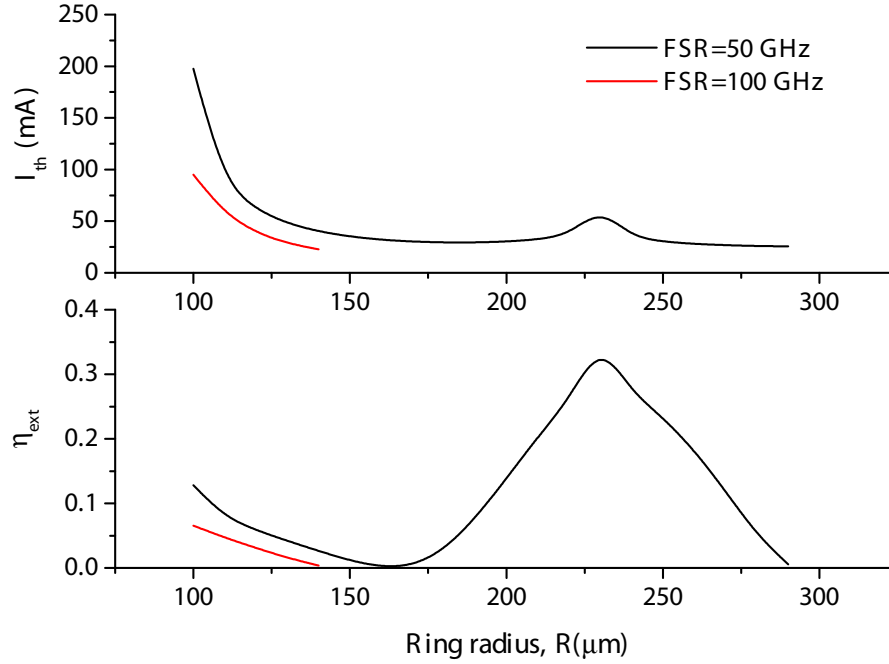


Figure 2.17: Threshold currents and external quantum efficiencies of racetrack shaped SRLs varying the radius of the ring and the length of the coupler to keep the cavity length fixed to  $925 \mu\text{m}$  and  $1850 \mu\text{m}$  corresponding to FSRs of 100 GHz and 50 GHz, respectively.

quantum efficiency correspond to a coupler length equal to the half beat length of the coupling, where the coupling is close to 100%. The threshold current would reach infinity and  $\eta_{ext}$  reach 35% close to that point. The 100 GHz devices are strongly influenced by the bending loss and/or low coupling, however stronger coupler (with smaller gap) can be chosen in order to improve device performance. A fabrication related issue helps to overcome these limitation as well: small gaps require over etching of the couplers because the etching speed is slower at confined spaces as will be discussed in Section 3.5 in more detail. During the extra etching time the 50 nm InAlAs layer is etched (despite the high selectivity), a couple of 10 nm extra etching in depth pushes further down the limit defined by the strong bending losses.

Joining a curved and a straight waveguide results in insertion loss because the mode position in the curved section is shifted to the outer perimeter of the waveguide. None of the results contain the effect of the insertion loss, even though

it was considered: A preliminary set of simulations was run to get information on insertion losses, and it was found that the effect is negligible (even at very small ring radii), since the effective refractive index differences are very small.

## 2.5 Distributed feedback mirror

A technologically convenient way to fabricate integrated tunable Bragg reflectors is the use of lateral gratings, which are shallow gratings defined by periodically varying the width of a ridge waveguide [55]. They allow easier injection of current into the waveguide, reduced fabrication processing and high flexibility in designing the Bragg wavelength. Furthermore, they reflect in a narrow (tunable) band, which makes them ideal as feedback for rapidly tunable ring lasers.

The design of the gratings was carried out as follows. The effective refractive index of a normal  $2\ \mu\text{m}$ -wide waveguide was simulated and further confirmed by measurements, giving a value of  $n_{\text{eff}} = 3.21$ . The 2D geometry of a  $2\ \mu\text{m}$ -wide grating with a recess of 500 nm on each side and a period of 0.25  $\mu\text{m}$  with a duty cycle of 50% was fed back to a commercially available simulator. The target wavelength of the grating was specified as 1550 nm and the simulator adjusted the period of the grating – using the coupled mode theory – to a value of 242 nm. According to the simulation, such a geometry with a length of 50  $\mu\text{m}$  would give a stop-band, as shown in Fig. 2.18, centered at the desired wavelength.

The coupling coefficient for the structure was calculated to be  $\kappa = 203\ \text{cm}^{-1}$  by using the equation described in [56]:

$$\kappa = 2\Delta n_{eq}/\lambda_B,$$

where  $\Delta n_{eq}$  is the equivalent refractive index difference of a rectangular grating and  $\lambda_B$  is the Bragg wavelength.  $\Delta n_{eq}$  was calculated subtracting the simulated effective refractive indexes of the waveguide with full width and the waveguide with no teeth.

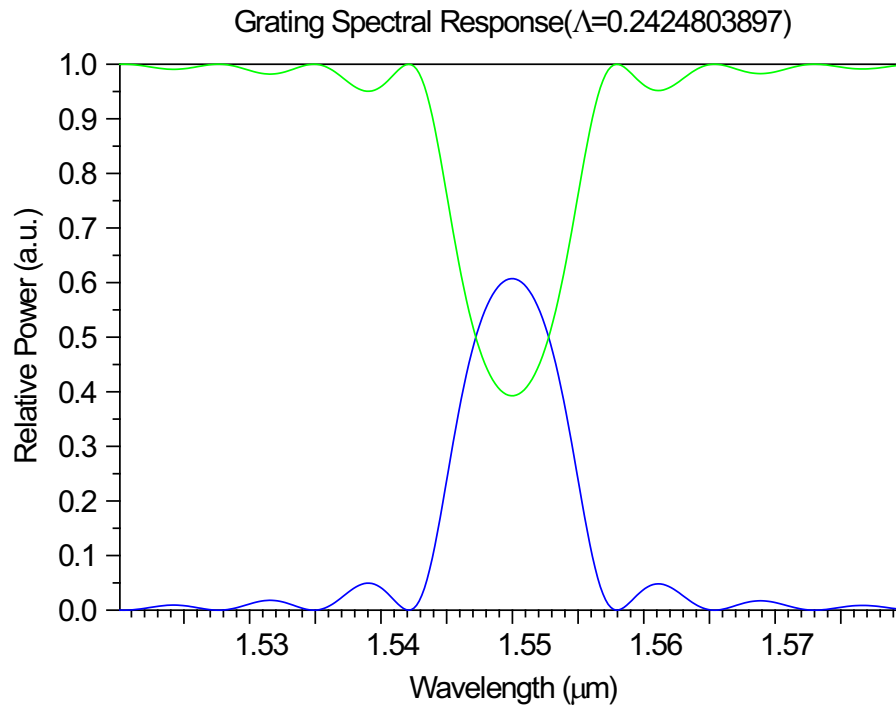


Figure 2.18: Simulated stop-band of a 2D grating with a refractive index of  $n = 3.21$ , a total width of  $2 \mu\text{m}$ , a recess of  $500 \text{ nm}$ , a length of  $L = 50 \mu\text{m}$ , a duty cycle of 50%. Simulations indicate a coupling coefficient of  $\kappa = 203 \text{ cm}^{-1}$ , thus a  $\kappa L$  product of  $\kappa L = 1.015$ .

# Chapter 3

## Fabrication

To a certain extent, ring laser fabrication requires similar processing steps – from wafer level to final packaging – as other, commercially available semiconductor lasers: waveguides need to be etched, contact insulation and contact layers need to be formed, and finally, individual lasers need to be cleaved and mounted. Behind this simplified process flow, however, there are over sixty technological steps, most of which are crucial for functional devices and high yield. All the fabrication steps were initially carried out in the cleanroom of the department and later in the newly built James Watt Nanofabrication Centre.

First of all, an overview is given on the main fabrication steps while separate sections are dedicated to the critical steps where major process development was carried out, such as dry etching. The chapter is finished by a flow chart detailing the available process routes including optional and recommended steps. Finally, a full list of chemicals, resists and equipment used is listed in Appendix D.

### 3.1 Overview of the process steps

The main fabrication steps are schematically shown in Fig. 3.1, and can be summarized as follows:

1. Waveguide mask layer definition into a silica ( $\text{SiO}_2$ ) hard mask.
2. Waveguide etching by RIE.
3. Silica deposition serving as insulation layer.
4. Contact-window definition on the top of the active waveguides.

5. Formation of metal contact pads on the p-side of the wafer.
6. Wafer thinning.
7. Entire n-side metallization.
8. Cleaving and mounting of separate laser bars.

## 3.2 Sample preparation

### 3.2.1 Cleaning techniques

Sample preparation starts with cleaving of the samples to (usually) 10x12 millimeter pieces to minimize the waste of material during the technological process development. Both, the processing environment and the samples must preserve cleanliness all along the fabrication steps, therefore the very first step is always a thorough cleaning: five minutes of ultrasonic bath in acetone soluble Opticlear is followed by five minutes of acetone ( $\text{CH}_3\text{COCH}_3$ ) and five minutes of isopropyl alcohol (IPA,  $\text{C}_3\text{H}_8\text{O}$ ) cleaning in ultra-sonic bath. The solvents are used to remove organic and inorganic contaminants, while ultrasonic waves enhance the efficiency. The previously used common technique – that cleaning steps were finished by water soaking – was replaced by IPA soaking because it was found that IPA leaves less residual than water. The main reason is believed to be the better wetting property of IPA on semiconductor compared to water, so drying of the sample happens only at the nitrogen blowing-off stage.

All the process steps were always followed by cleaning steps, which will not be detailed later, so a short summary is given below. Intermediate cleaning stages were used where no process residuals were expected (for example scanning electron microscope (SEM) investigation): a short (5-5 minutes) rinse in acetone and IPA. Apart from that, resist residues were often removed with oxygen ashing, or – in the case of hardened mask (such as after reactive ion etching) – RIE oxygen was used for a complete resist removal. The wet-etching steps were also always finished with the acetone-IPA process. It is worth noting that after the waveguide definition, no ultrasonic bath was used to avoid the risk of breaking the waveguides. Instead, during full resist removal (such as after lift-off) the effect of acetone was enhanced by using a hot bath.

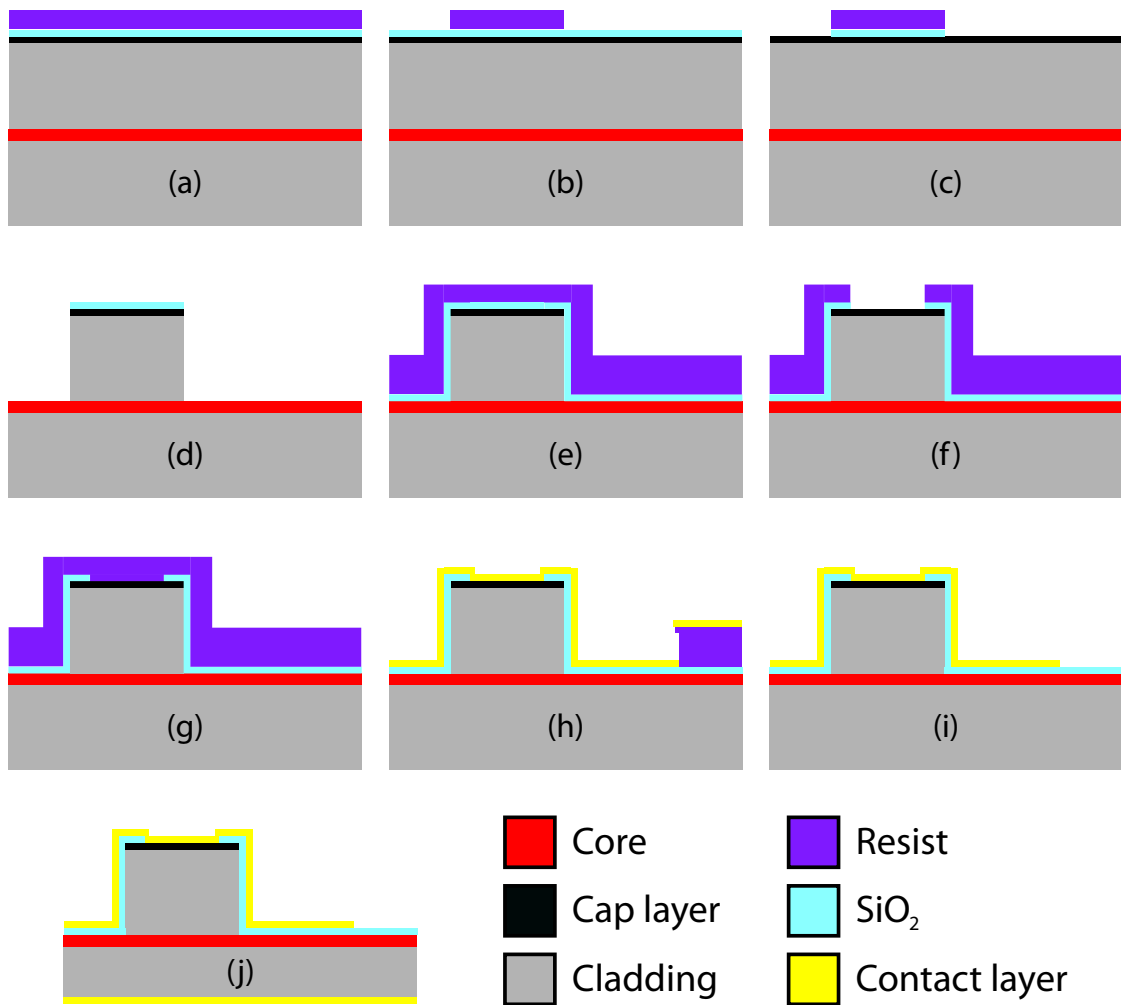


Figure 3.1: Main fabrication steps (not to scale): (a) silica deposition and e-beam resist spinning, (b) waveguide mask lithography, (c) silica etching, (d) resist removal and InP etching, (e) silica deposition and e-beam resist spinning, (f) contact window lithography and silica etching, (g) e-beam resist spinning, (h) contacts lithography and p-contact deposition, (i) lift-off, (j) thinning and n-contact deposition.

### 3.2.2 Marker definition

Any type of multiple-stage lithography requires the definition of alignment markers. It is particularly important in the case of electron beam lithography (EBL) because the alignment is automated and alignment markers have to be well-defined and reliable. Two types of marker fabrication techniques were used, namely gold and etched markers.

The gold markers are usually  $40 \times 40 \mu\text{m}$  rectangles made by evaporated layers of 20 nm NiCr and 120 nm Au defined by lift-off using either EBL or UV lithography. Gold markers give a positive contrast to the EBL tool that can be detected with high precision. However, there is a technology related problem with gold markers: using quantum well intermixing (QWI) involves a high-temperature annealing step and the markers get severely damaged. One way to address this issue is to define lithography markers after the QWI step but then it is difficult to ensure two times the same precision of alignment using only the corner of the chip as reference. Therefore, the previously common routine of using gold markers was replaced by etched markers.

The etched markers – as the name suggests – are rectangles, etched into the semiconductor so the electron beam can locate the edges of the trenches. They do not get damaged from high temperature annealing so they can be defined as a very first fabrication step. They are fabricated by opening windows in either ebeam or UV resist and by using a double etch process: 90 seconds in 3:24:120  $\text{H}_2\text{SO}_4:\text{H}_2\text{O}_2:\text{H}_2\text{O}$  removes the top InGaAs cap layer and 4 minutes of 90:30  $\text{H}_3\text{PO}_4:\text{HCl}$  removes an adequate (about 1800 nm) portion of the InP layer. The two types of markers are shown in optical microscope images in Fig. 3.2, where after a first alignment attempt, etched markers and gold markers gave 1-2  $\mu\text{m}$  and a 40  $\mu\text{m}$  misalignment error, respectively.

A few micron of misalignment (coming from the leaning sidewalls caused by anisotropic etchants) is tolerable for aligning the intermixing pattern but not adequate enough for further process steps. The most convenient way to increase precision is to define dry etched markers in the same step as waveguide etching and using this new set of markers in the following steps: it was found that RIE etched markers have good (around 150–200 nm) alignment accuracy.

A few additional issues should be carefully considered in defining the optimum fabrication procedure: gold markers tend to come off and degrade during fabrication, while the ebeam can not always locate the etched marker edges. Depending on the required alignment accuracy, ease of fabrication and reliability, a number of

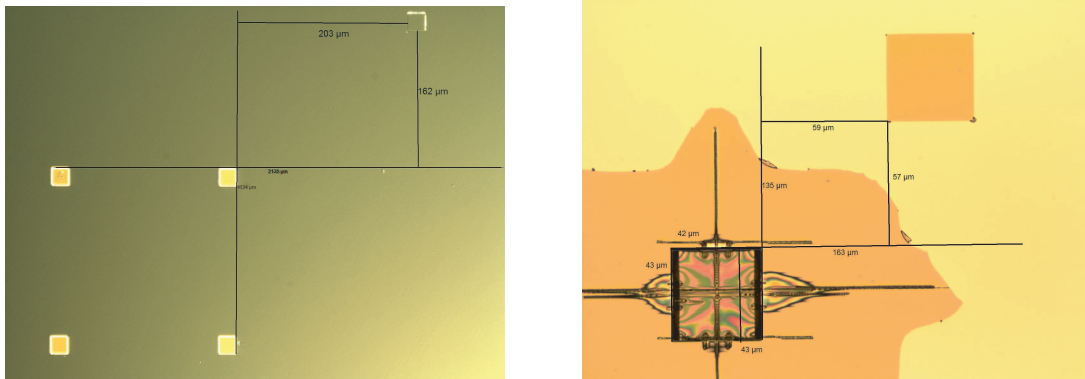


Figure 3.2: Gold markers and an etched marker on the left and right, respectively and the corresponding distances from a test rectangle on the intermixing layer showing the alignment accuracy (intended distances were 200,200  $\mu\text{m}$  and 60,60  $\mu\text{m}$ ).

different fabrication routes can be devised:

- QWI – gold marker: Not good alignment to intermixed pattern, requires careful design updates during fabrication, especially for correcting rotational misalignment. Markers tend to come off. Ease of fabrication: medium. Final alignment accuracy: 50 nm.
- Wet etched marker – QWI – RIE marker with waveguides: No problems with intermixing at all. Can be problematic with EBL edge location. Ease of fabrication: easy. Final alignment accuracy: 150–200 nm.
- Wet etched marker – QWI – gold marker: No problems with intermixing, no problems with edge location. RIE cell markers can be defined as well. Ease of fabrication: difficult. Final alignment accuracy: 50 nm.
- RIE marker – QWI: No problems apart from EBL edge location. Ease of fabrication: very difficult. Final alignment accuracy: 100–150 nm.

The number of available choices can also be further extended by considering UV lithography, although it can only be used for defining the first markers because UV masks can not be precisely aligned for existing patterns. However, manual alignment to the edge of the chip gives better (typically  $< 0.5^\circ$ ) rotational misalignment than that achieved with EBL ( $\sim 1^\circ$ ), which is particularly important during the final cleaving of laser bars.

### 3.3 Quantum well intermixing

The integration of photonic components onto III-V substrates offers high performance and low-cost at the same time. However, the interconnecting waveguides between active elements have to be low loss. This task is usually carried out by using either selective area epitaxy or regrowth [57]. On the other hand, apart from the complexity, a high level of integration usually involves curved waveguides, which poses limitations on pre-growth techniques.

An alternative approach is a post-growth technique known as quantum well intermixing. Dislocations inside the core and a subsequent high temperature annealing promotes inter-diffusion of the atoms of the QWs and barriers – hence the name QWI. The result is an enlarged bandgap of the QWs (and shrinkage of barrier bandgap due to averaging effect), therefore reduced free carrier absorption at the operational wavelength. There are several ways to induce damage, from which probably the most effective way is implanting ions into the core, such as described in [58]. Intermixing can also be achieved using Argon plasma [59], Aluminum-oxide [60] or using the sputtered silica technique [61]. The latter technique has proven to be universally suitable for all material systems. Furthermore, the technique is relatively simple, requires lower annealing temperatures for the same bandgap shift than the similar techniques. It was also developed and now it is well assessed at the University of Glasgow, therefore the same technique with some minor modifications was used in the present work.

#### 3.3.1 Sputtered silica QWI

The technique starts with a lithography, where windows are opened on a thick resist (at least  $1\ \mu\text{m}$ ) where QWI is desired. Then sputtered silica is deposited onto the sample, which does not damage the areas protected by the resist. Because only a 50 nm layer of silica is deposited, it can be easily lifted-off. The process can be assisted by very short ( $\sim 3\text{sec}$ ) ultrasonic cycles. After a thorough clean, 200 nm plasma enhanced chemical vapor deposition (PECVD) silica is being deposited all over the sample. Finally, a high temperature rapid thermal annealing ( $600\text{--}700\ \text{°C}$ ) promotes interdiffusion and gives the required bandgap-shift. The sputtered silica technique and the idea of QWI are illustrated in Fig. 3.3.

The bandgap shift can be characterized by measuring the photoluminescence (PL) spectra of the samples. The measurements were carried out using the setup indicated in Fig. 3.4. The sample is cooled down with liquid Nitrogen (to 77 K) to

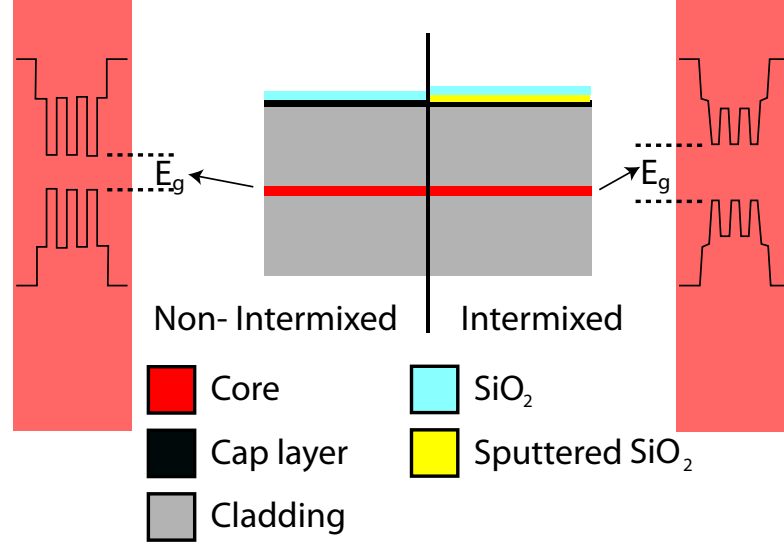


Figure 3.3: Illustration of the sputtered silica QWI technique. Interdiffusion of the atoms of QWs and barriers results in an enlarged bandgap.

increase the PL efficiency and it is excited by an Nd:YAG laser lasing at 1064 nm. The optically excited carriers relax back to the ground state with spontaneous emission around the wavelength of the bandgap, giving information on the resulting band properties. Fig. 3.4 shows two spectra taken from the IQE material<sup>1</sup>, both of them processed with QWI: one was left unannealed while the other was annealed at 650 °C in a rapid thermal annealer (RTA) for one minute. Even though, the Varshni relation approximates well the temperature-dependence of semiconductor bandgaps

$$E_g(T) = E_0 - \frac{\alpha T^2}{T + \beta}, \quad (3.1)$$

where  $\alpha$  and  $\beta$  are fitting parameters – characteristic of a given material –, one does not make a significant error when the bandgap shift is calculated from the values measured at 77 K [62].

The PL shift was measured for various annealing temperatures and the result is plotted in Fig. 3.5. It is worth to note that during annealing, a fast temperature ramp-up results in a severe damage to the semiconductor surface, therefore the annealing profile was also optimized with the final temperature profile, shown in Fig. 3.5.

<sup>1</sup>The material structure was reported earlier in Fig. 2.1.

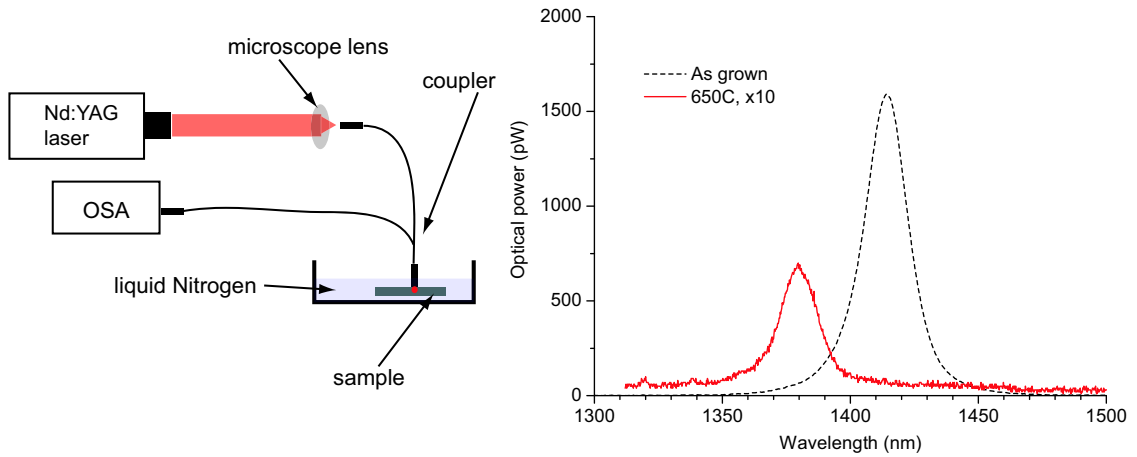


Figure 3.4: Illustrating the PL measurement setup (left), and PL spectra (right) taken from an as-grown sample (dashed black) and from one annealed at 650 °C (red).

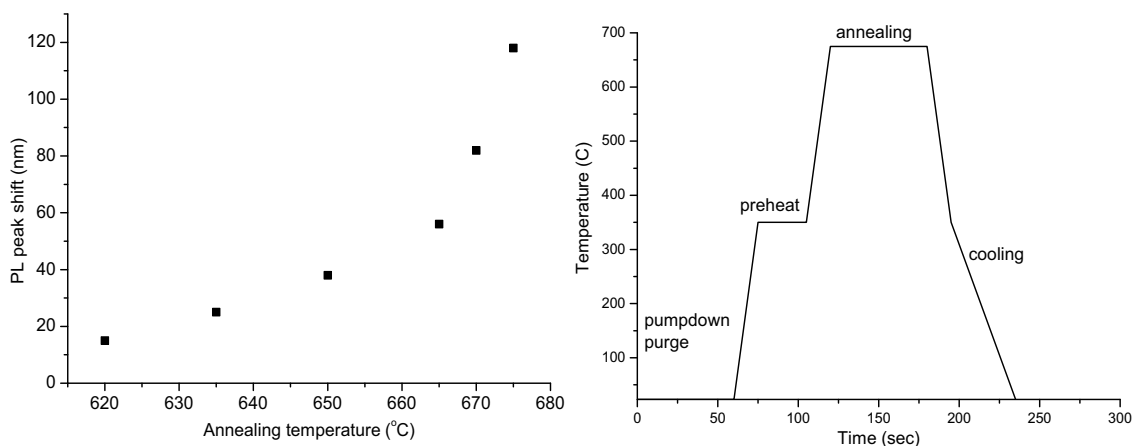


Figure 3.5: Measured PL peak shift as a function of annealing temperature (left) and the corresponding temperature profile during annealing at 675 C° (right).

### 3.3.2 QWI modulation

A monolithically integrated PIC might consist of several elements, which require different bandgap shifts. Passive waveguides have to be intermixed as much as possible for minimum losses, while phase shifters, tunable DBRs usually require a medium (30–40 nm) bandgap shift for maximum electro-optic effect at minimum losses [54].

A technique for multiple bandgap control called QWI modulation, or selective intermixing in selective areas (SISA) were already described in [59, 63]. The idea is that the amount of surface damage correlates with the bandgap shift: more damage gives larger shifts. To do so, the intermixing mask can be designed in such a way, that for example only half of the intermixed area is exposed to the surface damage by alternating densely spaced lines in the mask. The only criterion is that the maximum mask feature size must be smaller than the *diffusion length* of the intermixing. For example 1  $\mu\text{m}$  line – 1  $\mu\text{m}$  gap would give a duty cycle of 50 %. As an example, Fig. 3.6 shows an optical microscope image of a patterned sputtered silica on a chip containing some test waveguides with different duty cycles.

It was found that diffusion length of intermixing is several tens of microns, so a minimum lithography feature size of 2  $\mu\text{m}$  was used. Due to the limited time frame, only preliminary testing was carried out on QWI, therefore, the results are not reported in this work.

### 3.3.3 QWI related problems

Beside the beneficial reduction in free carrier absorption loss, unfortunately it was found that the sputtered silica QWI technique carries several disadvantages. For sufficient bandgap shift, relatively high annealing temperatures are required. Above 400 °C, the InP already starts to decompose and the core layer gets severely damaged resulting in a large penalty on available gain: on average, a 30 % larger threshold current densities of the lasers were found on a chip with intermixing, compared to an all-active one. The temperature performance of lasers was also degraded, although it was not characterized in detail.

Further care must be also taken when larger samples are annealed. It is a common technique to optimize the annealing temperature on 2x2 mm test pieces and proceed with the actual larger sample. Using a temperature of 675 °C results in a bandgap shift of around 120 nm on a test piece but only 35 nm of shift was found on a 10x12 mm sample using the same conditions. No scientific evidence was found to support the hypothesis that smaller bandgap shifts are caused by a

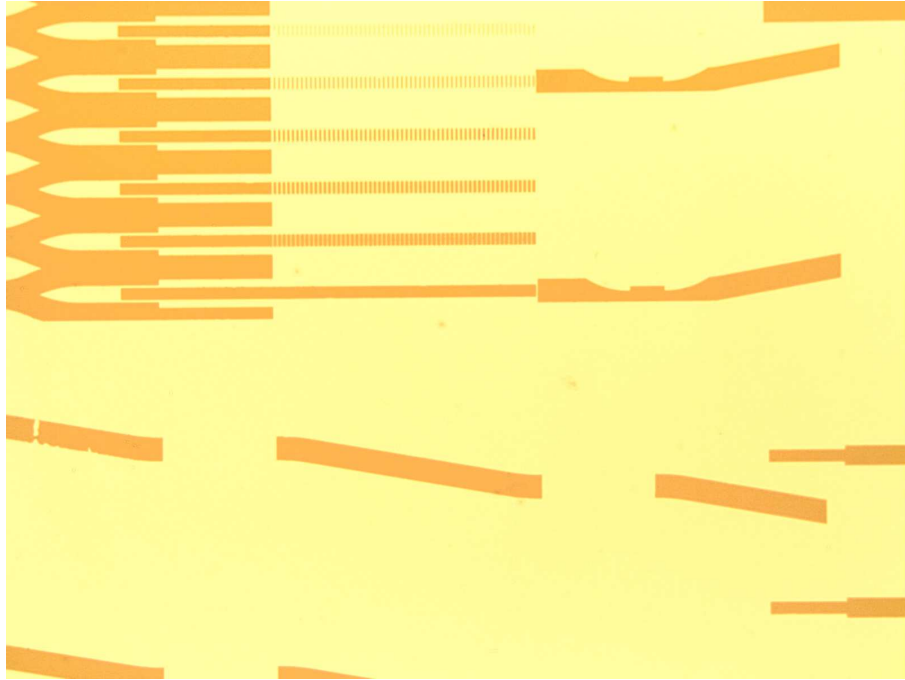


Figure 3.6: Optical micrograph of patterned sputtered silica on top of a sample. Tilted parts correspond to the output waveguides of ring lasers. Sputtered silica areas with variable density are for QWI modulation.

larger thermal mass of a larger sample. Especially knowing that the temperature is tightly controlled by a control loop where the thermocouple is sitting right under the sample.<sup>2</sup>

Furthermore, sputtering silica onto the surface strongly damages the top cap-layer. It was found that intermixed areas have a much larger contact resistance than normal ( $15\text{--}20\ \Omega$  instead of the normal  $1\text{--}2\ \Omega$  on a normal  $600\ \mu\text{m}$ -long DFB). As a result, large contact resistance gives a penalty on the speed and power consumption of passivated active elements, such as phase shifters, DBRs, etc.

The strong decrease in the intensity of intermixed sample's PL peak (such as shown in Fig. 3.4) already indicates that this technique is not suitable for bandgap shifted lasers: the strongly reduced gain results in a threefold threshold current density increase of FP lasers with a bandgap shift of only  $35\ \text{nm}$ .

To conclude, the sputtered silica QWI technique is a useful tool for reducing free carrier absorption loss of passive waveguides. Multiple bandgap is also feasible with the QWI modulation technique. Despite the advantages, there are several

<sup>2</sup>A K-type thermocouple is touching the 6 inch silicon carrier wafer that holds the sample.

disadvantages and it must be carefully considered when it is absolutely necessary to use.<sup>3</sup>

## 3.4 Lithography

Fabrication of SRLs involves several (typically 4–6) lithography steps, which were exclusively carried out by using the department’s EBL tools: EBPG5 and VB6. Beside the high resolution (down to a few nm with the VB6) and good contrast, EBL allows direct patterning of samples with sizes ranging from a few mm<sup>2</sup> to full six inch wafers. Therefore EBL is perfectly suited in a research environment where small sample quantities with ever changing design are common.

This section introduces the development of design rules for a full mask-set along with EBL techniques and resist issues. The proximity error – the main limiting factor of EBL –, and proximity error correction (PEC) is also discussed.

### 3.4.1 Automated layer generation

Generally, the devices consist of active and passive waveguides, i.e. the active waveguides are pumped with a separate contact pad while the passive waveguides are just connecting elements. The very first step of the design flow is always defining the layout/shape of the devices: where to use passive waveguides, what shape of a ring laser should be, what type of coupler, what bend radii to use, etc. All the other lithography masks (for example for intermixing or contact window) can be designed according to certain design rules, driven by technological constraints.

To reduce design time, automated mask generation – a technique routinely used in the IC industry – was applied here for the fabrication of integrated devices<sup>4</sup>. First, the exact shape of active and passive waveguides are laid out on a full chip scale containing about 50–100 various elements such as ring lasers, DFBs, FP lasers, test couplers, half ring lasers, passive waveguides. Then the required full mask set can be generated by a simple *press of a button*.

Fig. 3.7 shows part of the masks of a ring laser. The full mask set contains markers, waveguides, contact window, p-contact. The *markers’* mask is the simplest as it contains rectangles and crosses only, so this is usually defined in the first place. In the case of a positive ebeam resist (such as PMMA), everywhere

---

<sup>3</sup>Some materials are not suitable for QWI at all, for example intermixing the 1.3- $\mu\text{m}$  material always resulted in a red shift of the PL peak.

<sup>4</sup>Tanner’s CAD software, L-Edit was used for mask design and layer generation.

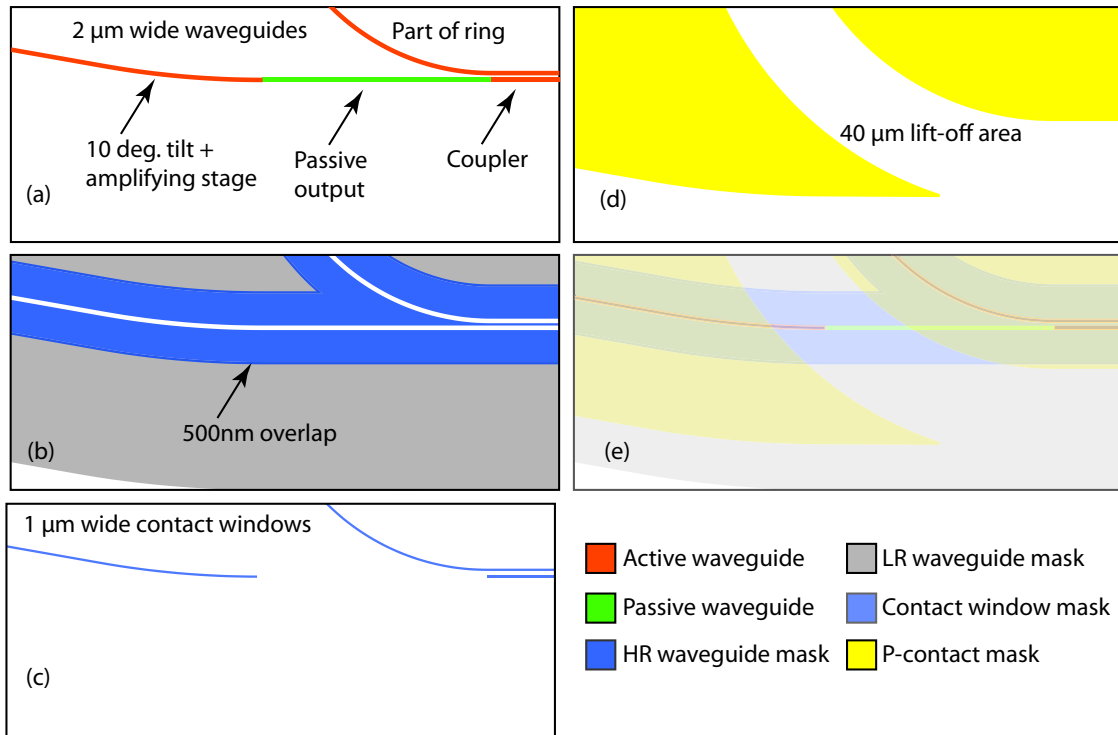


Figure 3.7: Example on automated mask generation. (a) hand drawn active and passive waveguides, (b) waveguide mask set with high and low resolution layers, (c) contact window mask, (d) p-contact mask and (e) full mask set together.

is written but the waveguides. To reduce the ebeam writing time, the waveguides are defined by two layers: one with a higher resolution – written  $15\ \mu\text{m}$  on each side of the waveguide – and one with a lower resolution written outside of this area. The higher resolution layer (Fig. 3.7b) is generated from the passive and active waveguide layers (Fig. 3.7a) with the rule  $(GROW15\mu\text{m}(\text{passive OR active}) NOT (\text{passive OR active}))$ , where  $GROW15\mu\text{m}$  means an enlargement of layers by  $15\ \mu\text{m}$ , and  $OR$  and  $NOT$  are operators well known from Boolean logic. With similar logic, the low resolution (faster writing time) layer can be defined, as well as the other mask sets shown in Fig. 3.7.

### 3.4.2 Electron beam lithography

After designing the full mask set, the lithography masks were transferred to the samples by using electron beam resist and either the EBPG5 or VB6 operated at a beam energy of 50 kV or 100 kV, respectively. One of the most common EBL

resists is PMMA and it can be routinely used for all the lithography steps because of its high resolution, relatively good contrast and medium dry etch resistance. Furthermore, both the resist and its developer (a solution of MIBK and IPA) are relatively cheap.

The waveguide definition was carried out by using a double layer of 110 nm thick PMMA. Double layer is used to avoid any pinholes in the mask that might affect the subsequent dry etching of the underlying silica hard mask. An other technology is based on a double layer of 1.1  $\mu\text{m}$  and 120 nm PMMA, which was used for lift-off processes (such as gold marker and p-contact definition), where the top thinner layer has a smaller sensitivity. This way, an undercut forms during development, which helps to remove the metal layers on top of the resist (as already illustrated in Fig. 3.1h). The same resist combination was used for contact window opening: during contact window lithography, the waveguides are already etched, so a thicker resist is required for complete coverage.

The waveguide resist mask must have small edge roughness in order to minimize any imperfection transfer into the silica hard mask and waveguide sidewalls. An improvement can be achieved by using an alternative resist called HSQ.<sup>5</sup> It is a negative tone, spin-on glass type resist, which has several advantages: It has very high resolution, faster baking time and good etch resistance (almost as good as PECVD  $\text{SiO}_2$ ), which makes it suitable as a hard mask for etching of InP. Therefore it can further simplify the process with higher quality masks. Even though a thicker resist must be used (600 nm instead of the 220 nm of PMMA), the HSQ contrast is extremely good, which allows the definition of features with aspect ratios better than 1:6 – for example a 100 nm gap of a coupler with 600 nm-thick resist. An important resist property is the contrast curve that provides the optimum exposure dose: a sample was covered with 600 nm of HSQ and it was exposed at different electron dose levels. After development, the residual thickness can be measured and plotted, as depicted in Fig. 3.8.

### 3.4.3 Proximity error correction

Despite the advantages, EBL carries several disadvantages. First of all, in a chip there are several features integrated together: gratings, bent waveguides, couplers, tapers, etc., which have different feature sizes and thus require different doses.

---

<sup>5</sup>Full name in list of materials.

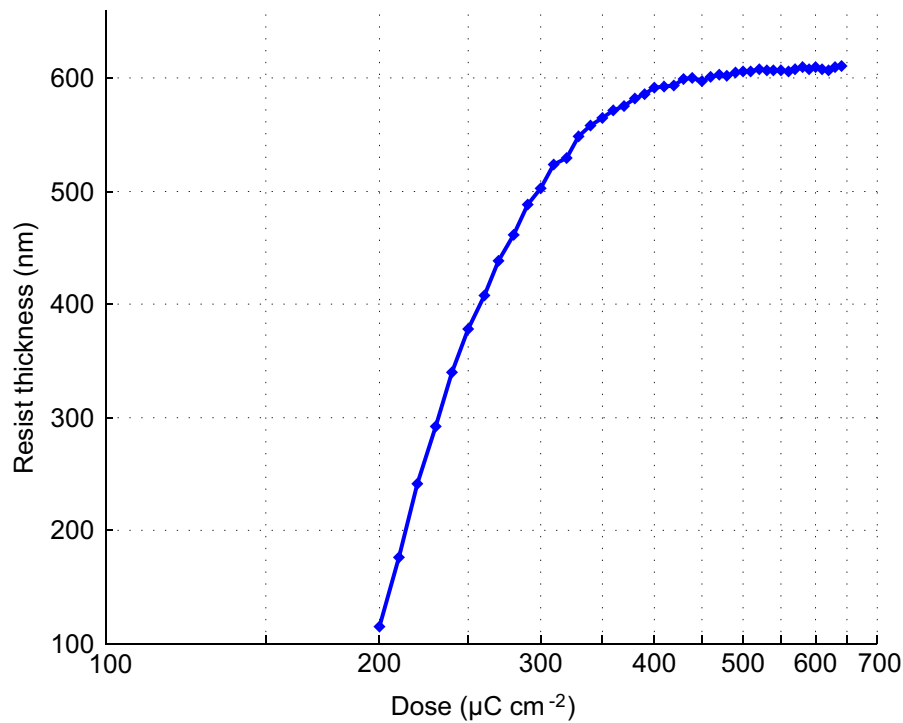


Figure 3.8: Residual HSQ resist thickness after development at different doses.

Furthermore, corners and closely separated spaces usually get under developed<sup>6</sup>, which is particularly detrimental for couplers and gratings. This effect is called the proximity error and generally it is regarded as the main limiting factor for EBL.

The explanation is as follow. During electron beam exposure, the electrons interact with the atoms of the resist or semiconductor. Apart from backscattered electrons there is a quantity of secondary electrons as an additional radiation source that decreases the contrast of the incident electron beam exposure. To demonstrate the effect, a Monte-Carlo simulation was carried out tracing one million electrons injected into a stack of PMMA/SiO<sub>2</sub>/InGaAs with an acceleration voltage of 50 kV by using a commercially available software called Skeleton. The resulting space/energy-density diagram in Fig. 3.9 shows that a significant exposure occurs even at distances, several microns away from the point of impact. Therefore, the effective dose on large exposed areas is increased by the background exposure from scattered electrons, which leads to a different correct dose depending on the different pattern densities.

<sup>6</sup>Actually they get underdeveloped using positive ebeam resist and overexposed using negative resist.

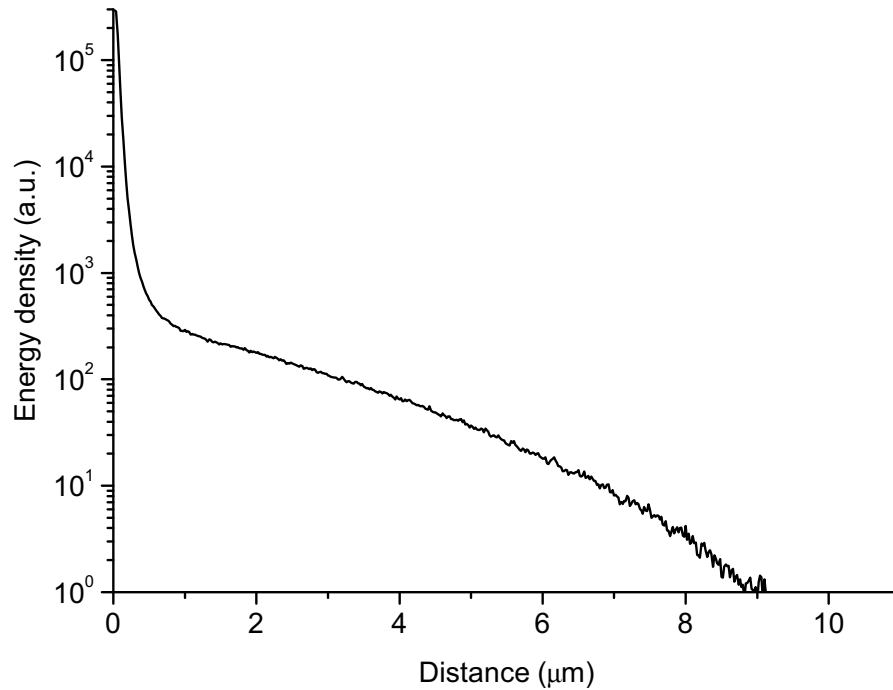


Figure 3.9: Energy density in a PMMA resist on top of semiconductor after 50 kV electron beam exposure at  $x = 0$ .

One simple solution would be using separate layers for the various patterns and expose them with a different dose. However, not only the complexity of the mask design increases but also stitching errors are likely to occur. After writing each layer the EBL tool realigns its position with respect to the markers and which can cause a displacement error in the order of 100 nm between layers. This can cause backreflection points all over the design, which can severely affect device operation. It is worth to point out that layer to layer stitching is completely different from field to field stitching ( $\sim 25 \text{ nm}$ ). If the total pattern size is larger than a field size (1.2x1.2 mm in the VB6) the tool has to mechanically reposition the sample to the next exposed area that – by nature – generates misalignment errors. However, the field to field stitching is much lower than the layer stitching and the devices can also be designed in such a fashion that no field boundary crosses important parts of devices (for example rings).

Fortunately, the proximity error can be corrected by assigning different dose values to edges and corners. Fig. 3.10 shows the idea of PEC and an SEM image of a developed grating in PMMA with poor contrast due to the proximity error. The dose-level on the edges of patterns can artificially be enhanced, as illustrated

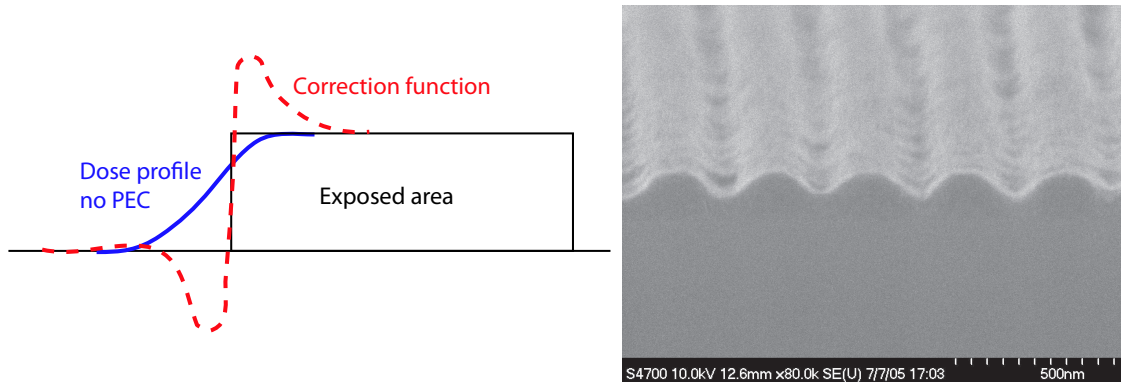


Figure 3.10: Illustration of PEC and an SEM image of a PMMA grating with poor contrast resulting from proximity error.

by the red curve.

The EBL tools have standard software tools for implementing PEC. The result of the Monte-Carlo simulation (shown in Fig. 3.9) is used by a software package called Proxecco to assign the corrected doses to the different features during the fracturing of the mask<sup>7</sup>. The assignment of different doses is clearly visible in Fig. 3.11 that shows an optical micrograph of an underdeveloped cross: the middle of large exposed areas have similar dose values, while higher and higher doses are assigned as we approach edges and corners.

### 3.5 Dry etching

As already discussed in Section 2.2, couplers are very sensitive to etch depth variations. Furthermore, the bending losses can be reduced to a negligible value by etching down to the core (detailed in Section 2.3). To tackle both problems, a selective dry etching was developed that etches InP but does not (or little) etch the core ensuring good control over the coupling ratio and low bending losses at the same time. This section is dedicated to present the details of etching development.

<sup>7</sup>Fracturing is the process when the vector-represented design gets transferred into small rectangles and triangles, a raw data suitable for the EBL tools.

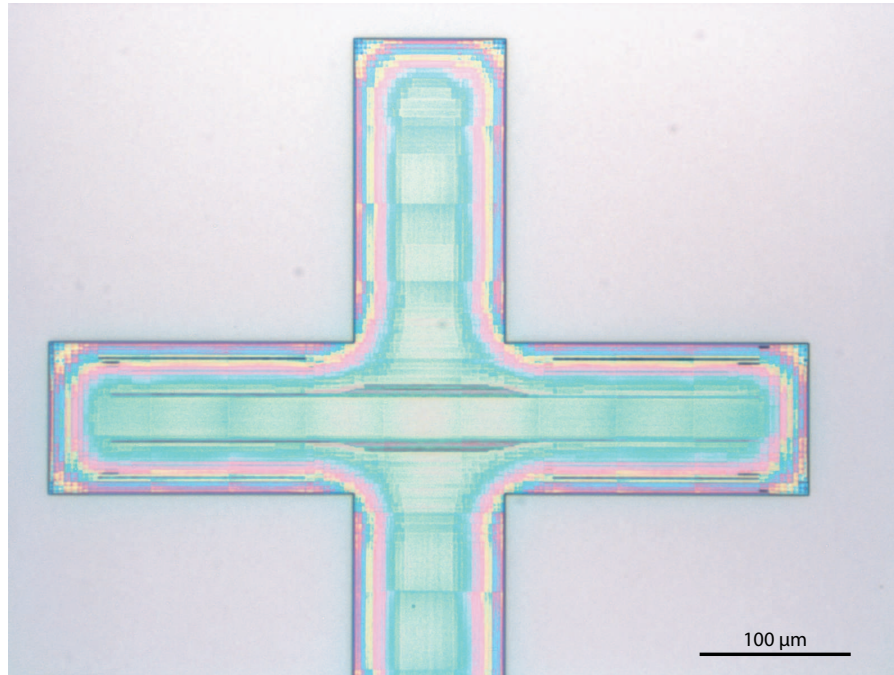


Figure 3.11: Optical micrograph of an underdeveloped alignment cross. The different colors indicate a difference in resist thickness due to dose assignment by PEC.

### 3.5.1 Selective RIE etching of InP over InAlAs in $\text{CH}_4/\text{H}_2/\text{O}_2$ plasma

There are several etching chemistries and technologies available to etch InP, such as ICP etching using  $\text{Cl}_2\text{-N}_2$  [64] or RIE etching with  $\text{CH}_4/\text{H}_2$  or  $\text{SiCl}_4$  [65, 66]. The most common chemistry is based on  $\text{CH}_4/\text{H}_2$  but etching is often accompanied by strong polymer formation, which limits the etch speed and verticality of the etched profile. A solution is provided by a cyclic process of etching with  $\text{CH}_4/\text{H}_2$  and polymer removal with  $\text{O}_2$ . Very high aspect ratios were achieved using this technique [67, 68].

Unfortunately, none of the previously mentioned etch chemistries give good selectivity over InAlAs, the boundary material (serving as electron confinement layer) between the upper cladding and the core. Two techniques were found to satisfy this requirement: one was developed at the University of Glasgow where an etch chemistry of HBr was used to achieve selectivity greater than 60 [69]. However, HBr is a very toxic gas, therefore it was excluded from the department's list of etch

gases years ago. The other technique uses  $\text{CH}_4/\text{H}_2$  with a little addition of oxygen to the mixture. The oxygen forms a thin layer of  $\text{Al}_2\text{O}_3$  by oxidizing the high aluminum content of the core and stops (or slows down) the etching [70].

Control of the etching depth was achieved by using the above mentioned method and optimized on our RIE tool, called ET340 – an RIE machine for methane based chemistry. Different etching runs were performed in  $\text{CH}_4/\text{H}_2/\text{O}_2$  plasma, varying both the relative flow rate of the gas mixture and the total radio-frequency (RF) power. Addition of  $\text{O}_2$  to the gas mixture decreases the etch rate but improves the sidewall verticality because it partially removes the polymer that forms during InP etching.

A preliminary result showed an InP etch rate of 55 nm/min and a selectivity greater than 10, but the sidewalls were not vertical, with an undercut in the top layer. Furthermore, the excess polymer formation gave nonlinear etching speed and therefore unpredictable etch depth.

Finally, a total RF power of 50 W, a pressure of 30 mTorr and a 6/54/0.6 sccm flow rate ( $\text{CH}_4/\text{H}_2/\text{O}_2$  respectively) gave the best etching results in terms of sidewall verticality. Furthermore, the etch rate on InP decreased to 35 nm/min, while the rate on InAlAs was only about 1 nm/min, corresponding to a selectivity greater than 30. Very little polymer formation was found, which resulted in a linear etching speed over time. SEM images in Fig. 3.12 show some examples of structures etched with the optimized<sup>8</sup> recipe.

Moreover, the set of parameters used gives very smooth etched surfaces as the etching stops on the InAlAs layer and flattens out any unevenness. An atomic force microscope (AFM) trace shown in Fig. 3.13 gives an insight into the smoothness of the resulting surface: less than 2 nm real mean square (RMS) surface roughness was found scanning over an area of  $2 \times 2 \mu\text{m}$  indicating an almost atomic level flatness.

### 3.5.2 Effect of RIE lag

In order to achieve small device dimensions, the waveguide coupling gaps were reduced, which gave a problem, called RIE lag or aspect ratio dependent etching (ARDE). Ions of the etching gas reach the bottom of a narrow gap with a smaller probability than into open areas, which consequently causes an area dependent etch rate. Furthermore, the sidewall verticality can be distorted, since the ions can bounce off from the sidewalls (ricochet effect). There is also an edge effect

---

<sup>8</sup>A process reoptimization was required after the move of dry etch facilities to the newly built James Watt Nanofabrication Centre.

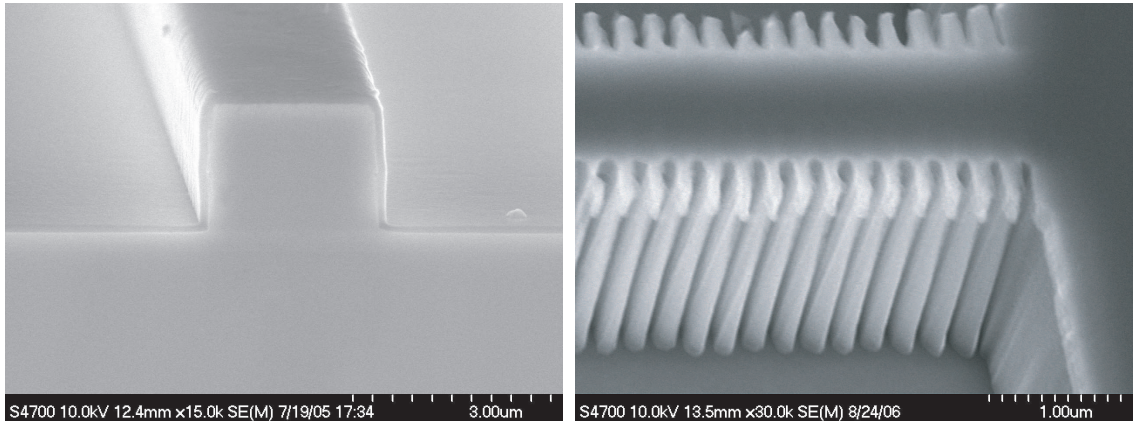


Figure 3.12: SEM image of etched waveguide and gratings using the optimized process.

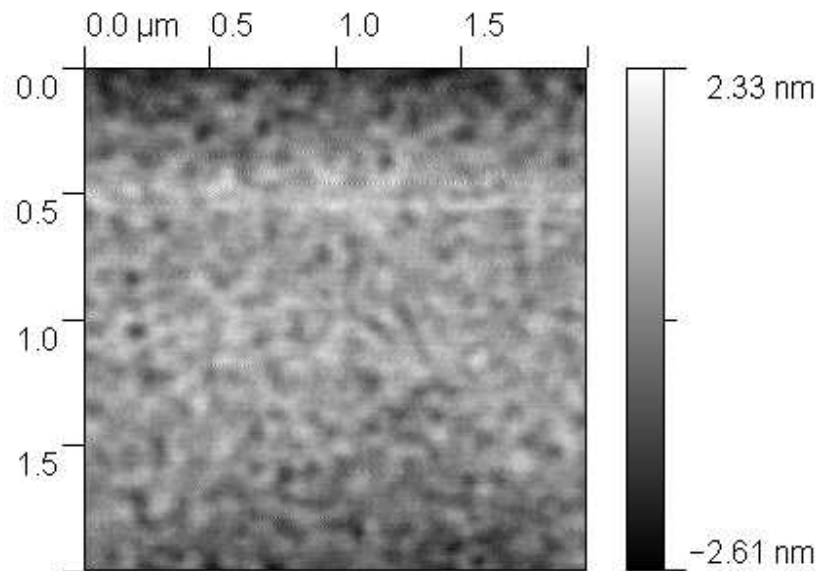


Figure 3.13: AFM trace about etched surface when etching reached the stop-etch layer.

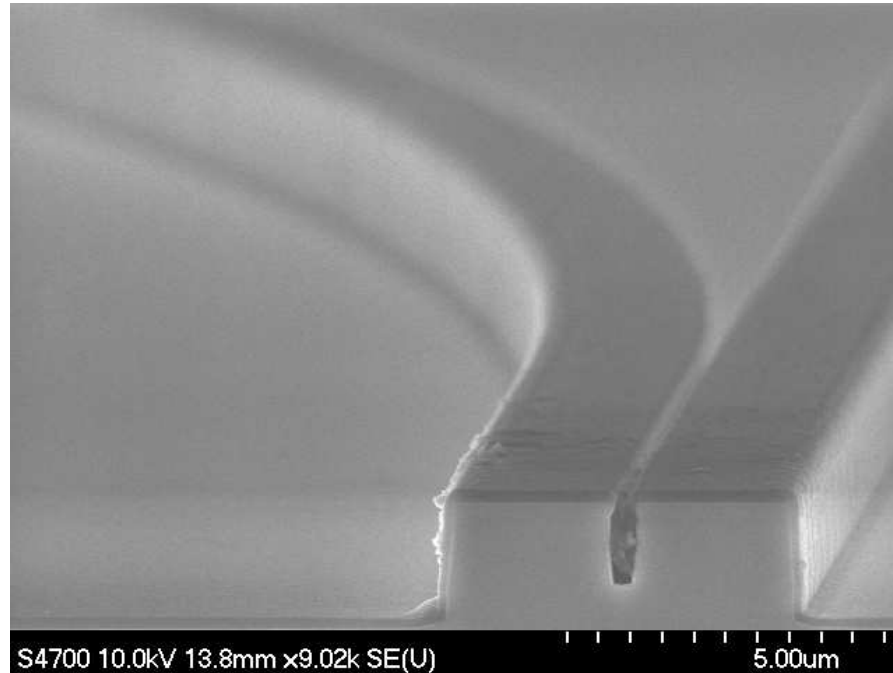


Figure 3.14: SEM image of a (not fully) etched 300 nm-gap coupler showing the effect of RIE lag.

that modifies the self bias potential distribution at the bottom of the gap, which further distort the etch profile. The inconsistent results from the measurement of test couplers led to the conclusion that RIE lag can cause a significant problem in precisely defining the coupling ratio. The results were further confirmed by SEM investigation of a coupler's cross section, as shown in Fig. 3.14.

To tackle the problem, a series of etching test were run using different etch times and coupler widths in order to measure the etch speed as a function of coupler gap width. The results in Fig. 3.15 show that coupler gaps below 900 nm show a significant decrease in etching speed with respect to open areas. Taking into account the process parameters, it can be calculated that fully etching of a 500 nm gap already requires a 20 mins over etching. Unfortunately, the electron confinement outside the couplers also get slowly etched, and – in order not to suffer from sidewall recombination – etching down to the QWs should be avoided. According to the calculation on etching speeds, this technology allows the etching of 500 nm gaps but not smaller without reaching the QWs.

The etch profile of gratings were also investigated, which also shows some decreased etch rates and a sloppy profile, as shown in Fig. 3.16. Since the profile

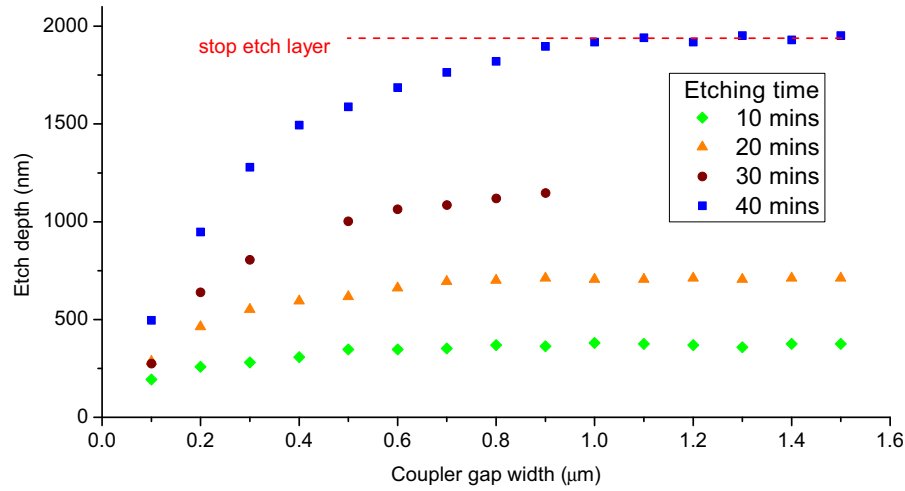


Figure 3.15: Etch depth inside coupler gaps as a function of coupler gap width and etch time.

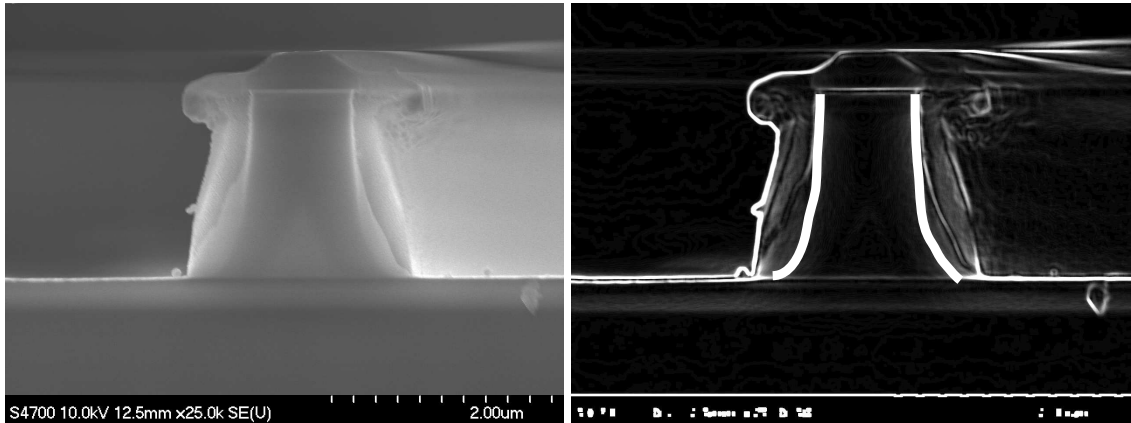


Figure 3.16: Cross-sectional SEM image of a grating and contrast enhanced image showing the etch profile inside the recess of the grating.

differs from the ideal, one must consider that the optical mode *sees* less the effect of the apodization, which in turn results in a reduced coupling coefficient.

Just to mention, using HSQ causes a further inconsistency in etching speed. It was found, that using HSQ reduces the etching speed despite the fact that HSQ is chemically inert to the etching gas (being similar to  $\text{SiO}_2$ ). The explanation was found to be as follow. With a positive electron beam resist, only small parts of the chips are etched: about  $30\ \mu\text{m}$  around the waveguides to save on ebeam writing time. On the other hand, HSQ is a negative resist and almost the total area of

the chip gets etched apart from the waveguides and some spacers between devices for protection. It means at least a ten times higher load for the etchants, hence the decrease in etching speed. On small test samples the same difference does not occur, so one must carefully consider this effect.

## 3.6 Contact metallization

Major process development was also carried out for p-contact metallization. The problem lies in the fact that usual electron-beam metal evaporation is highly directional and does not give a good coverage of sidewalls. Contacts deposited with this technique become unreliable because the thinner metal coverage on the sidewalls locally has a higher sheet resistance. Apart from the joule heat coming from the metallization contacting the semiconductor, sidewall metallization acts as several, parallel-connected tiny fuses: upon high injection levels a catastrophic failure of the contact occurs. Normally, the problem is eliminated by tilting the sample in two directions during deposition to cover both sides of straight waveguides<sup>9</sup>. In the case of ring lasers, however, a complicated continuous rotating-turning mechanism would be required.

Plasma sputtering of metals is a completely different physical process than evaporation and it was found to be a viable technique for p-contact metallization of SRLs. Sputtering is carried out in a moderate vacuum where high RF power is applied between the metal target and the wafer holder. The atoms of the assisting Argon gas get ionized and hit the target. The collision removes metal atoms, which then are accelerated towards the biased sample holder and sample.

According to the literature, the Ti/Pt/Au sequence of layers proves to be the best layer sequence for contacting InGaAs in terms of adhesion and contact resistance [71].

A series of tests and improvements were carried out to investigate the optimal chamber conditions, layer thicknesses and precleaning processes. The most convenient tool for contact resistance investigation is forming contacts in a transmission line model (TLM) pattern manner, as shown in Fig. 3.17. The gap between the 800x200  $\mu\text{m}$  metal pads are designed to be 10, 15, 20 and 25  $\mu\text{m}$ .

After metal deposition, lift-off and annealing, the resistances were measured between the contact pads. The slope of the contact resistance vs. gap provides the resistance value of the underlying semiconductor while its intercept with the

---

<sup>9</sup>The technique is called *rocking*.

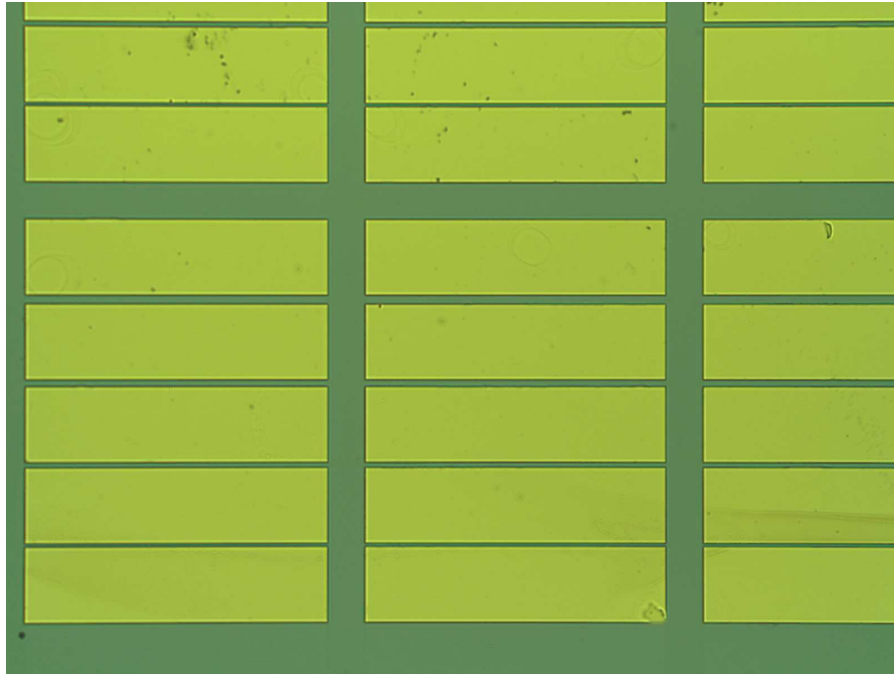


Figure 3.17: Optical micrograph of TLM patterns on InGaAs consisting of  $800\ \mu\text{m}$  by  $200\ \mu\text{m}$  sputtered Ti/Pt/Au metal pads.

y-axis gives the specific contact resistance. A set of measurements are shown for different annealing temperatures in Fig. 3.18. A minimum contact resistance of  $1.7 \times 10^{-3}\ \Omega\text{mm}^2$  was found for a 36/60/240 nm Ti/Pt/Au sequence of sputtered layers, respectively. This value means a contact resistance of about 2 Ohms for a 1 mm-long FP laser, which is just acceptable but certainly significant considering  $20\ \Omega$  for a  $100\ \mu\text{m}$  long contact. Especially when comparing this figure with values taken from the literature where two orders of magnitude lower contact resistances are usually reported.

Further developments and trials led to the identification of a machine fault, namely the cooling system for the target was blocked. Target cooling is utterly important for the very first Titanium layer because it tends to oxidize at higher temperatures even when only traces of oxygen are present in the chamber. After the timely down-time of the machine, the p-contact strategy was altered to as follows: Right after deoxidization, a first sequence of Ti/Pt/Au layer is deposited by electron beam evaporation. Right after, the sample is transferred to the sputtering tool where a final, thick ( $\sim 200\ \text{nm}$ ) layer of gold is deposited. The final technique includes the advantages from the two technologies: the first layers are of a very high

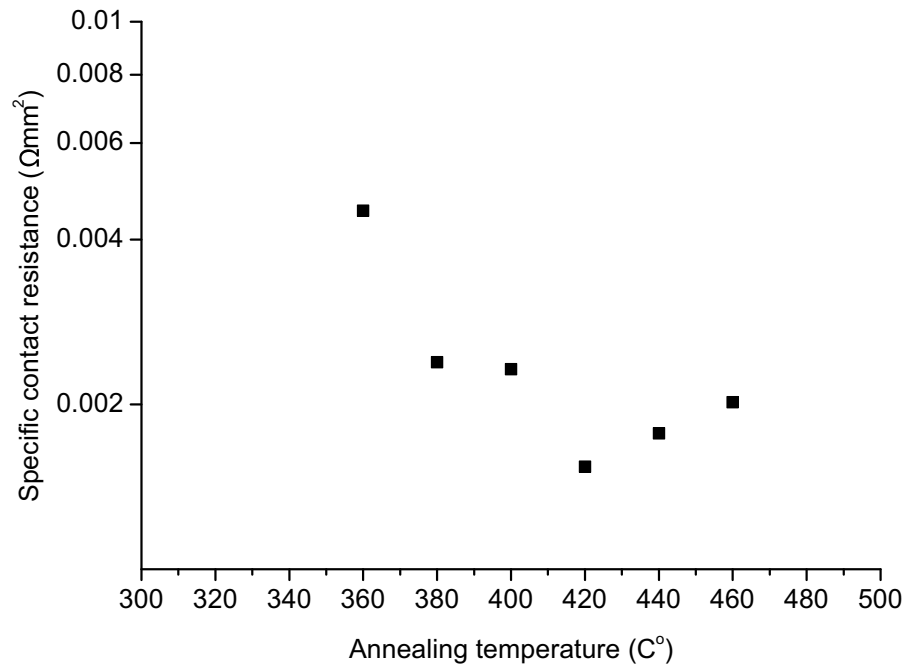


Figure 3.18: Specific contact resistance as a function of annealing temperature.

quality and purity while the final sputtered gold layer gives the uniform coverage of the waveguide sidewalls. Using this technique, contact resistances well below  $1\ \Omega$  were routinely measured.

### 3.7 Final steps

One of the final preparatory stages is thinning: to reduce the series contact resistance of the substrate and to ease the cleaving, the originally  $350\text{--}600\ \mu\text{m}$  thick samples are thinned down to a thickness of  $200\text{--}220\ \mu\text{m}$  after the top p-contact definition. The samples are glued topside down to a glass slide carrier using S1818 type photoresist spun at a low speed of 1000 rpm for 5 seconds. The subsequent 20 minutes of curing on a  $90^\circ\text{C}$  hotplate provides a good adhesion to the glass slide and ensures that the waveguides do not get damaged. The glass slides carrying the samples are then stuck to a metal rod and are rubbed against a glass plate using a colloid of water and  $9\ \mu\text{m}$  Alumina particles to promote thinning. After thinning, the sample is removed and thoroughly cleaned with Opticlear (wax removal), acetone and IPA.

Right after thinning, n-contact deposition, contact annealing and cleaving of

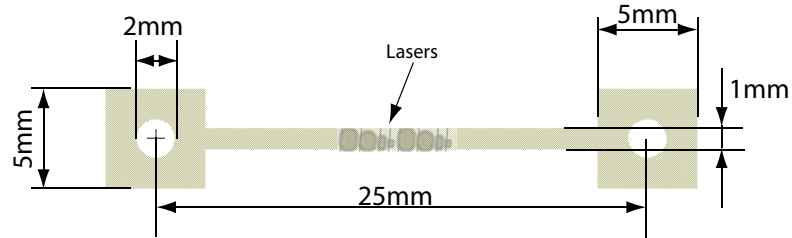


Figure 3.19: Schematic of the lasers glued to a sub-mount.

laser bars are carried out. The final preparatory step is mounting them on a suitable submount for characterization. A relatively easy and still reliable way of laser mounting is carried out by gluing the bars to a brass submount where the submount serves as the common negative contact of the lasers as well as for heat dissipation and mechanical support. After cleaning the mount with acetone, a two component conductive epoxy is applied to the surface, the bars are pressed on the top and they are cured on a hotplate for 5 minutes at  $90^{\circ}\text{C}$ . The schematic of the used sub-mount is illustrated in Fig. 3.19.

### 3.8 Full process flow chart

A final device looks as in Fig. 3.20 and shows a cross-sectional SEM image of a finished FP laser. Naturally, the full fabrication involves more and other fabrication steps, which neither were nor will be discussed later. A more complete fabrication scheme is illustrated in Fig. 3.21<sup>10</sup>, which includes all the steps, some necessary, other optional and recommended processing routes but without any processing details.

As a conclusion, the fabrication of semiconductor ring lasers was presented and detailed where major process development was carried out. In particular, an extensive e-beam process development on the relatively new HSQ resist was carried out, along with the optimization of the dry etching process to define vertical and smooth waveguide profiles. A highly selective reactive ion etching (RIE) technique was successfully developed to address both bending losses and fabrication tolerance of couplers. Finally, development of p-contact metallization for SRLs and issues

<sup>10</sup>I made available the process chart in MS Visio and PDF formats at <http://userweb.elec.gla.ac.uk/f/furst/> for further use.

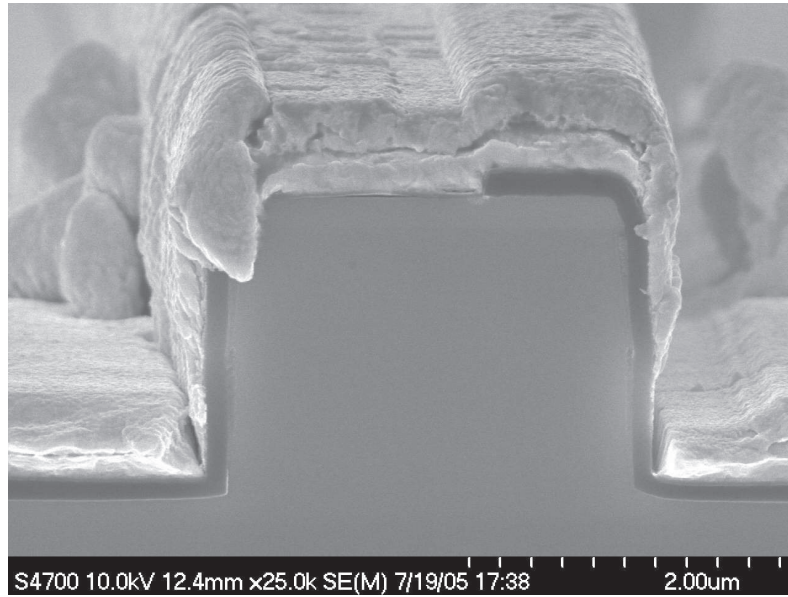


Figure 3.20: Final FP laser facet.

related to quantum well intermixing of quaternary material are discussed.

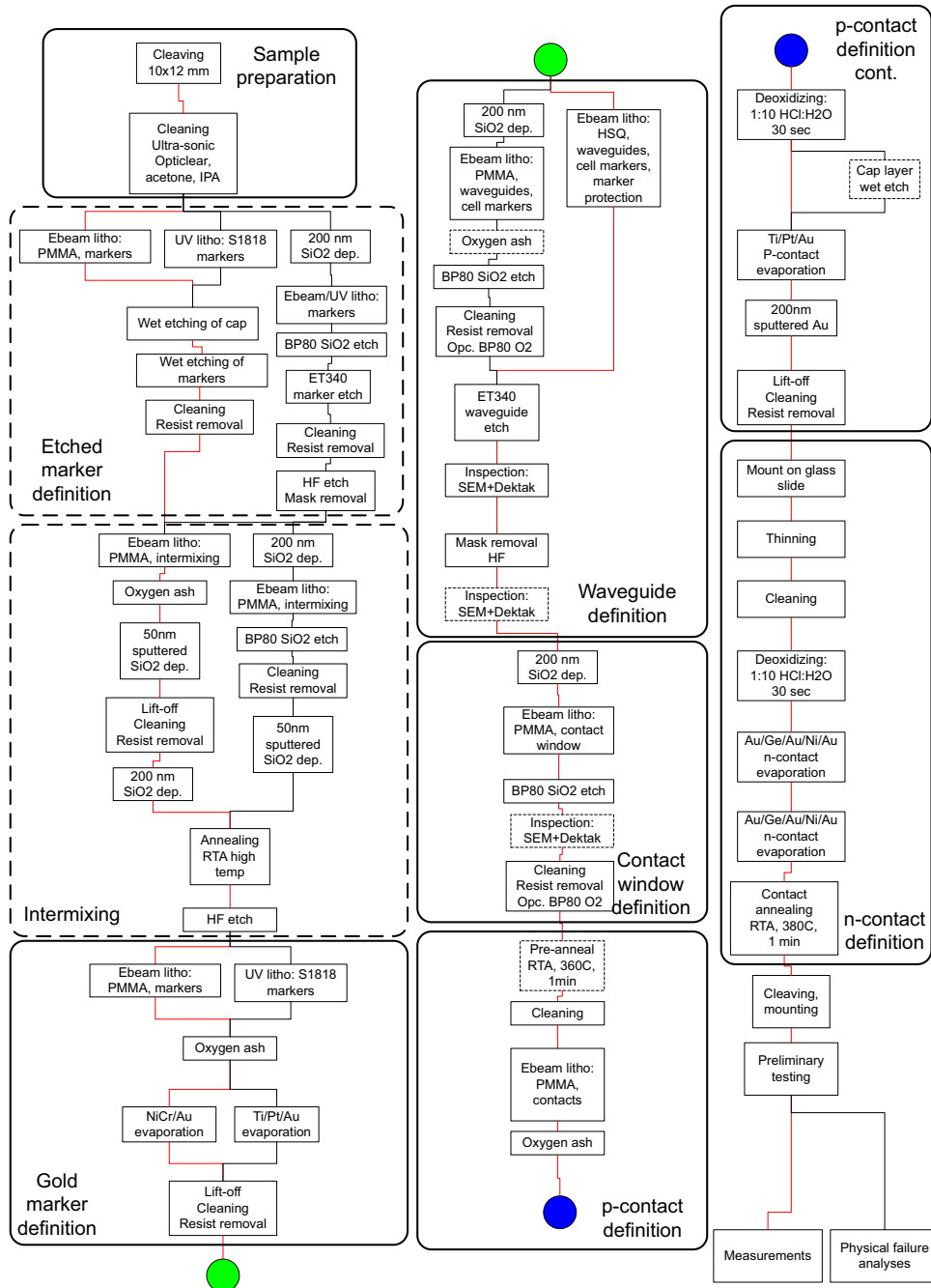


Figure 3.21: Full process flow chart for the fabrication of SRLs. Optional steps are enclosed with dashed line, while recommended route is indicated with red. Lithography steps include resist spinning, baking, exposure and development.

# Chapter 4

## Basic characterization

SRLs are more complex devices than conventional FP or DFB lasers and their optimum design requires a thorough optimization of a number of components, such as guiding mechanisms and couplers, along with a deeper understanding on the counter-propagating mode dynamics. This chapter reviews the basic material characterization and discusses the minimal dimensions – allowed by shallow etching – through the characterization of half ring lasers. Coupler properties are studied together with their tuning characteristics and the fabrication of DFBs and DBRs is reported. Finally cw characteristics of ring lasers are described, with an emphasis on their directional mode properties.

### 4.1 Material characterization

#### 4.1.1 Basic material properties

A precise assessment of the semiconductor material properties not only gives feedback to the grower but also provides significant information for the design of lasers. Furthermore, getting hold of the basic material parameters requires little fabrication effort and gives immediate information about the quality of the wafer.

The preliminary set of tests involves the assessment of the threshold current densities of broad area lasers (BALs). BALs consist of a wide ( $50\ \mu\text{m}$ ) p-contact stripe defined between two cleaved facets that provides the optical feedback for lasing action. The fabrication does not contain any etching steps and the mode is guided by the gain guiding mechanism provided by the pumped section. Because of the wide gain region, the edge effects and the current spreading on the side of the waveguide can be neglected, and the threshold current density is calculated by

Table 4.1: Summary of threshold current densities obtained from broad area laser measurements.

Wafer	MBE3183	MR2032	MR2254	MR2256	IQE IEGENS 13-17
$J_\infty$ (A cm <sup>-2</sup> )	1230	689	1082	731	208

considering the area of the pumped section. On the other hand, large pumped area increases the threshold current to a level where Joule-heat severely degrades gain, therefore, pulsed operation is required for the measurements.<sup>1</sup>

As an example, the results on BAL measurements for the material MR2256 are reported in Fig. 4.1. The data is plotted in such a fashion that an important (theoretical) quality factor – the threshold current density of an infinite long laser ( $J_\infty$ ) – can be graphically represented. The expression for  $J_\infty$  yields

$$\ln(J_\infty) = \frac{\alpha}{n\Gamma_w g_0} + \ln \frac{nJ_t}{\eta_i}, \quad (4.1)$$

where  $\alpha$  is the material loss,  $n$  is the group index,  $\Gamma_w$  is the confinement factor per well,  $g_0$  is the gain factor,  $J_t$  is the transparency current density and  $\eta_i$  is the internal quantum efficiency. These parameters give enough information to predict basic laser performance, such as threshold currents and external quantum efficiencies. However, to obtain the full set of parameters, we need to measure the external quantum efficiencies as a function of the cavity length. The full derivation of the equations is not reported here for simplicity but can be found in Appendix B.

The calculated material parameters were used to predict ring laser performance during the design stage (in Section 2.4). As a comparison, the threshold current densities of the different materials are summarized in Table 4.1. It is clearly visible that the IQE wafer provided much lower threshold current densities than previous batches. Further cw measurements of FP lasers confirmed the figures on the IQE wafer.

It is worth to point out that there is not always a direct correlation between BAL measurements and material performance under cw operation. Despite the strong PL peaks and the relatively low threshold current densities of the materials MR2254 and MR2256, the two wafers did not provide lasers that could be operated cw. The poor cw performance is most likely related to an insufficient confinement of the carriers into the QWs, which escape at elevated temperatures and cause a decrease

---

<sup>1</sup>Lasing under cw conditions can usually not even be achieved at room-temperature.

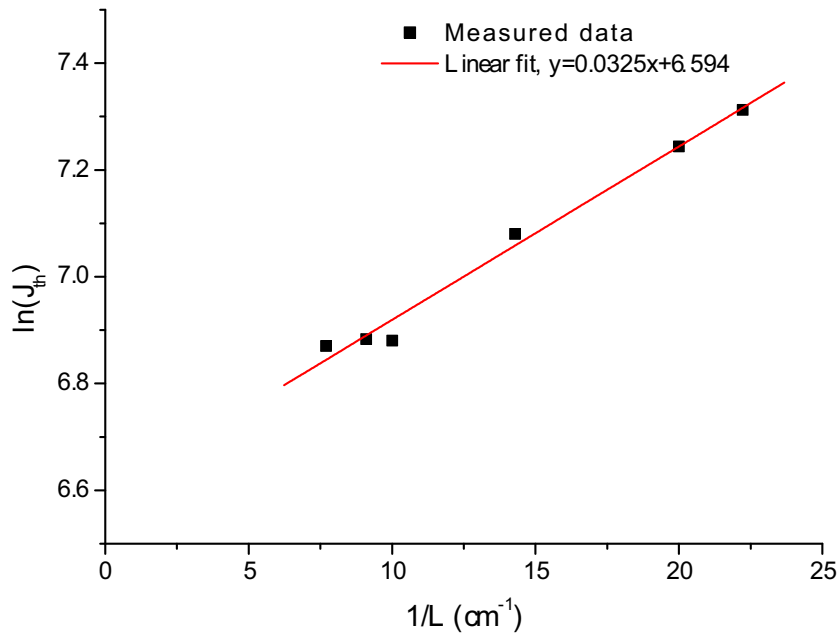


Figure 4.1:  $\ln(J_{th})$  as a function of  $1/L$  for material MR2256, where  $J_{th}$  is the threshold current density in  $\text{A cm}^{-2}$  of a BAL with a length of  $L$ .

in the gain. The origin of this effect is still unclear since both wafers contain carrier confinement layers and previously grown wafers proved very performing. The most likely explanation is that some problems occurred during the growth.

Several batches of RWG lasers showed the same effect, which led to the conclusion that the two wafers were not suitable for further device fabrication. Also, the stop-etch layer process did not work with the expected selectivity, which further confirmed that the problem could have been related to the bad growth of the InAlAs carrier confinement layer.

#### 4.1.2 Cw characteristic of RWG lasers.

After the BAL assessment and the extraction of the main material parameters, it is good practice to measure the L-I curves of FP lasers to evaluate the fabrication robustness and the characteristic temperature  $T_0$  of the material. Fig. 4.2 shows a set of LI curves on a 1 mm-long laser taken at different temperatures. Since the IQE material exhibited the best performance, it was used for fabricating the majority

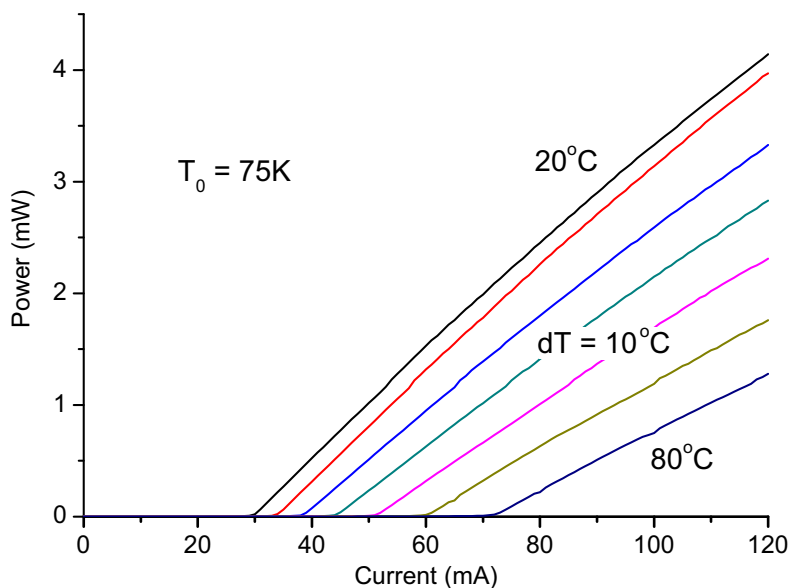


Figure 4.2: LI characteristic of a 1 mm long FP laser as a function of temperature.

of the devices reported in the following sections.<sup>2</sup> The threshold current densities of RWG lasers were found to be around  $J_{th} = 1 \text{ kA/cm}^2$  with an external quantum efficiency  $\eta_{ext} = 35\%$ , which are considered average on this material system.

Together with threshold current and output power, the temperature dependence of the threshold current is of significant importance. Increasing the operating temperature of the laser results in an increase of the threshold current, a relationship that can be approximated as

$$I_{th} = I_0 \exp \frac{T}{T_0}, \quad (4.2)$$

where  $T_0$  is the characteristic temperature. Plotting the threshold current values at different temperatures,  $T_0$  was found to be 75 K. This figure is good, although it is slightly lower than typical values reported for Aluminium quaternary material systems [40].

### 4.1.3 Waveguide loss/gain

The output waveguides of some of the SRLs reported in this work are left active. An electrical contact defined on the waveguides enables to either amplify the signal if

<sup>2</sup>Therefore it is the default material in the text, unless otherwise stated.

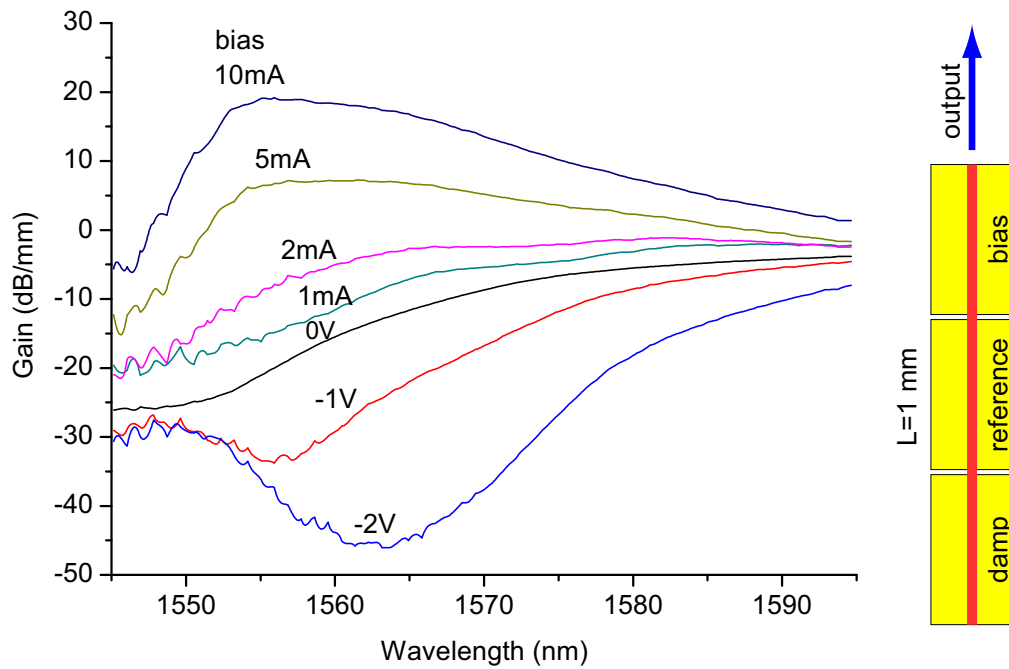


Figure 4.3: Gain (or loss) as a function of waveguide bias extracted from three section laser measurements.

more output power is required or to absorb most of the power if the optical feedback from the cleaved facets has to be minimized. Therefore, a precise assessment of the waveguide gain or loss level at different electrical biasing levels is of crucial importance to evaluate the SRL performance.

These figures can be extracted from three section laser measurements. A 1 mm-long FP laser, with three separately biasable sections with identical length  $L$  was used as follows: One output is aligned with a lensed fiber and connected to an optical spectrum analyser (OSA), and the section next to it is forward-biased to a value of typically 30 mA. At the same time the other end of the laser is strongly reverse biased to damp the cavity and prevent lasing action. Once the reference is taken, the same current is applied to the middle section and the other section next to the fibre can be biased to any desired current or reverse voltage values to decrease or increase losses of the output section. Measurement of the output spectra normalized to the reference provides the gain/loss values at different bias levels as a function of the wavelength. The results do not depend on the losses coming from fiber misalignment and connectors because the reference already accounts for them. The results are plotted in Fig. 4.3.

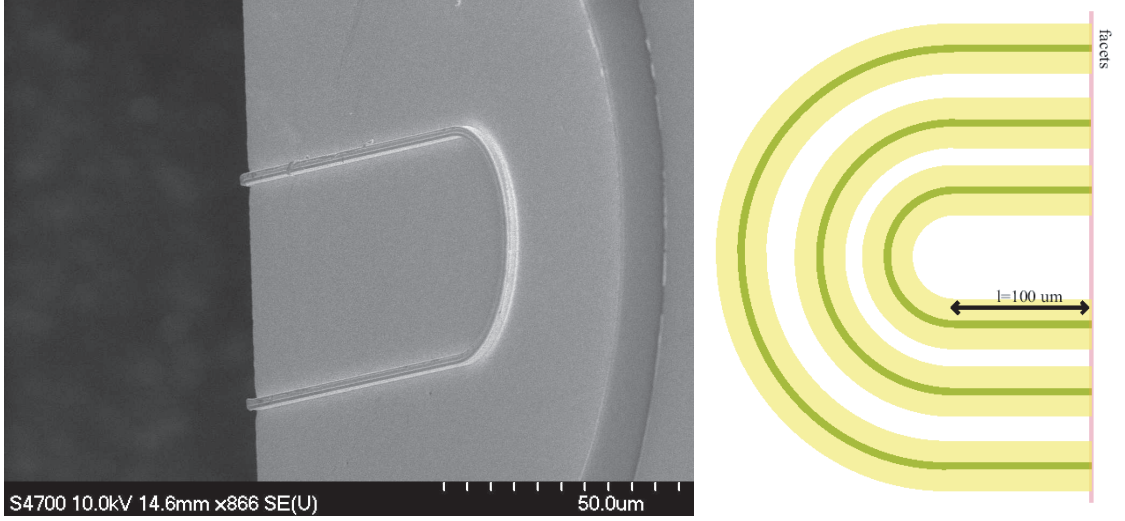


Figure 4.4: SEM image of a half ring laser without contact metallization (left) and schematic of devices with different ring radii (right).

## 4.2 Bending loss assessment

### 4.2.1 Half ring lasers

Probably the most accurate way for assessing bending losses is provided by the measurements of the current thresholds of half-ring lasers with decreasing bend radii. A half ring laser comprises a half ring shaped waveguide joined with two straight sections ending in cleaved facets forming a Fabry–Pérot cavity, as shown in Fig. 4.4.

Half rings, with ring radii ranging from 150 to 600  $\mu\text{m}$ , and length of the straight section of  $l = 100 \mu\text{m}$ , were first fabricated on the MR3186 material structure. The measured threshold currents and external quantum efficiencies are reported in Fig. 4.5. A minimum value of the threshold current of 34 mA is obtained for a ring radius of 150  $\mu\text{m}$ .

In order to validate the bending loss simulation results (in Section 2.3), the *gain equals loss* equation has to be modified to account for bending losses, waveguide losses and output facets:

$$L_{\text{cav}} n \Gamma_{wgth} = L_{\text{cav}} \alpha_0 + \ln \frac{1}{r} + \pi r \alpha_b(R), \quad (4.3)$$

where  $L_{\text{cav}} = 2l + R\pi$  corresponds to the cavity length and  $r$  is the reflectivity of the mirrors. The simulation described in Section 2.4 was repeated with the modified

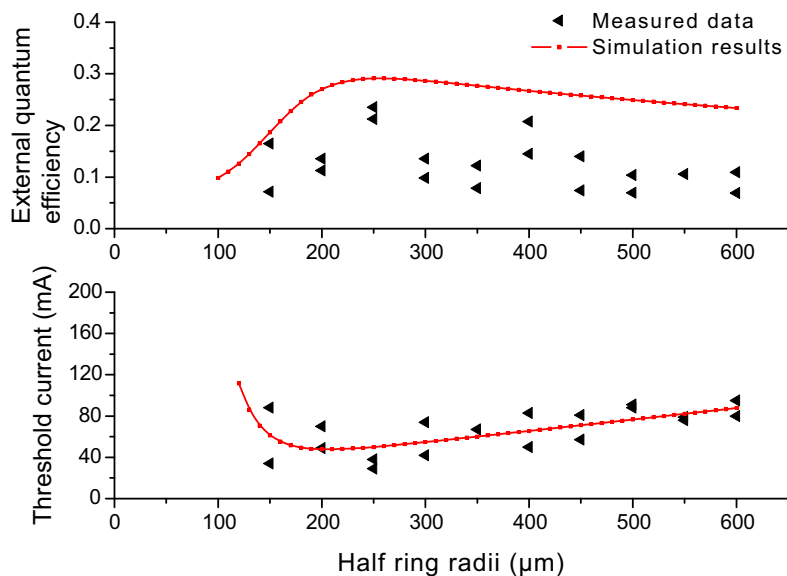


Figure 4.5: Measured and simulated half ring laser thresholds and external quantum efficiencies fabricated from the *3168* material.

equation ( $l$  is fixed to  $100\ \mu\text{m}$ ), and assuming a facet reflectivity of  $r = 0.31$ . The measurements show a good match between the experimental and simulation results, as depicted in Fig. 4.5.

Surprisingly, some devices show threshold currents and bending losses lower than the simulated values. A reason for this might be due to the cleaving: to save chip space, the half rings were obtained by cleaving into half full-ring devices with straight sections (i.e. racetrack shaped devices). A misalignment in cleaving can result in devices with the same radii but different straight section length, which would give pairs of devices with higher and lower threshold currents than the nominal value. Indeed, Fig. 4.5 shows such pairs.

Furthermore, the external quantum efficiencies show the same trend as the simulation, although the measured values are lower than expected. It can be explained by the impossibility of collecting all the light emitted by the devices, especially in this case, where there are two outputs on the same side of the devices, and the photodetector area was only a few  $\text{mm}^2$ .

As a comparison, threshold currents of half ring lasers fabricated on the IQE material are plotted in Fig. 4.6. The first thing to note is the lower achievable bending radius without a major penalty on the current thresholds. In the case of the MR3186 material, the trend shows a minimum threshold current at a radius of

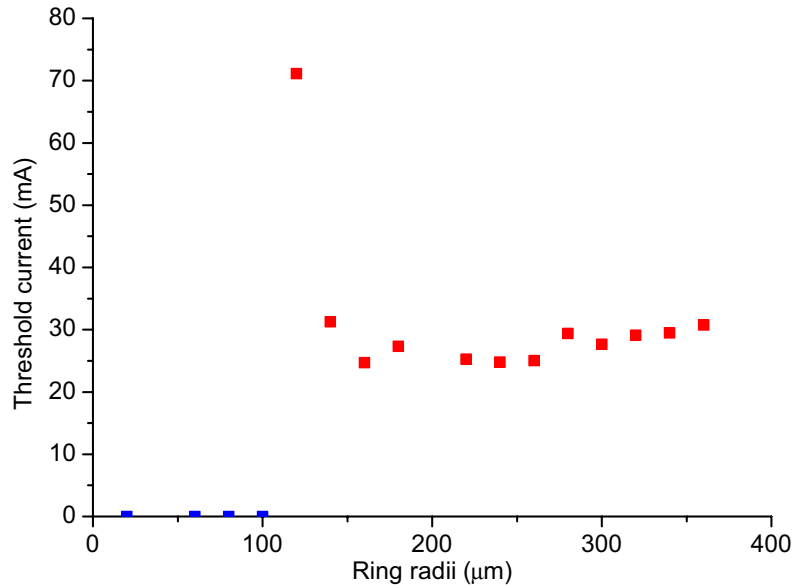


Figure 4.6: Threshold currents of half ring lasers fabricated on the IQE material.

200  $\mu\text{m}$  while the same figure goes down to 150  $\mu\text{m}$  for the IQE material. This slight change is accounted for the increased confinement of the IQE material: etching down to the core provides an effective refractive index difference  $\Delta n = 0.055$  for *MR3186* and  $\Delta n = 0.064$  for the IQE, respectively. An optimized design of the wafer structure with higher refractive index difference could provide devices with ring radii smaller than 100  $\mu\text{m}$ . For the purposes of the present work, however, smaller ring radii were not necessary.

#### 4.2.2 Cw characterization of SRLs with different radii

As a first confirmation of the previous results, a set of SRLs – with 100  $\mu\text{m}$ -long couplers and 1  $\mu\text{m}$ -wide gap – was tested. The threshold currents follow the expected trend, as reported in Fig. 4.7. Below a ring radius of 160  $\mu\text{m}$ , the threshold current values strongly increase while no lasing was found at a radius of 100  $\mu\text{m}$  or below.

The lasing wavelength is also plotted, which indicates the same trend: higher pump rate is required to compensate for higher losses per unit volume. Thus, the carrier distribution is shifted towards higher energies/lower wavelength.

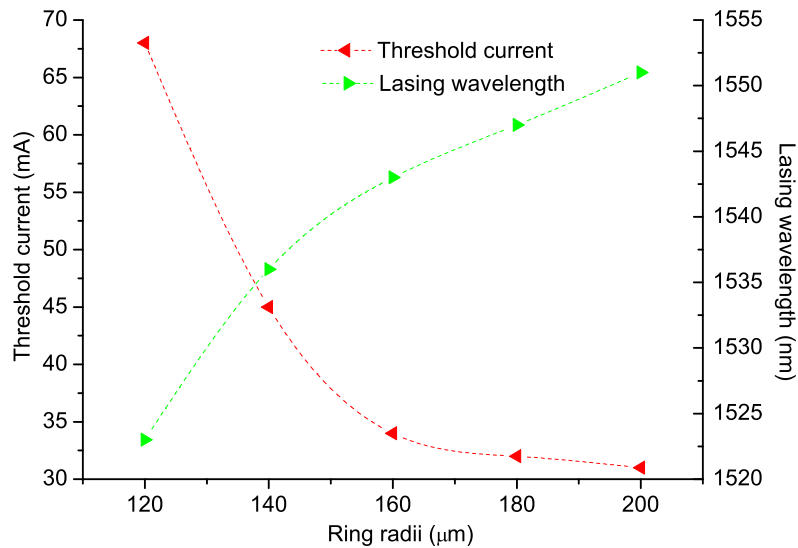


Figure 4.7: Threshold current and lasing wavelength at  $1.1 \times I_{th}$  as a function of SRL radii.

## 4.3 Couplers

### 4.3.1 Passive couplers

As said before, couplers are probably the most critical parts of SRLs. Apart from low intra-cavity backreflection and mode perturbation, they need to provide an acceptable coupling factor. In the previous chapter, most of the fabrication tolerances/problems related with evanescent couplers were discussed in detail, while the present section will report on their characterization.

A set of separate evanescent field couplers were fabricated exclusively for testing purposes. As shown in Fig. 4.8, the coupler is connected to two output arms on each side, all of them accessible through the cleaved ends of the chip for transmission measurements.

$1\ \mu\text{m}$ -gap couplers with a length ranging from 0 mm (point-coupler) to 1 mm were tested using the setup shown in Fig. 4.9. The output of a tunable laser was transmitted through a polarizing beam splitter to maintain TE polarization. The signal was modulated by a mechanical chopper and focused by an objective lens into one of the input waveguides. The output signal was collected by an other objective lens at the back facet and measured with an InGaAs photo-detector (PD). The signal from the PD was connected to a lock-in amplifier, which eliminates most of the ambient noise. The measurement of both outputs was carried out by focusing

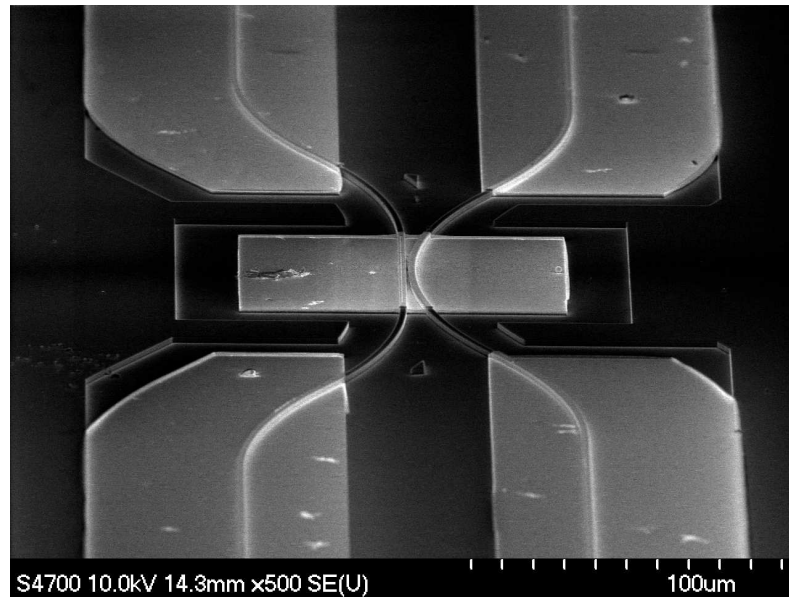


Figure 4.8: SEM image of a point coupler designed for coupling ratio measurements.

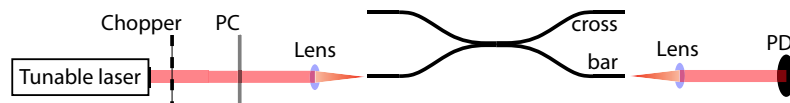


Figure 4.9: Setup for transmission measurements. (PC = polarization control, PD = photo detector)

onto either the bar or cross outputs with the help of a charge-coupled device (CCD) infrared camera.

The designed and measured coupling ratio values are plotted in Fig. 4.10. Apart from the  $800\ \mu\text{m}$ -long coupler, the measured coupling ratios show a good match with the designed values. Furthermore, the wavelength dependence of the coupling was investigated and it was found that the coupling changes only a few percent in the wavelength range of 1550–1570 nm.

### 4.3.2 Tunability

As discussed earlier in Section 2.2.4, evanescent field couplers have the potential for tunability. Fig. 2.12 suggested that a change in the effective refractive index of one of the waveguides is sufficient for a detuning of the coupler from 100% to almost 0%. The detuning was realized and tested using two techniques, namely

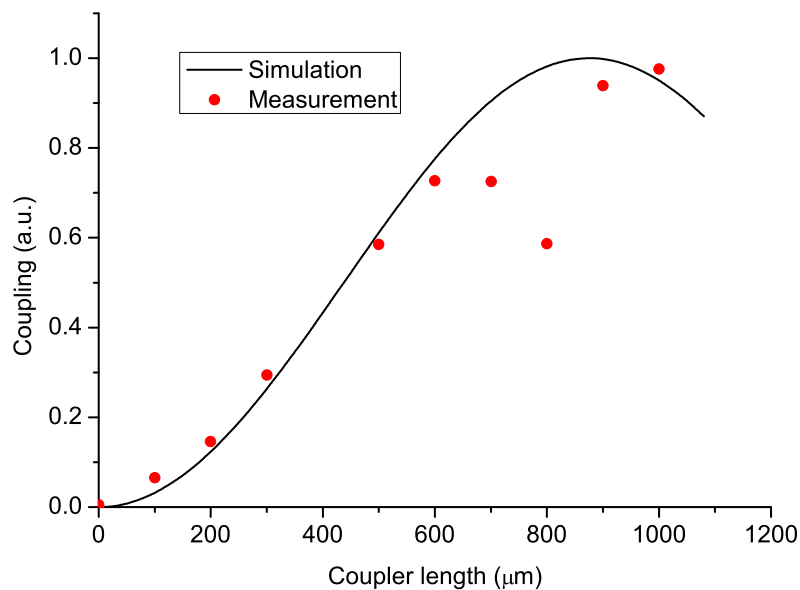


Figure 4.10: Measured coupling ratios and designed values for different coupler length at a wavelength of 1560 nm.

injecting current into one of the waveguides to achieve refractive index change due to the free carrier plasma effect and secondly by reverse biasing the waveguide to change the refractive index by quantum confined Stark effect (QCSE) [40].

Using the same measurement technique as for basic coupler characterization, current was injected into the bar<sup>3</sup> waveguide of a 900  $\mu\text{m}$ -long coupler while the coupling was measured. From a fabrication point of view, a contact window is opened on one waveguide only so that the applied electrical biasing generates the required refractive index difference between the waveguides. Fig. 4.11 shows the results as a function of the bias current. It can be seen that current values as small as 6 mA are sufficient for reducing the coupling ratio from 95% to 8%. Furthermore, the coupling at higher currents follows the trend of the simulation (shown earlier in Fig. 2.12) with minor differences. First noticeable difference is that the coupling never reaches zero, which is explained by a strong crosstalk between the two waveguides. The simulation did not include the effects of scattering, which could lead to coupling to higher order modes in the neighboring waveguides, thus resulting in crosstalk. This is further supported by the fact that crosstalk depends on the length of the coupler: a shorter (300  $\mu\text{m}$ -long) coupler could be tuned from an initial coupling ratio of 29.5% down to a minimum of 2% coupling, a value that

<sup>3</sup>See Fig. 4.9 for layout.

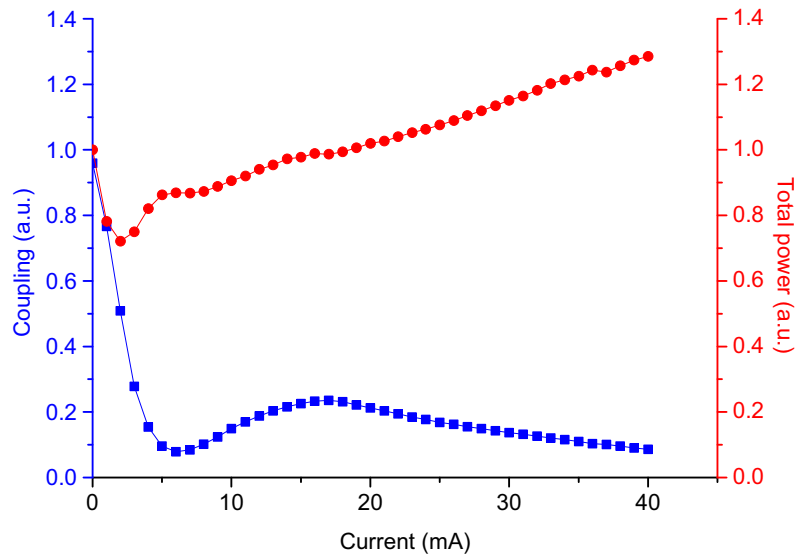


Figure 4.11: Coupling ratio as a function of the tuning current for a  $1\ \mu\text{m}$ -gap,  $900\ \mu\text{m}$  long coupler when the current is injected into the bar waveguide.

is smaller than in the previous case.

The total power<sup>4</sup> emerging from the outputs was also plotted in Fig. 4.11 that shows some peculiarities. If one considers only gain, losses and change in coupling ratio the minimum in the transmitted coupling power at 3mA can not be explained. Without getting into the details, let us consider the fundamental modes of the two waveguides, and the supermode in the coupled waveguide structure. I called it supermode because it is only present when the two waveguides are in close proximity – it accounts for the power transfer –, but alone it is not a guided-mode, only the overlap of fundamental modes’ evanescent tail. During the power transfer process the power is transferred from one waveguide to the other waveguide through the supermode. This mode carries the most power when there is equal power in the waveguides, i.e. at a coupling ratio of 50%. At the end of the coupler, the two waveguides are quickly separated and the power in the supermode gets radiated, resulting in power loss.<sup>5</sup> Indeed, the total power shows a minimum when the coupling ratio is tuned down to 50%. It should also be noted that for current values exceeding 20 mA, the output power gets slightly amplified.

Voltage tuning was realized by reverse biasing the cross<sup>6</sup> waveguide of the cou-

<sup>4</sup>The total power was normalized to the unbiased case.

<sup>5</sup>A similar situation occurs when the length of an MMI coupler is not properly designed.

<sup>6</sup>See Fig. 4.9 for layout.

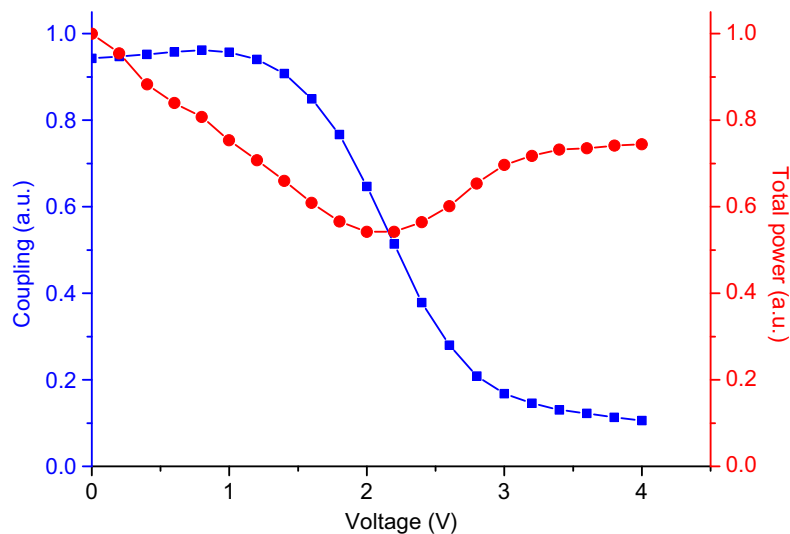


Figure 4.12: Coupling ratio as a function of the tuning voltage for a  $1\ \mu\text{m}$ -gap,  $900\ \mu\text{m}$  long coupler when the reverse voltage is applied onto the cross waveguide.

pler. A similar change in the coupling ratio was found as with the current tuning. Coupling is decreased to 8% by applying 4 V, as shown in Fig. 4.12. In this case, the total power shows a decreasing trend down to 50% coupling because of two effects: increasing the reverse voltage increases the losses in the cross waveguide, while the total loss of the coupler increases due to loss of the supermode's power at the end of the waveguide. Further tuning decreases the power that travels in the lossy waveguide and – at the same time –, the total coupler loss gets decreased. Finally, the power reverts back to about 80% of the original power. The residual loss is due to crosstalk with a very lossy waveguide and due to the fact, that the two waveguides are still electrically connected. The latter can be responsible for a saturation of the tuning mechanism in both the voltage case (the other waveguide gets slightly reverse biased) and the current injection (carrier diffusion to the other waveguide). The measurements were carried out at 1580 nm.

The two configurations of measurements were carried out by having two applications in mind. Current injection into the bar waveguide is suitable for Q-switching experiments, where a strongly damped ring cavity (100% coupling and additional loss from a non-pumped waveguide) could be quickly changed to a lower coupling with decreased cavity losses. While reverse biasing the cross waveguide is suitable for an electro-optic switch, where a maximum coupling could be quickly decreased to a very low coupling with additional losses on the output resulting in a high con-

trast between the on and off states. Of course, the configuration can be changed (injection into cross or reverse biasing the bar waveguide) but the effect of coupling change would be counteracted by the gain or loss.

## 4.4 DFB lasers

### 4.4.1 Cw characterization

Since the devices presented in the following chapters will include the integration of SRLs with DFBs and DBRs, the fabrication robustness and accuracy of gratings was carefully assessed. A set of 800  $\mu\text{m}$ -long DFBs with a pitch size ranging from 235 nm to 250 nm were fabricated and measured. The period of the gratings was provided by the simulation results described in Section 2.5. Threshold currents in the range of 17–25 mA and lasing in the range of 1500–1572 nm was found, which is a further indication of the large gain bandwidth of the IQE material.

The designed and actual lasing wavelength as a function of pitch size is plotted in Fig. 4.13. It can be seen that the actual lasing occurs at a wavelength that is 2–10 nm lower than the designed value. In the case of a non-perfect etching of the grating, the modal index would increase resulting in an enlarged emission wavelength. Therefore, the difference in wavelength is accounted by errors coming from the 2D simulation.

The spectra of the DFBs were also measured and SMSR values of 45–52 dB were found, which are amongst the best reported values, especially considering the un-coated facets and the absence of phase matching section. The spectrum of a DFB with a lasing wavelength of 1571.8 nm is plotted in Fig. 4.14. A further cw measurement was carried out on the optical linewidth, which was found to be in the order of 5 MHz.

### 4.4.2 Tuning properties

In Section 6.1, a device comprising an integrated SRL and DFB will be reported to demonstrate optical injection locking. Therefore, a preliminary assessment of the tuning properties of DFBs are reported. First, the lasing wavelength was precisely measured as a function of the injection current. The wavelength change per unit current is plotted for DFBs emitting at different wavelength in Fig. 4.15.

It can be seen, that tunability values around 1 GHz/mA was found across the whole wavelength range. The value indicates a small change in refractive index as a

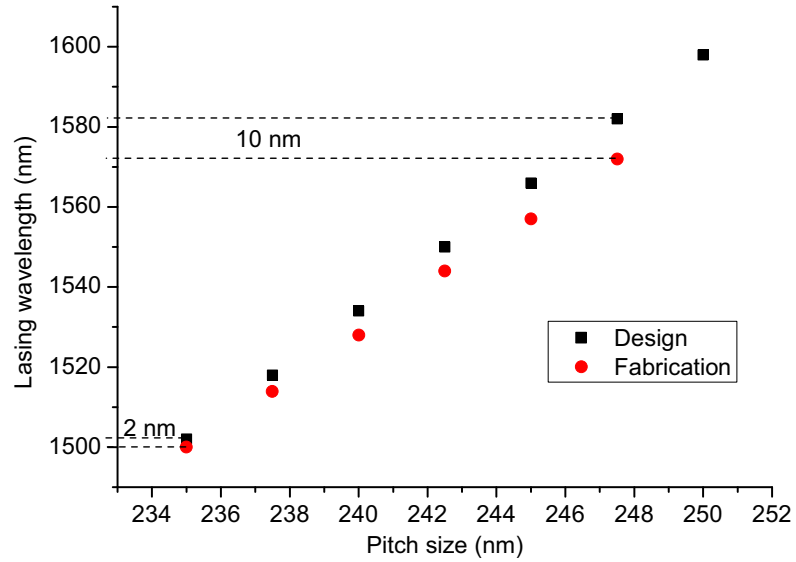


Figure 4.13: Designed and measured lasing wavelength of 800  $\mu\text{m}$ -long DFBs as a function of the pitch size.

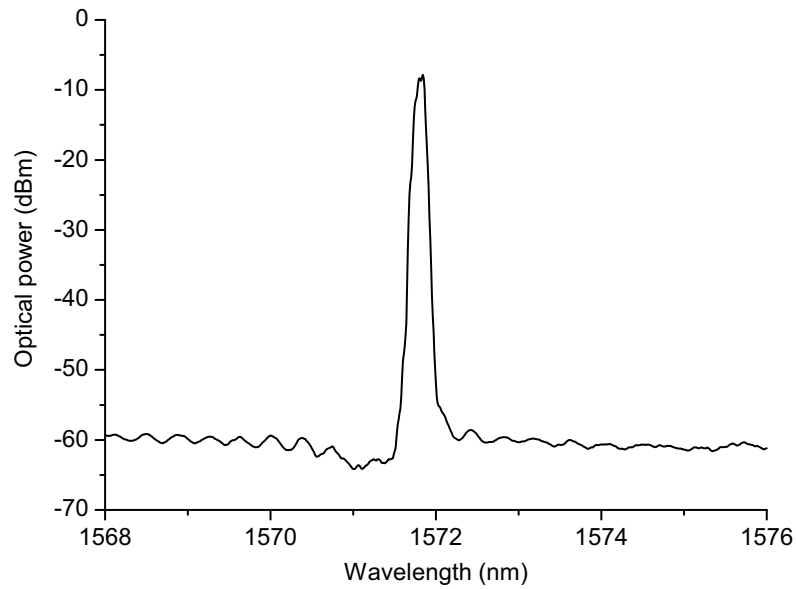


Figure 4.14: Optical spectrum of a DFB.

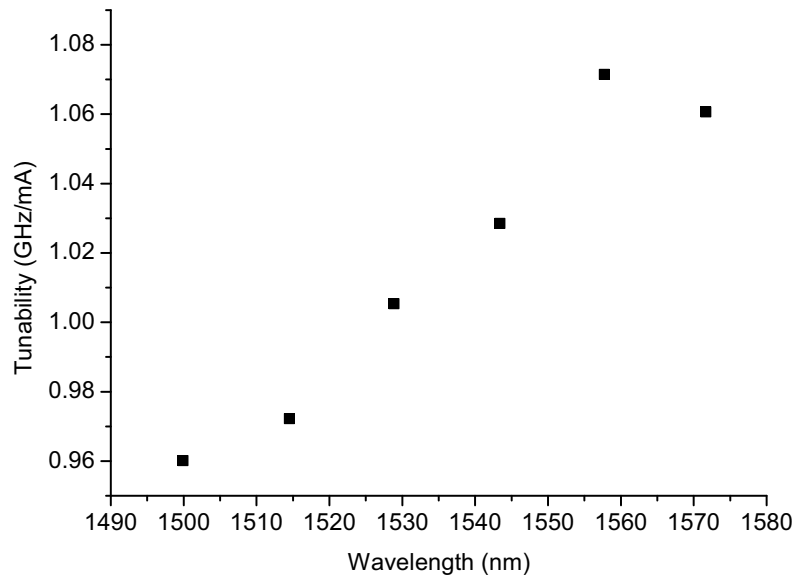


Figure 4.15: Tunability of DFBs as a function of lasing wavelength.

function of the carrier density, which is due to the linewidth enhancement or alpha factor of approximately 3 [72]. Detailed measurements of the alpha factor for the SRLs fabricated on the IQE material are reported in Appendix C. Low alpha factor is usually advantageous for high-speed direct modulation of single emitters but it limits their wavelength tunability by current injection. Considering the typical tunability figures, and a maximum current tuning range of 80 mA, one would span over only one cavity mode of an SRL with a FSR of 50 GHz.

The high speed response from a DFB was also measured, and a 3 dB cut off frequency of 825 MHz was found (the modulation response at 1 GHz is shown in Fig. 4.16). The relatively low cut-off frequency is due to the electrical configuration, which was not designed for high-speed operation. Modulation at higher frequencies can only be achieved by designing proper microstrip lines and p-contact in a ground-signal-ground configuration, which is outside the scope of this thesis.

The properties of passive gratings in a DBR+SRL configuration is discussed later in Section 6.2.

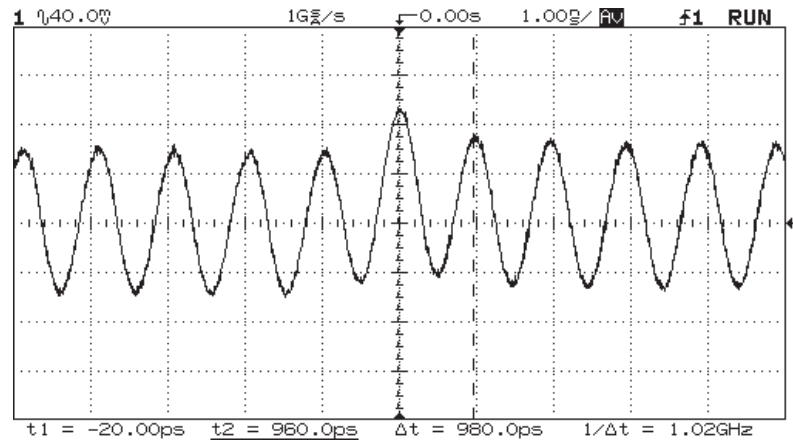


Figure 4.16: Modulation response of a DFB at a frequency of 1 GHz, with 5 mA current modulation, DC bias of 60 mA.

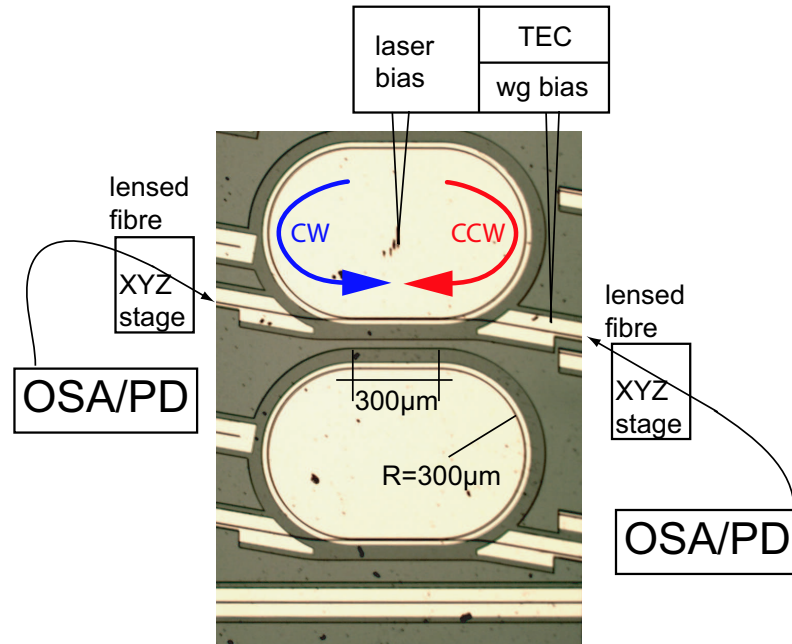


Figure 4.17: Setup used for testing SRLs.

## 4.5 Operating regimes of semiconductor ring lasers

### 4.5.1 Directionality

Using the setup shown in Fig. 4.17, the two counter-propagating (named clockwise (CW) and counter-clockwise (CCW)) modes of an SRL can be simultaneously recorded. The fibers used to couple the output signals are rotated to the correct angle (approximately with rotary stages) and aligned with XYZ stages. Biasing of the sections was carried out using standard metal probes while the temperature was kept constant at room temperature using a thermo-electric cooler (TEC). The LI-curve of a ring laser – with a ring radius of  $300\ \mu\text{m}$  and a coupler length of  $300\ \mu\text{m}$  – is plotted in Fig. 4.18.

So far, apart from the different cavity design, it was not discussed in detail how and why ring lasers are very different from normal Fabry-Perot lasers. A first peculiarity appears from the LI curve that shows several operating regimes as the current is increased. Just above threshold, the two counter-propagating modes lase simultaneously (region I); as the current is increased, the two modes undergo out-of-phase oscillations at frequencies around 100 MHz (region II). A further increase of the current, leads to complete unidirectional operation, in which only one direction

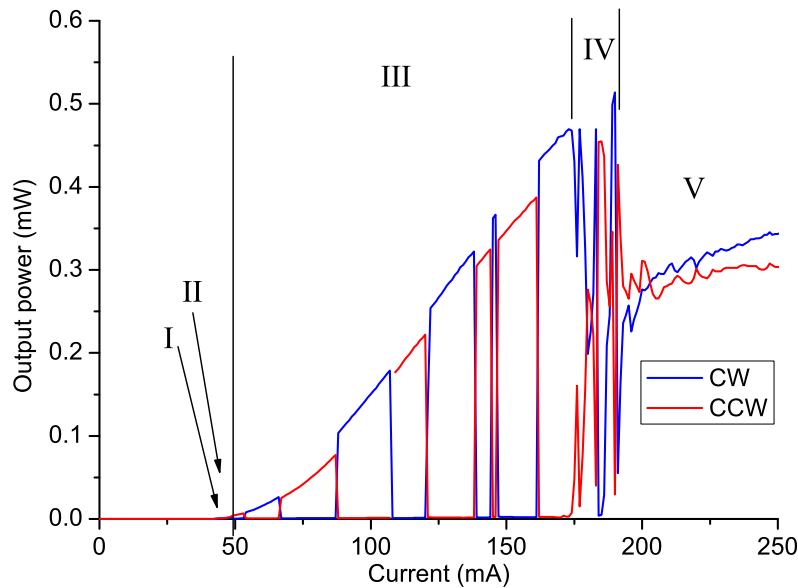


Figure 4.18: LI curves of a  $300\ \mu\text{m}$  radius ring laser with one  $300\ \mu\text{m}$  long coupler for the two directions.

lases at a time, while the other is suppressed. The unidirectional regime is followed by a highly unstable and an other bidirectional region. Region IV and V will be discussed later in Section 5.3.

The most interesting regime of operation is the unidirectional (Region III), which will be discussed more in detail. Considering a symmetric structure, traveling wave operation along one direction is only possible when the roundtrip gain of one direction gets suppressed through cross-gain saturation effects. It is worth to note that unidirectionality can be forced by preferentially coupling one direction into the other one [11], but then the round-trip gain of the two directions stays the same, which does not allow for a complete suppression of the other direction.

A basic understanding of travelling wave operation can be obtained by considering the differences between Fabry-Perot and ring lasers. The mirrors of a Fabry-Perot cavity strongly couple inbound and reflected waves, which gives rise to a standing wave pattern with fixed phase at the mirrors. According to the analysis of Sargent, the standing wave induces spatial hole burning, and – through many body effects – this result is multi-mode operation [73].

On the other hand, the ring cavity itself ideally does not have reflection points, the two counter-propagating waves are coupled only indirectly by the common gain medium and by cavity imperfections. Once again according to the analysis

by Sargent, the most likely situation to occur is unidirectional operation, with the conclusion that bidirectional ring laser operation can not occur considering only the many-body effects.

However, with the inclusion of a coupling term between the counter-propagating modes, a large variety of operating regimes appear, as the analysis suggest from Sorel et al. [23]. They investigated the operational regimes by introducing an explicit coupling term  $K$  in the model that directly couples the fields of the two directions, as shown in the time evolution of the fields:

$$\frac{dE_{1,2}}{dt} = \frac{1}{2} (1 + i\alpha) \left[ G_{1,2}(N, E_{1,2}) - \frac{1}{\tau_p} \right] E_{1,2} - K E_{1,2}, \quad (4.4)$$

where  $E_{1,2}$  are the mean field slowly varying complex amplitudes of the electric field of the two directions,  $\alpha$  is the linewidth enhancement factor,  $G$  is the gain factor (depending on the  $N$  carrier density and includes cross-gain saturation effects),  $\tau_p$  is the photon lifetime.  $K$  is the complex backscattering coefficient, which can be written as

$$K = k_d + ik_c, \quad (4.5)$$

where  $k_d$  and  $k_c$  are called dissipative and conservative coupling coefficients, respectively.

The naming of the conservative  $k_c$  and dissipative  $k_d$  can be explained as follows [74]: if we consider CW and CCW traveling waves of the same frequency, a localized step in the refractive index reflects one direction into the other, and therefore it couples the counter-propagating waves. This reflection point only redistributes the energy between the two directions, thus it is called conservative type scattering.

The dissipative coefficient is instead related to localized absorbers, in which the energy is not conserved anymore. If we consider a wave traveling in the CW direction, this can be regarded as the sum of two standing waves  $90^\circ$  out of phase. If one of the two standing waves has a node on a localized absorber, the other has an antinode there. Clearly, the one with the node on the absorber ideally sees zero loss while the other suffers maximum loss. Therefore, the localized absorption tends to move the SRL from a traveling wave situation towards a standing wave situation, which in turn can be regarded as the sum of two counter-propagating waves. Indeed, part of the CW wave gets transferred into the CCW direction. From these simple and intuitive explanations, it appears that both coupling coefficients favour bi-directional operation.

The inclusion of the  $K$  complex coupling term into the model resulted in the appearance of several operational regimes, which agree very well with experimental

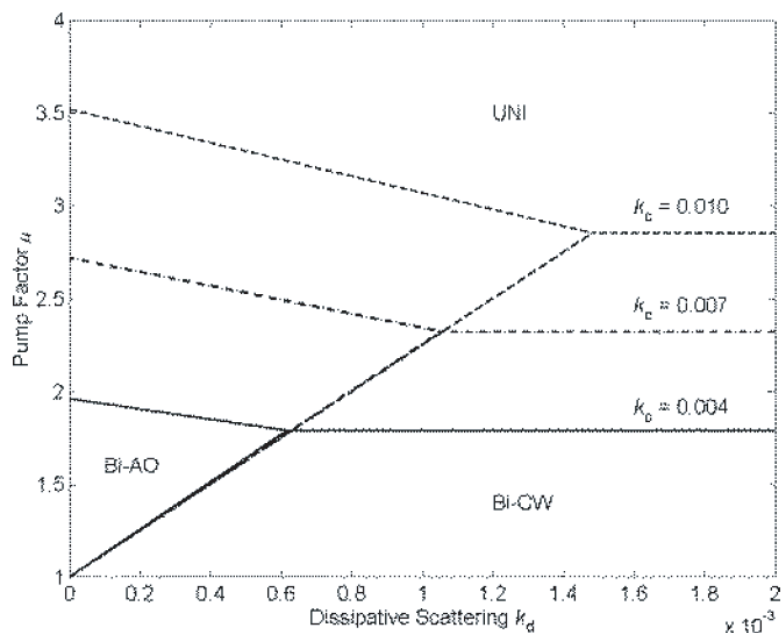


Figure 4.19: Simulated operating regimes of SRLs. The figure is taken from [23].

results. Fig. 4.19 shows that at low values of  $k_d$  and  $k_c$ , unidirectional operation is expected, due to cross-gain saturation. This result is in good agreement with the predictions from Sargent. Otherwise, two more regimes appear at low pump factors, namely bidirectional (Bi-cw) and alternate oscillations (Bi-AO). Bidirectional operation is similar to the normal operation of FP lasers. While alternate oscillations – as the name suggests – is a region where the output power oscillates between the two directions with a frequency in the 100 MHz range.

Mode coupling can occur due to imperfections of the cavity (scattering loss caused by rough sidewall, backscattering by joining straight and curved sections, etc.) and the output coupler. Furthermore, external reflection/absorption points – such as the facets of output waveguides – can give rise to both conservative and dissipative type of coupling. The feedback effect depends on the phase difference between the two waveguides, therefore the coupling coefficients are also wavelength dependent. Moreover, as suggested by Born, coupling can be induced by scattering on the carrier grating – caused by beating of the two counter-propagating fields [75].

From the LI curve, shown previously in Fig. 4.18, a few observations can be made. First of all, the bidirectional regime (indicated as I) has almost disappeared. Furthermore, some more detailed measurements revealed that the alternate oscillation regime is not present.

The curves in Fig. 4.19 suggest that in this device  $k_c$  is small, a situation that provides a very narrow bidirectional region and the absence of alternate oscillations. Compared to previously fabricated devices [23], the devices whose LI curve is reported in Fig. 4.18 have a much stronger coupler and a lower optical feedback from the output waveguides. It appears therefore that  $k_c$  and  $k_d$  are mainly related to the feedback from the waveguides and the strength of the coupler, respectively. This conclusion agrees well with results previously reported in a He-Ne ring laser [74].

### 4.5.2 Modal properties

Let's further examine the operating regimes by considering the spectral distribution as well. Optical spectra were taken from the CW output in steps of 1 mA.<sup>7</sup> The map of the output wavelength is plotted in Fig. 4.20. It can be observed that the unidirectional regime is accompanied by single mode operation. Surprisingly – as the current is increased –, the operating wavelength jumps every four cavity modes. It should be also noted, that this behaviour was only observed for increasing current. When the current is decreased, the direction does not switch and the wavelength jumps over consecutive ring cavity modes.

The SMSR and DER values were also plotted, as shown in Fig. 4.21. As clearly visible, both SMSR and DER increase with current and follow the periodicity of the wavelength jumps. Furthermore, a DER value as high as 34 dB was found, which is the highest reported value for ring lasers.

## 4.6 Conclusions

In this chapter, characterization of stand-alone devices – building elements of the integrated devices – were reviewed. The new wafer and the technology development allowed the fabrication of ring lasers with a minimum radius of 120  $\mu\text{m}$  and the coupling ratio of couplers matches well the designed values. Tuning properties of passive couplers were also presented. The DFBs show low threshold current densities, high SMSR, operating wavelength matching well the design, but the tunability is somewhat limited due to the low value of alpha factor.

The characterization of SRLs show the presence of a quite complicated mode dynamics, with the occurrence of several operating regimes. A phenomenological

---

<sup>7</sup>The measurement was automated using LabView, so that a complete map of the output wavelength could be taken in 10–20 minutes.

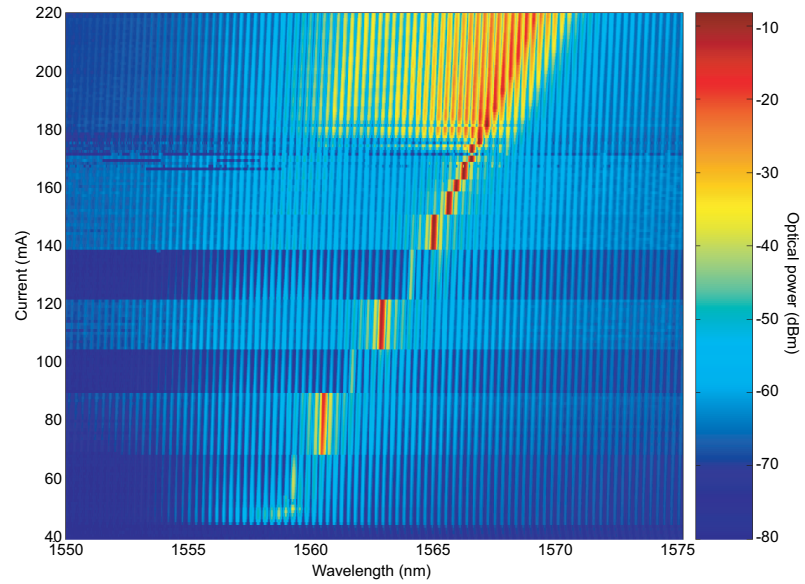


Figure 4.20: Wavelength distribution as a function of wavelength and current.

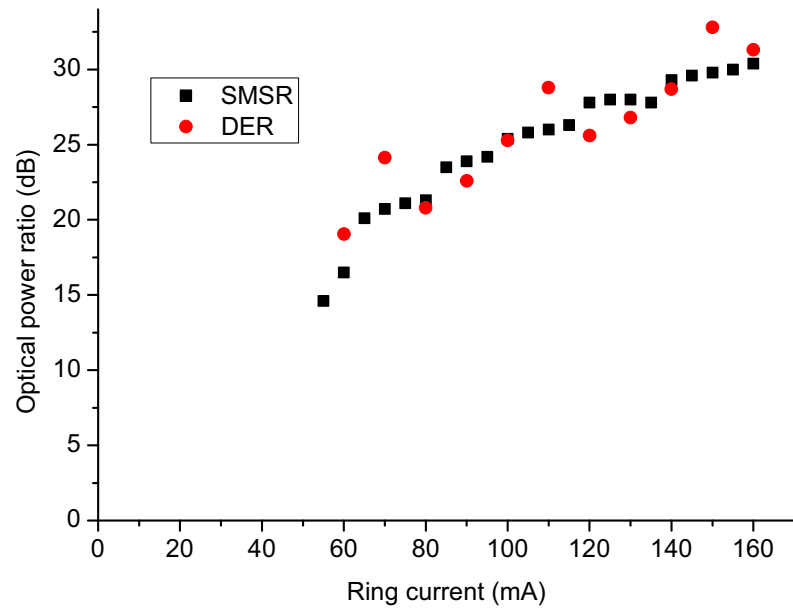


Figure 4.21: directional extinction ratio and side mode suppression ratio as a function of ring current.

explanation can be provided by introducing a complex mode coupling factor in the rate equations, although a complete physical explanation is still missing. By comparing SRLs fabricated in the last 20 years, it can be found that the bi-directional regime was the only mode of operation in the early devices. This is most likely due to the very high value of the conservative scattering originated by the strong feedback from the output waveguides and by coupling mechanisms based on highly-perturbative Y-junctions. In the design of the most recent devices, great care was taken to minimize both the optical feedback and mode reflections at the coupler. This led to devices operating mostly in the unidirectional operating regime.

The presence of the unstable regions at high current values is still being theoretically investigated by a traveling wave model that includes additional non-linear gain mode coupling mechanisms. The unexpected mode jumps for increasing current values will be investigated in detail in the following chapter.

# Chapter 5

## Feedback in SRLs

This chapter deals with the peculiar mode selection rules seen in SRLs, as well as the effect of feedback on the operating conditions. As suggested earlier, due to non-linear gain competition, the most likely operation of SRLs is unidirectional. However, any type of coupling between the two counter-propagating directions perturbs this scenario and gives rise to other modes of operation. Throughout this research, the main coupling mechanism and the origin of mode-jumps were identified to be caused by the weak optical feedback from the output waveguides to the ring, which will be presented in this chapter. For the sake of coherence, the results are presented in a bottom-up manner instead of following the time-line of findings.

The chapter begins with very high resolution passive measurements of rings coupled to an output waveguide that shows a frequency-splitting of the cavity modes of the ring. This analysis is followed by above threshold cavity line measurements, revealing and explaining the atypical mode-selection seen in SRLs. Then the effect of stronger feedback is presented, together with the multi-wavelength stability.

### 5.1 Transfer function of SRLs

#### 5.1.1 Measuring the transfer function

A measurement was carried out below threshold to get information on the fine mode structure of the cavity resonances of SRLs. The simplest structure – an SRL with a ring radius of  $300\ \mu\text{m}$  and a point coupler – was measured using the setup shown in Fig. 5.1. The measurement technique allows a high resolution ( $0.5\ \text{pm}$ ) mapping of the cavity lines. From a tunable laser, a monochromatic field was injected through

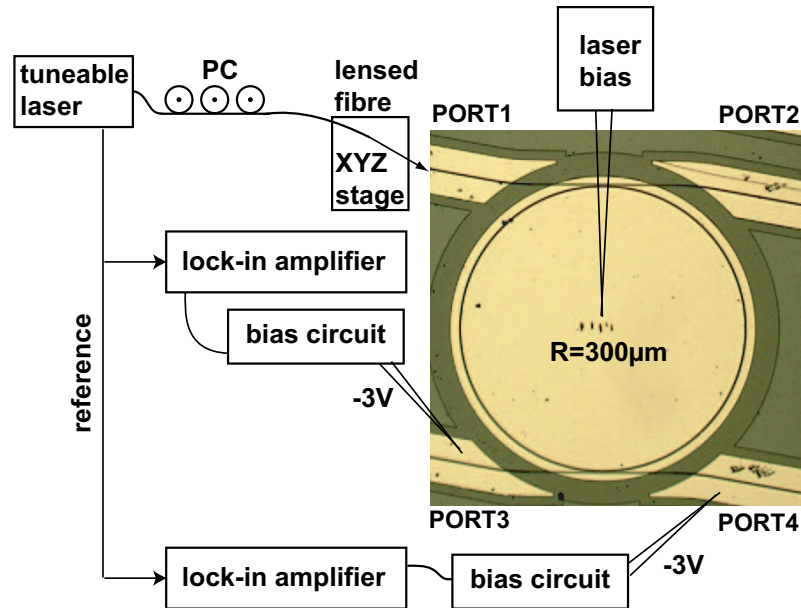


Figure 5.1: Optical micrograph of a  $300\ \mu\text{m}$ -radius ring laser with the corresponding measurement setup.

port #1 of the device. The photo-currents generated in ports #3 and #4 were measured by using a lock-in amplifier that is locked to the internally modulated signal of the tunable laser. These two ports were reverse biased to maximize the detected signal and to absorb any unwanted backreflection coming from the facets of the bottom waveguides. Feedback levels from unbiased and biased outputs were estimated to be  $-79.2\ \text{dB}$  and  $-94.6\ \text{dB}$ , respectively. During these measurements, the ring was biased close to transparency to minimize the absorption losses.

Fig. 5.2 shows the power collected at ports #3 and #4 as the input wavelength is scanned. It can be seen that the power in port #3 displays narrow and well defined peaks at wavelengths equispaced by  $0.4\ \text{nm}$ , corresponding to the FSR of the ring. The peak heights show the expected profile defined by the wavelength-dependent transmission spectrum in the structure but also an additional modulation that occurs every three longitudinal modes. Furthermore, a zoom around these peaks (in Fig. 5.3) reveals that they possess a doublet structure, with the splitting between the two subpeaks being of the order of  $2\text{--}4\ \text{GHz}$ . The power collected at port #4 presents a similar structure with the same periodicity, but instead of displaying peaks above a spontaneous-emission noise background, it shows dips on such a background.

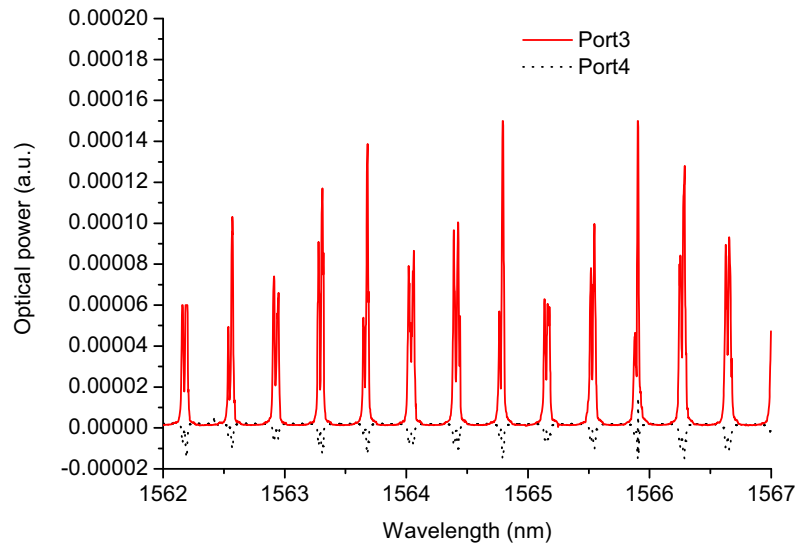


Figure 5.2: Detected power at port #3 and #4.

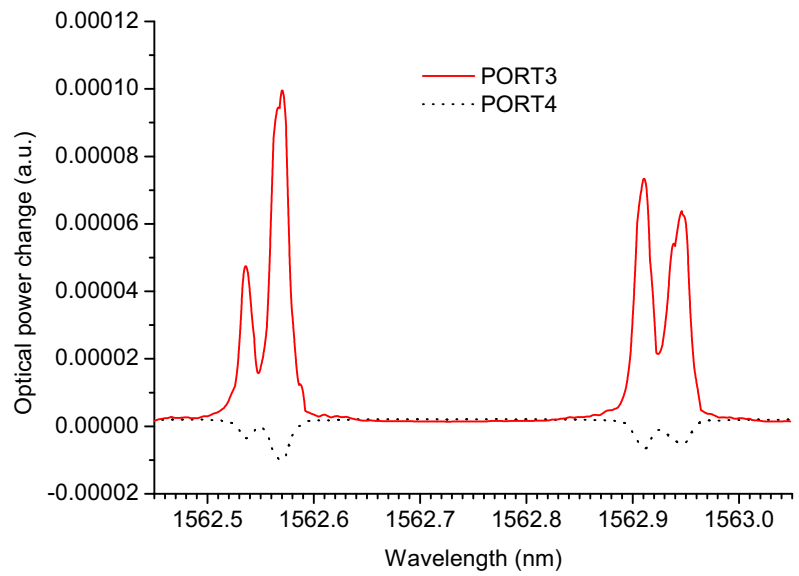


Figure 5.3: Zoom in of the measured lines.

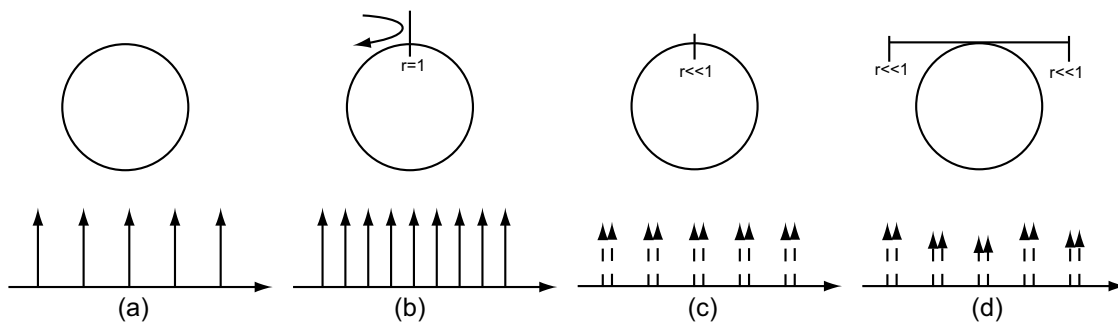


Figure 5.4: Transfer function in the frequency domain of (a) unperturbed ring, (b) ring with a strong point reflection, (c) ring with a weak point reflection and (d) ring coupled to a weak Fabry-Perot filter.

### 5.1.2 Measurement analysis

A detailed theoretical analysis was carried out on the transfer function of the SRL, and the above presented measurements with the corresponding simulation results (carried out by our collaborating partners) were published in [76]. The model theoretically expresses the transfer function by considering the perturbation induced by the output couplers, which induces a symmetry breaking in the resonant cavity and a modulation of the cavity losses.

A basic understanding on the existence of doublets can be obtained with the illustrative example shown in Fig. 5.4. An unperturbed ring gives narrow, well-defined peaks (Fig. 5.4a) spaced by the FSR of the ring given as

$$\Delta\nu = \frac{c}{nL_{\text{cav}}}, \quad (5.1)$$

where  $\Delta\nu$  is the mode spacing,  $c$  is the speed of light,  $n$  is the group index and  $L_{\text{cav}}$  is the length of the cavity.

If we insert a strong point reflection (with a reflectivity  $r = 1$ ) into the cavity (Fig. 5.4b), the device becomes a perfect FP etalon with a length of  $L_{\text{cav}}$ . The FSR in this case gets halved:

$$\Delta\nu = \frac{c}{2nL_{\text{cav}}}. \quad (5.2)$$

In other words, the two directions of the ring gets coupled into one direction of a large ring with a cavity length of  $2L_{\text{cav}}$ . When the reflection is weak (Fig. 5.4c), the lines of the original cavity are split – a result that is an intermediate transition between the first two cases.

A more realistic situation is obtained by considering the ring coupled to a weak FP etalon defined by the output waveguides. On top of the mode splitting, this

scenario introduces a weak intensity modulation of the transmission peaks, with a periodicity depending on the ratio of the FSR of the ring, the length of the output waveguide and the transmission properties of the output facets and the coupler. The resulting transfer function is illustrated in Fig. 5.4d.

The frequency splitting of the doublets comes from dissipative coupling introduced by the output-coupling. Also, the filtering effect of the FP etalon also causes a periodic intensity modulation.

The roundtrip condition for the SRL modes in a resonator with one output arm with a length of  $L_{cav}/2$  can be formulated as

$$e^{2iqL_{cav}} - ae^{iqL_{cav}} + b = 0, \quad (5.3)$$

where  $L_{cav}$  is the length of the cavity,  $q$  is the propagation constant and

$$a = \frac{t + t'}{tt' - rr'} \quad (5.4)$$

and

$$b = \frac{1}{tt' - rr'}. \quad (5.5)$$

Eqs. 5.4 and 5.5 contains the couplers wavelength-dependent transmissivity ( $t$ ) and reflectivity ( $r$ ) in the CW direction while the primed symbols denote the same magnitudes for the CCW waves. The solution for the SRL modes yields

$$q_m^\pm L_{cav} = 2\pi m - i \ln \left[ \frac{a}{2} \pm \sqrt{\left(\frac{a}{2}\right)^2 - b} \right] \equiv 2\pi m - i \ln Q_\pm, \quad (5.6)$$

having two branches of solutions for the two directions.

The doublet frequency-separation also gets modulated following the periodicity of the amplitude modulation because of the reflections coming from the output facets. The frequency separation has local maximum and minimum at the wavelengths where the combined cavity has minimum and maximum transmission, respectively. According to the perturbative analysis, the doublet separation frequency can be analytically expressed. When normalized to the FSR it yields:

$$\Delta = \frac{1}{2\pi} \left\{ \text{Im} \left[ \ln \left( \frac{Q_-}{Q_+} \right) \right] - \alpha \text{Re} \left[ \ln \left( \frac{Q_-}{Q_+} \right) \right] \right\}, \quad (5.7)$$

where  $\alpha$  is the linewidth enhancement factor.

Of course, the actual shape of the individual lines depends on the available gain, the cavity losses, the strength of the coupler, the reflection coming from the output

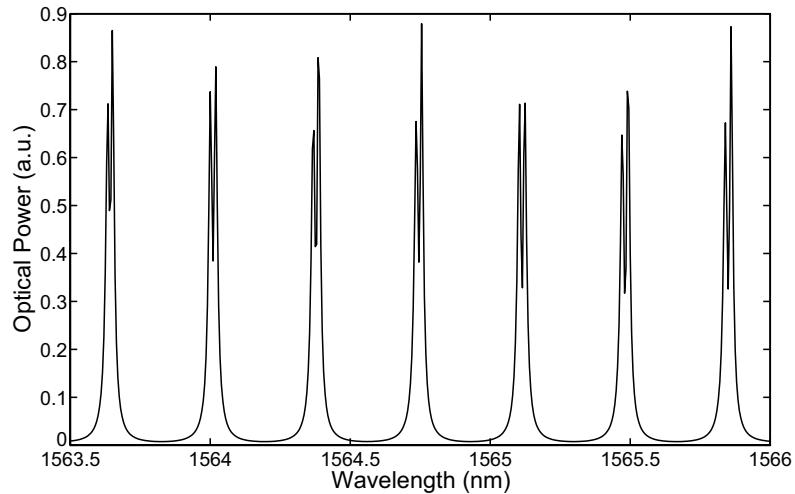


Figure 5.5: Theoretical results for the power collected at port # 3.

facets and the wavelength as well. Including these effects, the cold-cavity analyzes reproduces well the measured lines (Fig. 5.2), such as indicated in Fig. 5.5. In these calculations, the section lengths have been taken from the device layout and facet reflectivities have been adjusted to match the experimental results.

### 5.1.3 Asymmetric four port device

A logical extension of the model is to include a second output coupler. A device with perfect symmetry produces the same results as discussed earlier, however, any type of asymmetry – for example a difference in the output waveguide length – further splits the cavity modes. This effect was demonstrated by measuring a four port device (with a symmetric structure) but having one output waveguide broken. The measured cavity line (Fig. 5.6) indeed shows the further splitting of the doublets into a quadruplet structure.

Plotting the separation frequency between the doublet pairs (Fig. 5.7) also shows the expected trend: a constant separation gets further modulated by the coupled cavity effect. The cold cavity analyzes reproduces well the measured doublet separation distance, as shown in Fig. 5.8

It is worth to note that the broken output gave only about 5 dB lower output power than the others when the laser was measured above threshold. This indicates that even very small imperfections can split (further) the cavity modes.

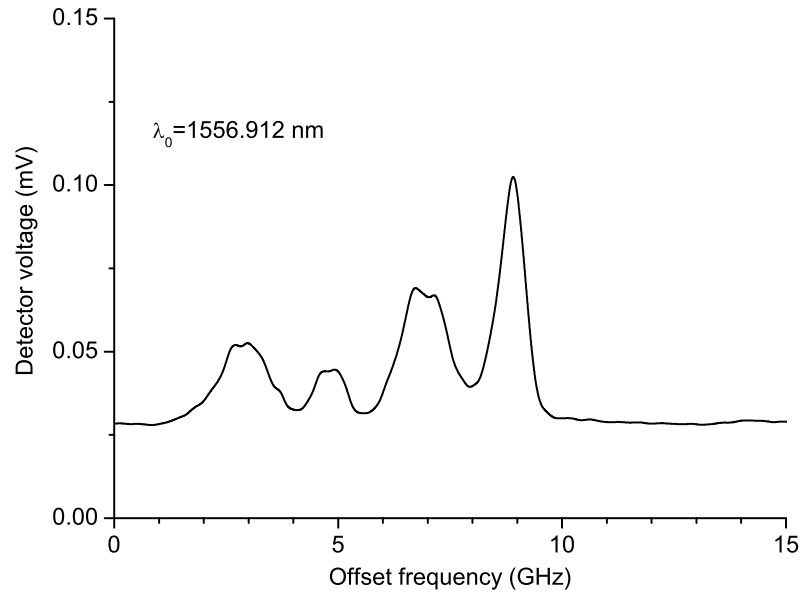


Figure 5.6: Transmission measurement of a cavity line of an asymmetric four port device.

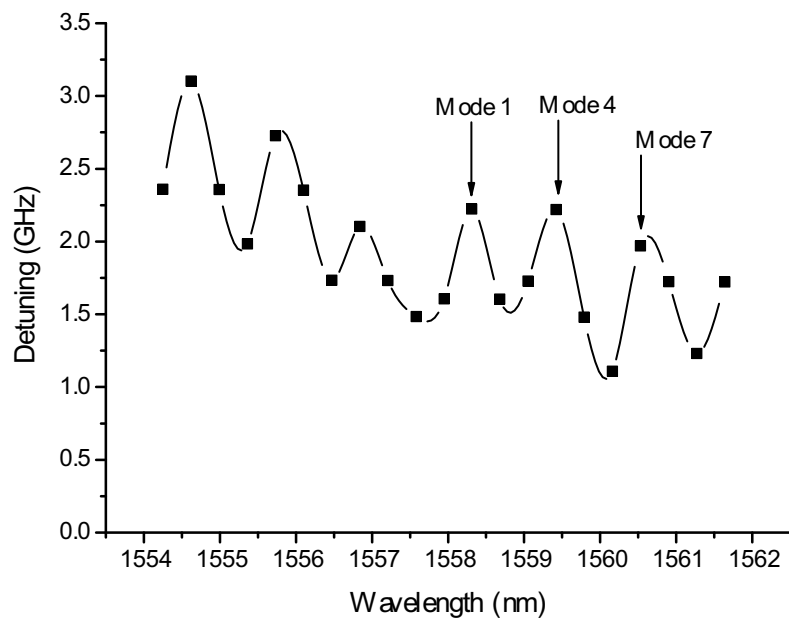


Figure 5.7: Doublet separation as a function of the wavelength.

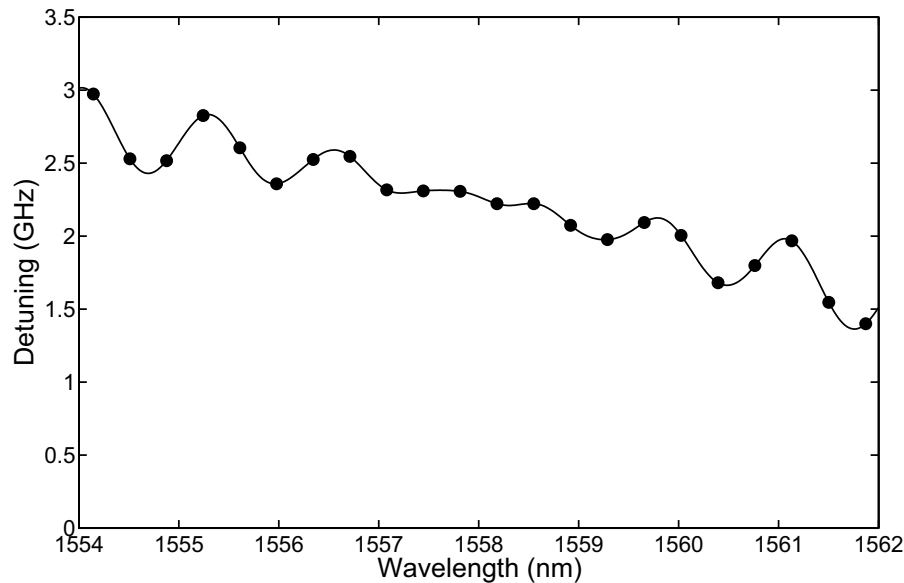


Figure 5.8: Theoretical detuning between doublets.

#### 5.1.4 Effect of amplified spontaneous emission noise

In an ideal situation no signal should emerge from port #4, however, a power drop in the signal is measured when peaks appear in port #3 (see Fig. 5.2 and 5.3). The power collected at ports #3 and #4 in the absence of external light is the power due to spontaneous emission in the SRL. In the absence of any reflecting element, light injected into the SRL through port #1 would reach port #3 only after being amplified or attenuated along the path, and no injected light would reach port #4; however, the power at port #4 is reduced because of amplified spontaneous emission (ASE) suppression under light injection, thus leading to dips onto the ASE background.

The explanation is confirmed by measuring the envelope of the signal detected at both ports for different bias currents. To do so, the measurement was slightly modified: instead of using small steps, the tunable laser was set to scan continuously across the cavity modes. At the same time, the integration time of the lock-in amplifier was set onto a longer time-scale, so the cavity modes were averaged out and only the envelope signal was measured. The advantage of this method is that it allows for very fast data collection. Using this method, a wavelength range of 10 nm can be scanned in 1–2 minutes, while depending on the resolution the high resolution step-scan measurement can take 1–2 hours.

Fig. 5.9 shows the measured signal that was collected from port #4. Indeed,

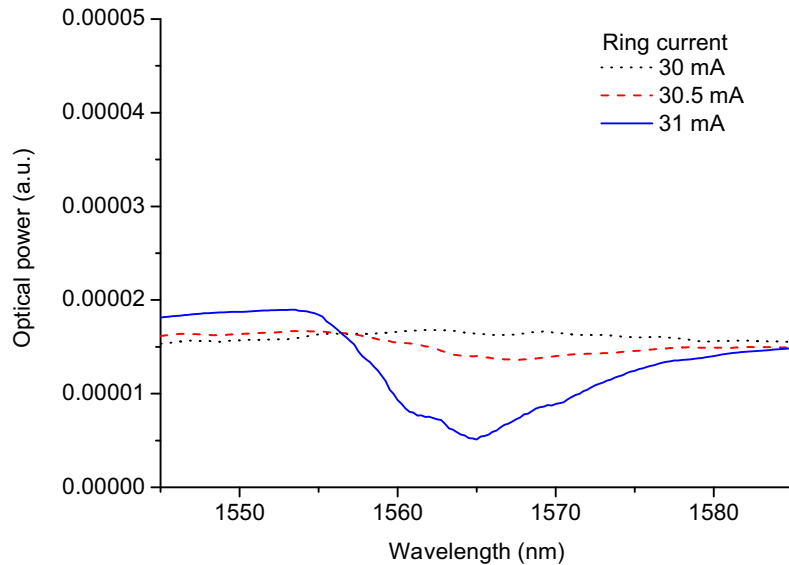


Figure 5.9: Measured envelope signal at port #4 for different bias currents.

the dips cannot be seen for bias currents below 30.5 mA and become clearly visible above that value. It is worth remarking that this measurement technique provides us with a precise way to measure the spectral dependence of the transparency current, i.e. the current that provides a complete flat output at port #4 corresponds to the transparency current value at that wavelength. On the other hand, the measurement from port #3 (Fig. 5.10) provides the shape of the gain curve independently from the current bias of the SRL.

## 5.2 Mode selection in SRLs

The previous section presented the evolution of the doublets in the cold cavity case. It was experimentally demonstrated that a ring coupled to an output waveguide does not possess the expected mode profiles, but the original lines of the ring cavity split. Furthermore, both the intensity transmitted and the doublet separation undergo an extra modulation. This section analyzes the SRL modal characteristics above threshold and demonstrates that the mode selection rules are dictated by the cold cavity transfer function of the device.

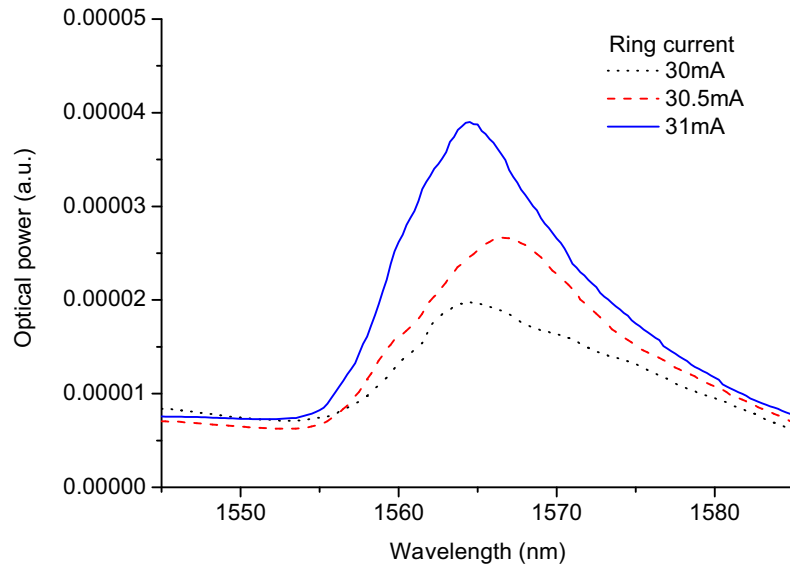


Figure 5.10: Measured envelope signal at port #3 for different bias currents.

### 5.2.1 Modal thresholds

Fig. 5.11 reports the L-I curve of the  $300\ \mu\text{m}$  radius device, showing the typical<sup>1</sup> SRL switching behavior between the CW and CCW directions for increasing current, along with the wavelength of the main lasing direction. It clearly appears that, in the regime of directional switching, the dominant lasing wavelength remains locked (except for a small thermal drift) when the lasing direction does not hop, but it suddenly jumps by three cavity modes when the lasing direction reverses.

The output coupler breaks the circular symmetry of the ring [77], which implies that pure CW and CCW states do not exist anymore due to the defect. As shown in Eqn. 5.6, the threshold condition of the modes possesses two solution branches, and become different for the two directions. An illustrative figure on the resulting modal thresholds can be found in Fig. 5.12. The SRL lases at the minimum of energy (one direction and wavelength) and the threshold modulation for each of the two branches of solutions is out of phase. Hence, when the gain spectrum redshifts due to Joule heating, the system will jump from the minimum on one branch to the following minimum on the other branch. For the considered reflectivity values and where  $L \geq 2R$ , this means a jump of  $m = \text{int}[3\tau_R/\tau_{FP}]$  modes of the SRL, where  $L$  is the length of the output waveguide,  $R$  is the radius of the circular cavity,  $\tau_{R(FP)}$  is the roundtrip time in the SRL (Fabry-Perot) cavity. Thus, for the

<sup>1</sup>As shown for example for an other device earlier in Fig. 4.20 or reported in [23].

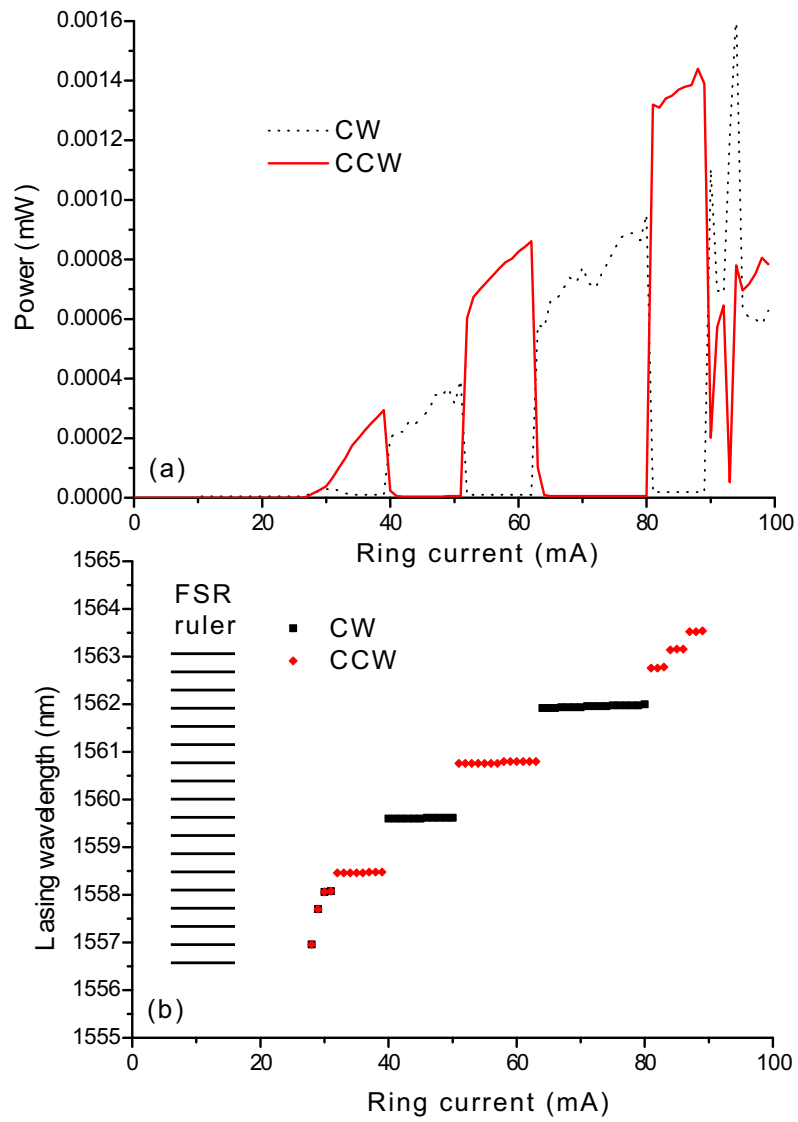


Figure 5.11: LI curve (top) and lasing wavelength (bottom).

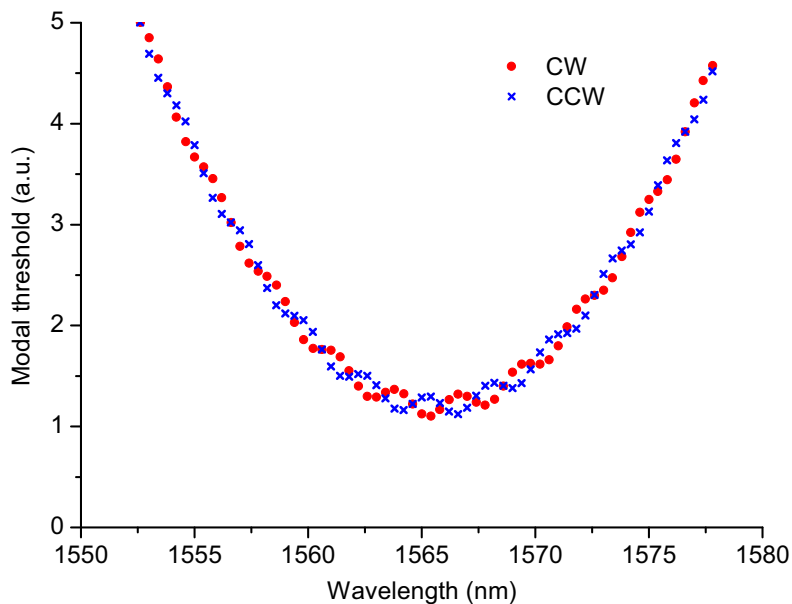


Figure 5.12: Illustrative figure on the two solution branches imposed by cavity defects. The minimum modal threshold corresponds to a maximum doublet separation.

device considered here, the modal jumps correspond to  $m = 3$ , which equals to the experimental observation.

### 5.2.2 Doublets in the bidirectional regime

The effect of the mode splitting due to the output waveguides has also an influence on the modal behavior of the SRL operating on the bidirectional regime. In order to have sufficient output power to directly observe the lasing modes, the 300  $\mu\text{m}$ -coupler device was investigated. The ring was biased above threshold with a current of around 64 mA, which corresponds to the bidirectional regime. In this case, the mode-competition is not strong enough yet to provide pure unidirectional operation. An individual mode of the SRL and the output power from a tunable laser were beaten on a high-speed photodetector and the resulting signal was visualized in the frequency domain by an RF spectrum analyzer. The technique is called heterodyne measurement and it is based on the fact that the beating signal has a directly measurable electrical component at frequency of  $\omega_2 - \omega_1$ , where  $\omega_2$  and  $\omega_1$  are the frequencies of the SRL and the tunable laser, respectively. Since the tunable laser has a very narrow linewidth (less than 10 kHz), this technique

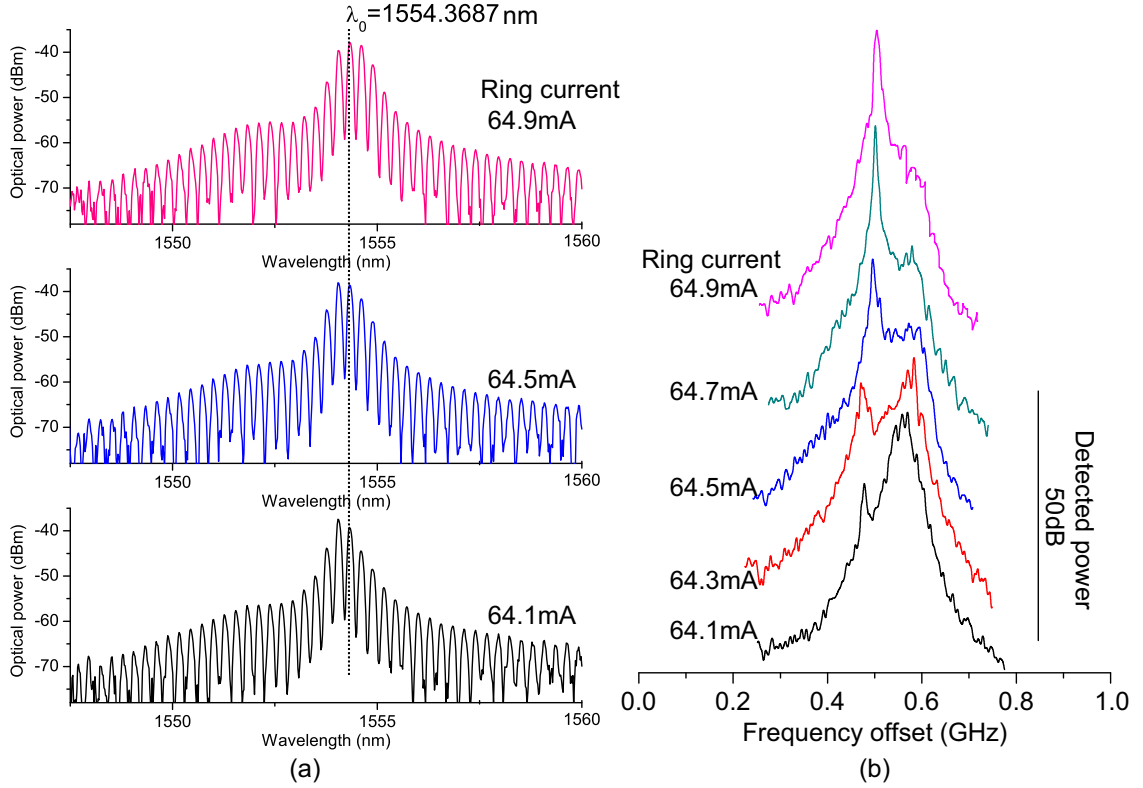


Figure 5.13: Doublet evolution in the bidirectional regime: (a) optical spectra of the CW direction for different ring currents and (b) heterodyne measurement of the indicated mode at the same current range.

enables a very high-resolution measurement of the optical spectrum of the SRL.

The optical spectra and the beating signal for different currents were plotted in Fig. 5.13. It can be seen that at a current of 64.1 mA, the observed mode has lower power than the adjacent cavity mode, and it possesses a doublet structure. When the current is increased, the power gradually shifts from an equal power distribution between the split lines of the cavity to the one. At the same time the mode becomes the lasing mode with the maximum output power. Further increasing the current shifts the gain peak to higher wavelengths and the doublet structure becomes visible again. The observation parallels with previous conclusions: when one of the split cavity line has minimum of modal threshold (highest modal power), the other one has maximum modal threshold – i.e. it does lase. When the lines of the doublet possess equal power, lasing occurs at the energy maximum of the system, which leads to the minimal modal power.

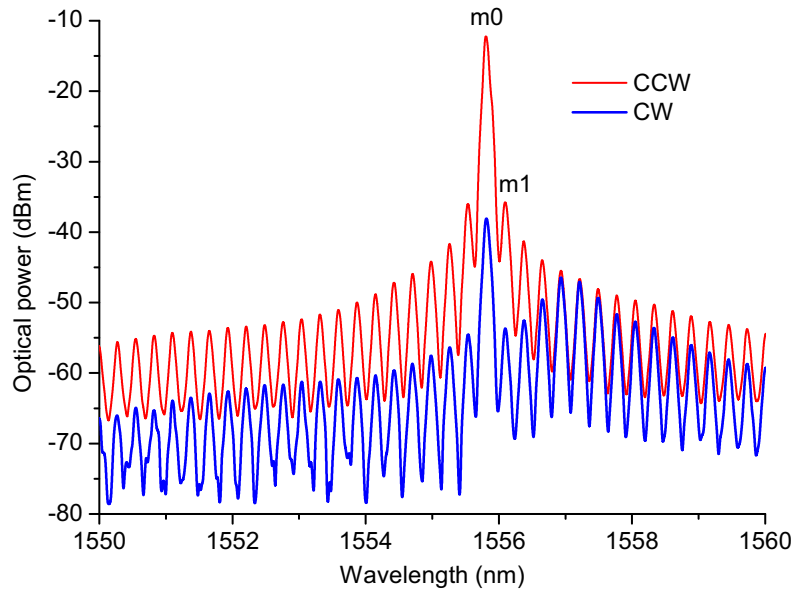


Figure 5.14: Optical spectra of a 300  $\mu\text{m}$ -radius SRL at a current of 115 mA for the two directions.

### 5.2.3 Doublet evolution versus mode number

The previously presented technique was used for measuring the individual laser lines in the bidirectional regime. A similar measurement was performed for a laser current of 115 mA, which corresponds to unidirectional operation. For this current value, the CCW direction is favoured with an SMSR of 28 dB, as plotted in Fig. 5.14. The suppressed mode (CW direction) has its maximum at the same wavelength as the main lasing mode (m0) but a further group of stronger modes appears 3–4 cavity modes away.

The heterodyne measurement of the individual cavity modes of the lasing direction at a fixed current value was plotted in Fig. 5.15. It can be observed again that the main lasing mode – being the only one to reach the modal threshold – does not show a doublet structure. Moving towards the adjacent cavity modes, the doublets are more evolved with more equal modal power. This observation parallels again with the analysis: the system lases at the energy minimum, where one doublet line has minimum and the other has maximum threshold. It must be also emphasized that pure CW and CCW states do not exist: both of the lines of the cavity mode are bidirectional when they possess about the same power. Quasi-unidirectional operation occurs, when one line of the doublet has minimum threshold and, at the same time, the other direction suffers from maximum threshold. When the effect is

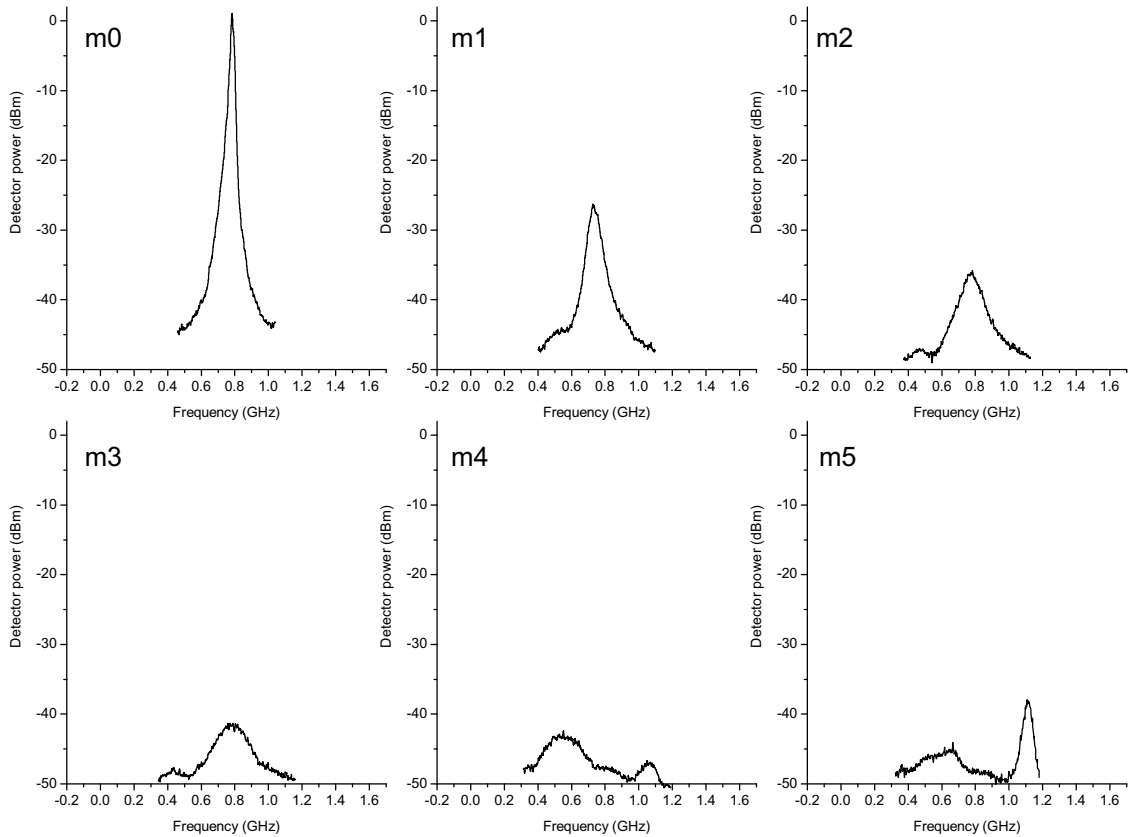


Figure 5.15: Heterodyne measurement of the modes of the lasing direction. The mode numbers are the same as in Fig. 5.14. The DC level and the noise floor are not shown.

enhanced and stabilized by cross-gain saturation, unidirectional operation occurs.

#### 5.2.4 Coupled cavity effect in large SRLs

The analysis would not be complete without providing an example on wavelength jumps other than three modes. Throughout this work, a number of different device geometries were fabricated, and – due to geometrical considerations to maximize the number of devices per chip – the ratio of the SRL cavity and output waveguide was always around two.<sup>2</sup> Therefore, the wavelength jump in these devices were in the range of 3–4. Having mode-locking applications in mind, SRLs with FSR of 18 GHz and 9 GHz were fabricated, corresponding to 5.2 mm and 10.4 mm cavity

<sup>2</sup>To save chip space, the length of the output waveguides was always kept around 1 mm.

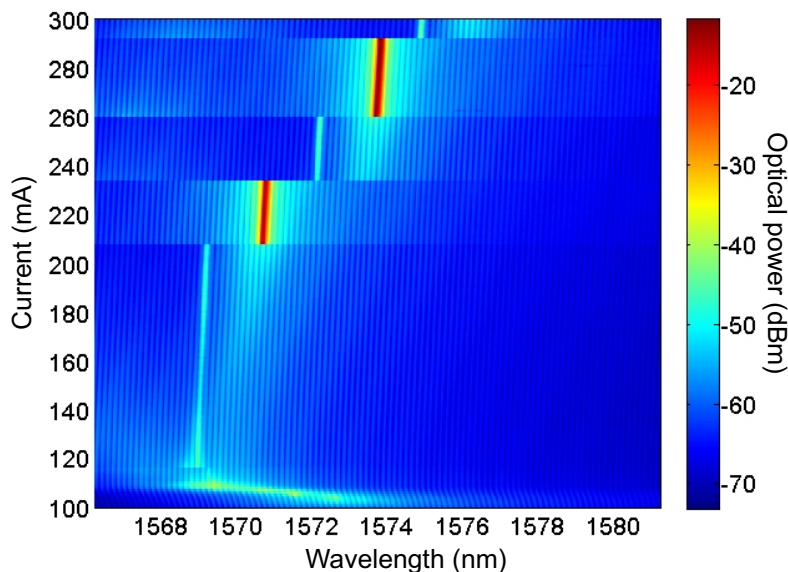


Figure 5.16: Wavelength map of a 5.2 mm cavity length SRL. The lasing wavelength jumps to every nine cavity modes.

lengths, respectively. The long cavity was folded into about  $4 \text{ mm}^2$  ( $7 \text{ mm}^2$ ) area to save chip space, while the width of the chip was kept at the usual 1 mm.

The wavelength map of the device can be seen in Fig. 5.16. It can be seen that the device jumps every 9–10 cavity modes. Even though the actual geometry was not fitted, a final confirmation of the effect comes from plotting the presented wavelength jumps for different geometries. Fig. 5.17 shows that there is a strong correlation between the output waveguide length and the presented jumps in wavelengths, despite the fact that the data set includes a large number of cavity lengths (0.75–5.2 mm) and coupler lengths (0–300  $\mu\text{m}$ ).

It can be finally concluded that the periodic switching observed during unidirectional operation of SRLs is caused by the extra cavities formed by the coupler and output waveguides. It must be noted that this behavior occurs with optical feedback levels as low as  $-60$ – $-70$  dB and it is therefore an unavoidable characteristic of SRLs, even if the waveguides are optimized for minimum feedback.

### 5.3 Feedback effect on operational regimes

In the previous section it was shown, that the feedback coming from the output waveguide affects the mode-selection in the unidirectional operation. Larger val-

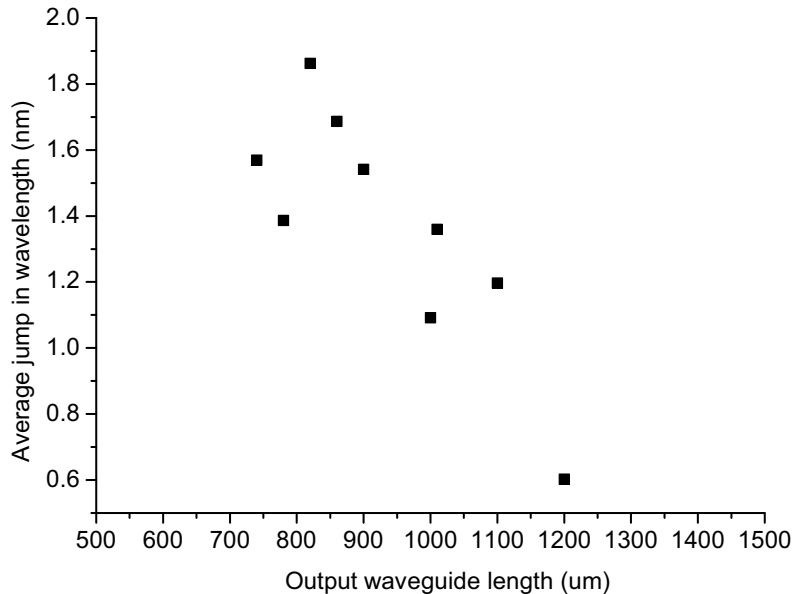


Figure 5.17: Average jump in wavelength for different SRLs.

ues of feedback, however, can not only shift the boundaries between the various operational regimes but can also induce a large variety of high-frequency mode dynamics.

The SRL used for strong feedback measurements has a  $300\ \mu\text{m}$  ring radius with a coupler length of  $300\ \mu\text{m}$ , as presented earlier in Fig. 4.17. The full spectral behavior and LI curves of the two directions was also reported in Fig. 4.20 and Fig. 4.18, respectively. The reason for selecting this device is because of its simple structure (single output waveguide), relatively high output power (30% coupler) and high injection values are available due to the large cavity. Furthermore, a frequency that can be measured with the available setup in the Department, since the PD and RF spectrum analyzer have a maximum frequency of  $f_{\text{max}} = 45\ \text{GHz}$ .

It was also presented earlier (Fig. 4.21) that both the DER and SMSR values are in the range of 15–35 dB for increasing values of the injected current. One of the most important properties of SRLs is unidirectionality, therefore the DER values were measured against increasing values of feedback. The additional contact pads on the output waveguides can be reverse or forward biased to increase or decrease the losses of the output waveguides, respectively. For small values of current or reversed voltage, the gain/loss can be assumed to vary linearly<sup>3</sup>. The exact values

<sup>3</sup>In fact it is exponential dependence, linear on the dB scale.

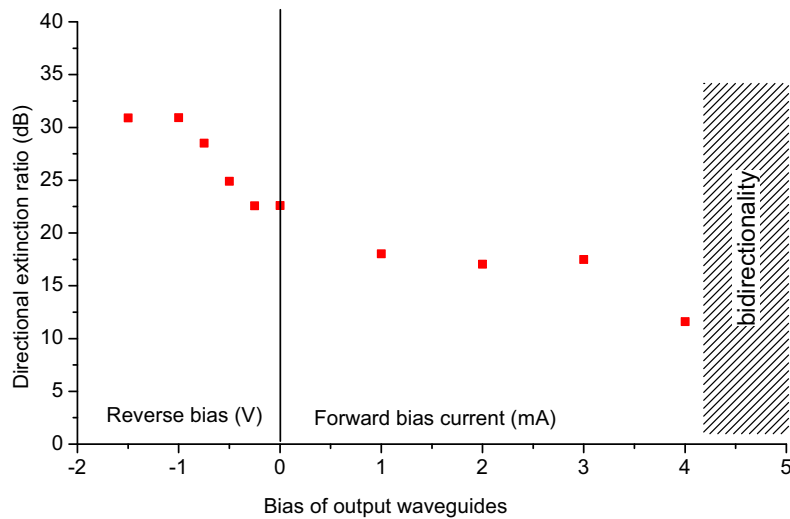


Figure 5.18: Directional extinction ratio versus symmetric feedback.

of attenuation and amplifications are calculated from the three-section waveguide measurements, reported earlier in Fig. 4.3. It was estimated that the nominal feedback from the output facets can be changed by  $+3$  dB/mA or  $-17$  dB/V by applying current or voltage, respectively.

At a ring current of 90 mA the DER is plotted in Fig. 5.18. It can be observed that – with increasing feedback level – the DER gradually decreases and finally, above currents of 4 mA, unidirectional operation ceases. It again confirms the results that feedback from the output facets (i.e. coupling of the two directions) have a major effect on SRL behavior. The LI curve – when 10.5 mA is pumped into the waveguides – reported in Fig. 5.19 confirms that unidirectional operation is strongly suppressed. Although, the LI curve shows some periodic preferential selection of direction, the difference in the output power does not exceed a few dBs and the laser exhibits multi-mode operation.

As a function of increasing feedback level, a map of the operational regimes was recorded and plotted in Fig. 5.20. As expected, the boundary of the unidirectional regime – called earlier Region I – gradually shifts to higher currents when the feedback from the output waveguides increases. Additionally, the alternate oscillations (Region II) still does not appear, which might be due to the low or high value of the conservative or dissipative scattering, respectively. Moreover, it can be observed, that Region IV and V do not shift as a function of the feedback. Therefore, it can be concluded that the existence of these regions is an inherent property of ring lasers and independent of the output waveguide geometry. These

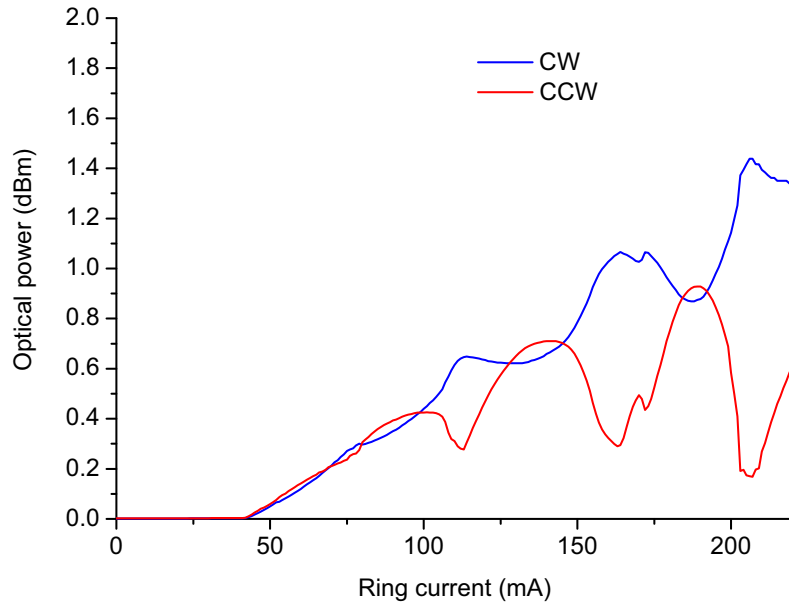


Figure 5.19: LI curve when a current of 10.5 mA is injected into both of the output waveguides.

two regions might be related to the power density inside the cavity that enhances non-linear gain effects: the effect was observed only at low-coupling and high pump rates ( $4-5 I_{th}$ ).

It was observed, that Region IV is a transition between uni- and bidirectional operation. This region is highly unstable and the output spectra and mode-power constantly change. Therefore high-frequency measurements were taken to gather a better understanding on the dynamical behaviour, as reported in Fig. 5.21.

The laser shows a large frequency spectrum, most likely chaotic, with a maximum frequency around 80 MHz. Therefore one can conclude that the characteristic life-time of a state is around 10 ns. The ever-changing output makes difficult the measurement of switching times between states, because sampling is not a viable option. Even so, it was measured with a real-time oscilloscope to be faster than  $2 \text{ ns}^4$ . The further investigation of Region IV is out of the scope of this thesis, however it will be suggested as *future work* in the Conclusions chapter, since this dynamically active region could be of interest for generating optical chaos.

It must be noted that a similar (but only a couple of tenth of mA narrow) boundary can be found between Region I and III. As stated earlier, alternate oscil-

<sup>4</sup>The oscilloscope had an  $f_{max} = 500 \text{ MHz}$ , which limited the measurement.

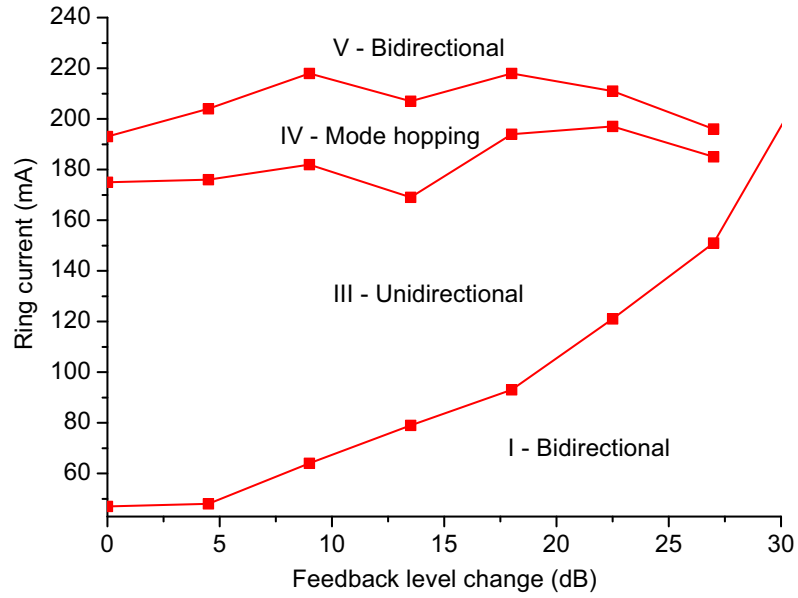


Figure 5.20: Operational regimes as a function of ring current and change in feedback level. The base-line corresponds to the threshold current of 43 mA.

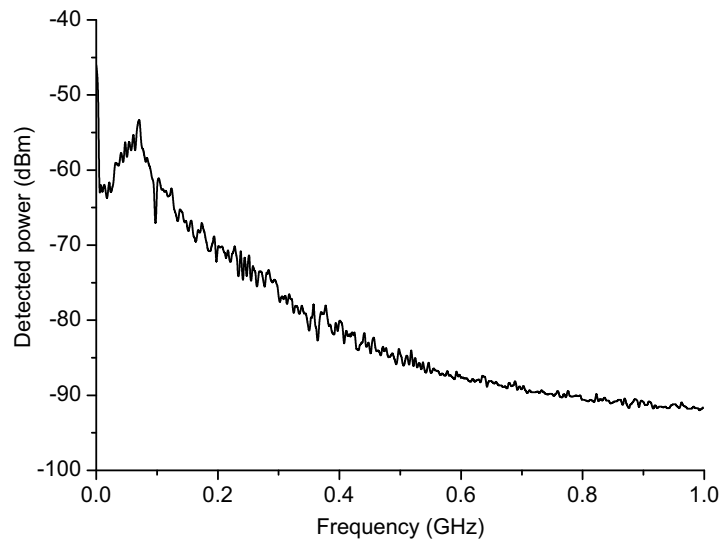


Figure 5.21: RF spectra measured in Region 4.

lations (called Region II) do not show, but the boundary of Region I and Region III is not well defined, most likely the laser here quickly moves between the two regions due to thermal noise.

## 5.4 Mode locking induced by feedback

In Region V – without increasing the level of feedback – the RF spectra of the outputs do not show any dynamics<sup>5</sup> and the optical spectra show stable, multi-mode, bidirectional outputs. For large feedback levels, a number of patterns appear on the RF spectra.

Most notably, a narrow-band signal appears exactly at the FSR frequency, as shown in Fig. 5.22. The existence of this signal indicates a high phase-correlation between the individual cavity modes of the SRL (which are now standing waves) with the emerging of pulses in the time domain. Due to lack of equipment, the time-domain pulse shape was never measured, so a detailed investigation on the mode-locking operation could not be performed. However, a number of observations support the assumption that the laser operates in a feedback induced stable passive mode-locking regime. First of all, the whole system is similar to the one described in [78] where passive mode-locking was achieved by using a vertical-cavity surface-emitting laser (VCSEL). In which, the output signal was reinjected after a delay line and polarization rotation. The re-injection of the other polarization resulted in a modulation of the carriers, which provided the non-linearity to achieve mode-locking. Here, the delay is provided by the output arm, and the cleaved facet couples the two counter-propagating modes. The two directions are sharing the same gain medium, similarly to what happens in the TE/TM configuration in a VCSEL. Secondly, the RF spectra shows a well defined peak with very low jitter, which is a clear signature of mode-locking operation. Thirdly, self-pulsations can be observed at the boundaries of the stable mode-locking regions, which is a typical feature of mode-locked lasers. It is worth to note, that this effect is also similar to the so called additive pulse mode-locking (APML) or coupled-cavity mode-locking (CCML) [79], however, no detailed analysis was carried out to further support this assumption.

The shape of the optical spectra shows the presence of two peaks, whose wavelength gap is given by the loss/gain modulation of the output waveguide. In the measurements, two distinct behaviors were observed: one with a narrow RF signal

---

<sup>5</sup>Up to the detectable frequencies of 45 GHz.

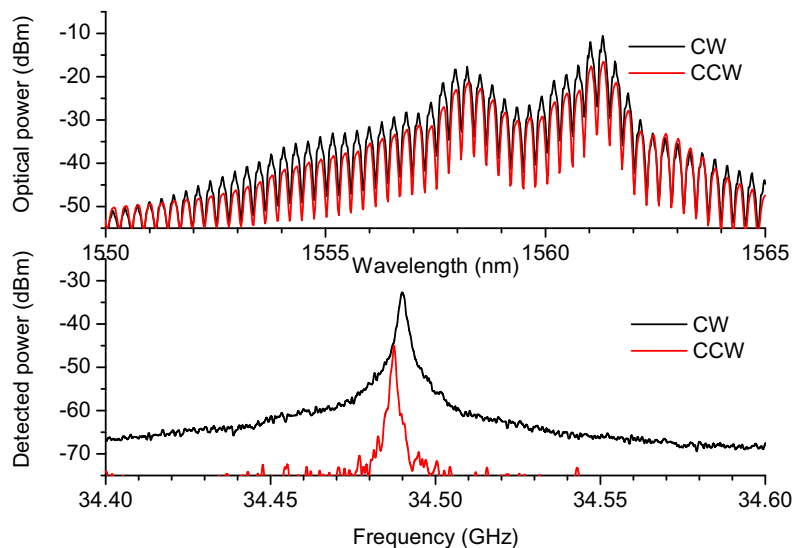


Figure 5.22: RF and optical spectra of the two directions at a current of 10 mA, 152 mA and 12.5 mA, injected into the CW output, the ring and the CCW output, respectively.

(as shown in Fig. 5.22) and one with a signal occupying about a ten times wider bandwidth. The map of these two mode-locking regimes was plotted in Fig. 5.23 as a function of the currents of the output arms. From the plot a narrow linewidth mode-locking region appears for low values of the optical feedback, while the wide linewidth mode-locking occurs at higher feedback levels. Also, the mode-locking regions seem to depend on the total amount of feedback ,i.e. the mode-locked regions overlap with the total constant feedback level from both waveguides.

Between the two mode-locking regions (mainly at the boundaries), a number of other dynamical scenarios were found. One typical example is the mixture of Region IV and Region V. As shown in Fig. 5.24, the RF spectra around the FSR frequency contains two side peaks at  $f_2 + f_1$  and  $f_2 - f_1$ , where  $f_2$  is the FSR frequency and  $f_1$  is the peak observed in the mode-hopping region. Finally, in this dynamically active region, three other examples of RF spectra are shown in Fig. 5.25.

## 5.5 Multi-wavelength stability

The most novel feature of SRLs is the unidirectional operating regime in which either of the two counter-propagating modes can lase. It was shown that for in-

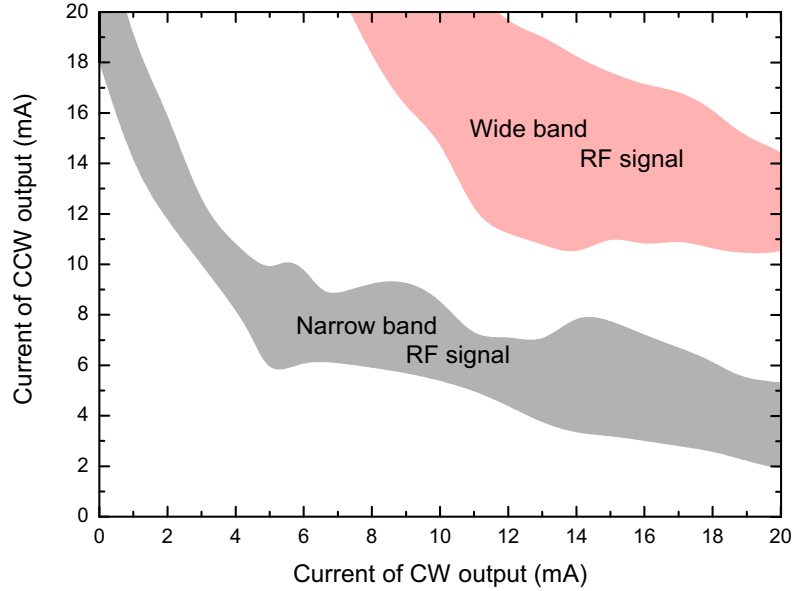


Figure 5.23: Mode locking map as a function of the current injected into the output arms at a ring current of 120 mA.

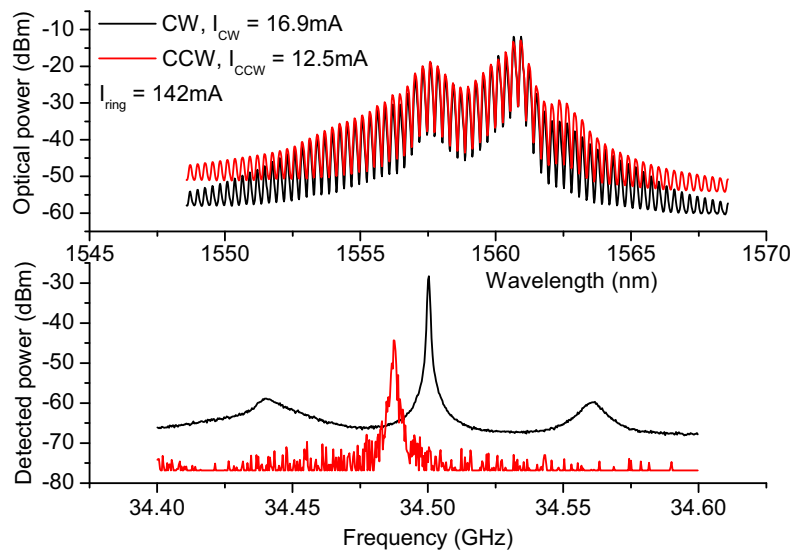


Figure 5.24: RF and optical spectra of the two directions at a current of 16.9 mA, 142 mA and 12.5 mA, injected into the CW output, the ring and the CCW output, respectively.

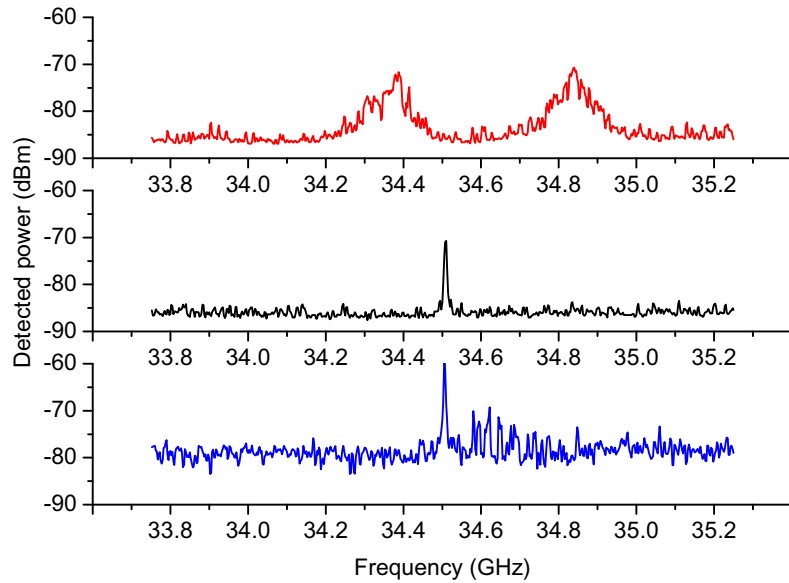


Figure 5.25: Examples of RF spectra, namely double peak (top), partial mode-locking (middle) and self-pulsations (bottom).

creasing injected current the laser periodically switches from one direction to the other because of the coupled cavity effect generated by the output waveguides. This section will show that the SRL is indeed a perfect optical multistable, in which both direction and wavelength can be selected by an external optical signal and that the new selected state is kept after removing the external injection.

A first set of experiments was performed to further investigate the directional mode switching behaviour for increasing current. The current of the laser was quickly raised from below threshold to a fixed current value. An automatic control/measure program was developed that repeats this sweep a large number of times and registers the direction of lasing. The probability values taken from 100 samples for each current were plotted in Fig. 5.26.

The plot indicates that the current value at which a mode directional switching occurs is not precisely defined but follows a statistical process. In the measurement of Fig. 5.26, a fast sweep to a current value of approximately 84.5 mA can provide either CW or CCW direction with almost equal probability. An increase or decrease in this current value favours one of the two modes but does not provide a sharp transition. As an example, a current of 84mA gives CW operation with a probability of 85% only. This probability increases as the current value decreases but never reaches 100%. Once the mode direction is selected it remains stable.

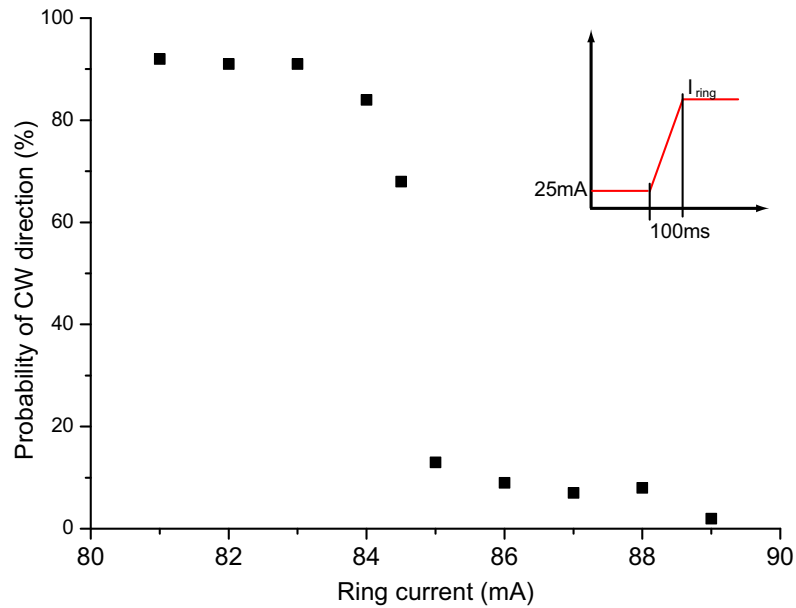


Figure 5.26: Probability of switching into the CW direction, when the current is quickly increased from below threshold to the indicated current value.

As an extension of the previous experiment, an external optical signal (from an external tunable laser) was injected into the non-lasing direction to induce a directional switching: when the injection is positioned on the lasing mode, the lasing direction takes the direction of injection. When the injection is removed the direction stays stable that proves optical bistable operation. The same experiment was also conducted, in which the external tunable laser not only switch the direction but also the SRL wavelength. When the external excitation is removed, several of the newly selected wavelengths stably remain in the new state. As shown in Fig. 5.27, as many as 12 stable states were found, 6 stable wavelengths in both directions. Furthermore, the cavity modes – neighboring the stable wavelengths – had lifetimes in the order of 0.5–1 second before getting repelled to one of the stable wavelengths. This type of multi-wavelength stability behavior is unique to SRLs, although the exact underlying mechanism is not fully understood yet.

The most obvious use of this effect is in all-optical memories. When we assume that the number of stable wavelengths is limited by the available gain bandwidth and the occupied chip area is proportional to  $R^2$ , we can quickly calculate that the number of available states per chip area is proportional to  $4\pi/R$ , where  $R$  is the ring radius. It can be seen, that the information storing density – defined as the available states per unit chip space – is the highest when  $R$  is kept at its technological

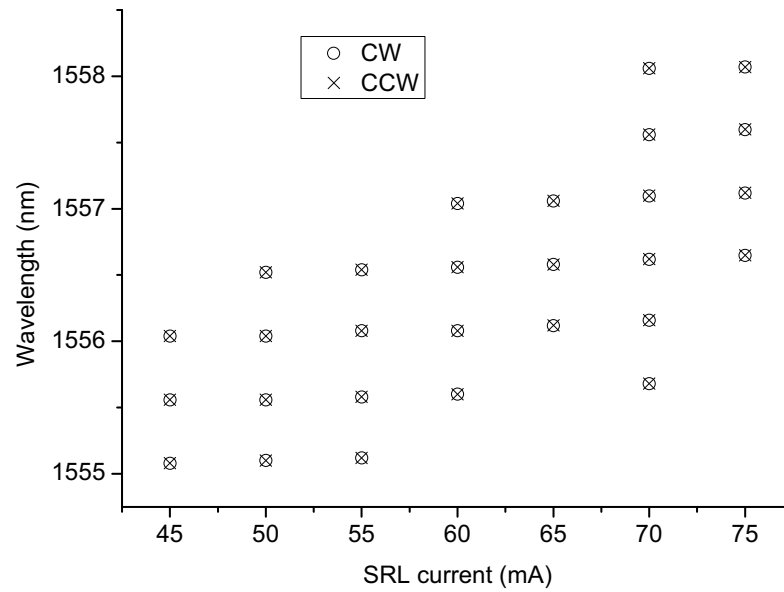


Figure 5.27: Stable wavelengths and directions versus ring current.

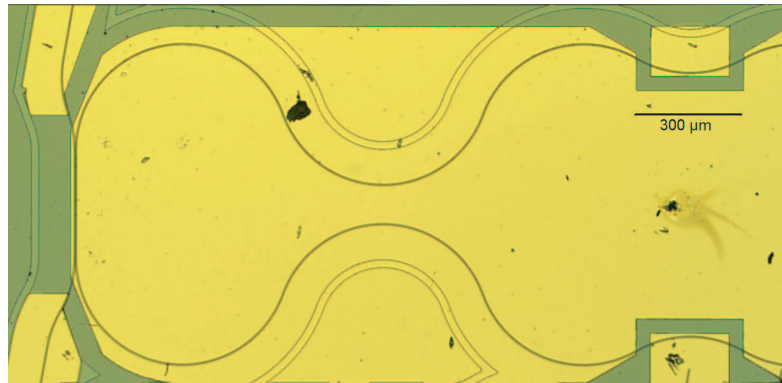


Figure 5.28: Optical microscope image of a folded mode-locked ring laser. The FSR was designed to be 9 GHz.

minimum. Therefore, micro-rings (having only two states by the two directions) are still the most attractive solution for all-optical memories. To increase the device length per unit area, the devices could be folded up (see Fig. 5.28), although it also requires  $R$  to be kept at its technological minimum.

## 5.6 Conclusions

The modal structure of SRLs were investigated by measuring the transfer properties of the device below threshold and the wavelength jumps that occur in connection with directional switching above threshold. A transfer matrix analysis explains the measurements when amplified spontaneous emission in the SRL cavity is accounted for. The residual reflectivity in the light extraction sections determine the frequency splitting and threshold difference between the two branches of solutions. This effect together with the redshift of the material gain explains the wavelength jumps displayed by SRLs in the unidirectional regimes. Furthermore, stronger feedback can destabilize the otherwise stable system and gives rise to a large variety of mode dynamics.

A feature unique to SRLs – namely multi-wavelength stability – were demonstrated. As it will be presented later, the existence of multi-wavelength stability has some very important consequences. When the laser is subjected to external injection for example, this effect allows for efficient cavity enhanced FWM, which leads us to the next chapter.

# Chapter 6

## Integrated SRLs

This chapter shows that unidirectional operation in SRLs – together with their potential for integration – enables the design of several novel devices, which can not be realized with FP or DFB technologies. The three sections in this chapter will study the integration of an SRL with a DFB to realize a master-slave configuration, an SRL with a DBR for ultra-fast wavelength tuning and an SRL with a tunable coupler for Q-switching operation. The results presented here were published or submitted for publication.

### 6.1 SRLs subjected to weak external injection

In the final remarks of the previous chapter it was concluded that external optical injection can lock cavity modes to certain wavelengths, where lasing remains stable even after removing the injection. Although injection locking is a well-known phenomenon that was extensively studied in semiconductor lasers [80], the multi-wavelength stability in SRLs was an unexpected result. Even more surprising was that for lower injection levels ( $< 10$  dBm), the SRL does not lock to the injector but generates a strong FWM signal between the self-lasing SRL wavelength and the wavelength of the injected signal. Again, a similar phenomenon has never been reported in FP lasers.

A strong enough injection can pull the laser's wavelength to the wavelength of the injector. This situation is utterly true for ring lasers as well, however, no real experimental study was carried out to investigate the effect of lower injection levels. This section details the experimental findings on the topic.

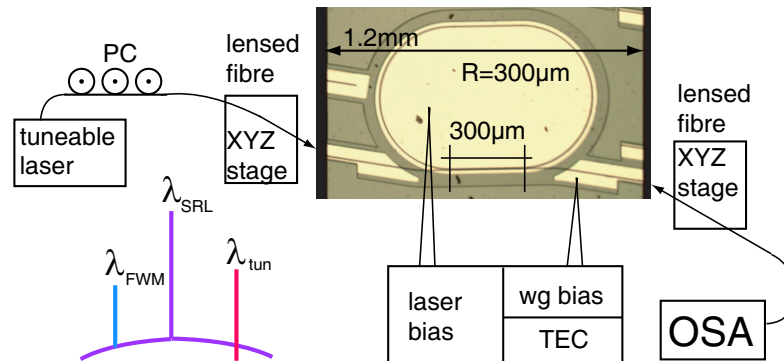


Figure 6.1: Optical micrograph of the 34.5 GHz FSR ring laser and the corresponding experimental setup used to measure the FWM signal. The output waveguide was biased to transparency.

### 6.1.1 Cavity enhanced FWM

The previously presented  $300\mu\text{m}$  radius SRL was driven at 130 mA in the unidirectional, single-mode regime, and was optically injected by a tunable laser, as shown in Fig. 6.1. The output of the tunable laser was fed through a lensed fiber to the input waveguide, and the polarization was maintained at transverse electric (TE). The counter-clockwise output of the SRL was collected by a lensed fibre connected to an OSA and an RF spectrum analyser with a high speed photodetector. The power of the tunable laser was kept at 0 dBm, which gives an estimated injection power of  $-23\text{dBm}$  to the ring cavity when the fibre-to-chip losses, the losses from the unpumped input waveguide and the coupling are considered.

Tuning the wavelength of the injection precisely onto one of the side modes of the ring laser gives a clearly enhanced cavity mode mirrored around the main lasing mode. This indicates a four-wave mixing process, where the injection acts as the probe, and the lasing mode of the SRL acts as the pump signal, as shown in Fig. 6.2. According to the literature, the non-linear process accounted for FWM – with a time constant below 1 ps – can most likely be spectral hole burning (SHB), while at lower frequencies carrier density pulsation (CDP) and carrier heating (CH) play a role as well [81]. The conjugate signal could be clearly observed when the injection was positioned precisely onto a ring cavity mode. However, a very weak FWM signal could also be detected with the injector detuned from the cavity modes, although the FWM signal was much lower due to the absence of the cavity enhancement effect. The total bandwidth in which a clear cavity enhancement of the FWM was detected is around 1 GHz. It is worth remarking that an FP

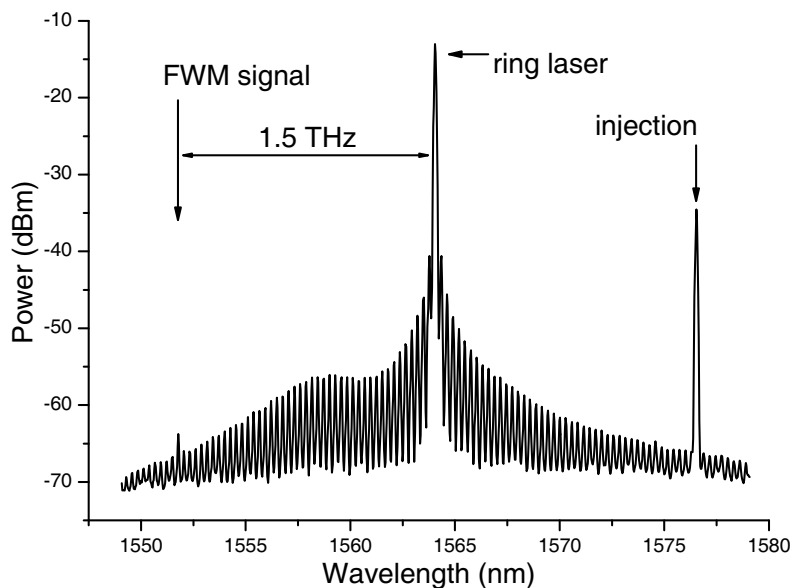


Figure 6.2: Injection into the 43<sup>rd</sup> mode away from the lasing peak (a detuning of 1.53 THz, 12.5 nm) gives a visible conjugate FWM signal.

laser subjected to optical injection on one of its cavity modes, either locks to the injector wavelength or, if the power is low, keeps lasing on its unperturbed lasing wavelength. To my knowledge, only one similar experiment was reported on FP lasers, in which the injected signal was precisely tuned in the middle between two FP cavity modes. In this scenario, the FP does not lock to the injector and a partial cavity enhancement of the FWM effect was reported [82].

The power of the conjugate signal was measured as a function of the injector detuning over consecutive cavity modes, while maintaining fixed SRL current (hence its wavelength and power), as shown in Fig. 6.3. The power of the FWM signal was found to increase exponentially with decreasing detuning. Furthermore, at this level of injection (-23 dBm), a central region was found where the injected signal pulled the mode of the SRL and injection locking occurred. The total drop in power of the conjugate signal was 45 dB when moving the injector from the first cavity mode to the 43<sup>rd</sup> mode.

According to [83], the FWM conversion efficiency scales with  $\sim (\Delta f)^2$ . However, the function connecting conversion efficiency and detuning is slightly more complicated but still the largest polynomial term is  $\Delta f^2$  [84]. Therefore, the conversion efficiency was plotted and it was fitted with a second order polynomial function in Fig. 6.4. Indeed, the shape of the curve nicely follows the expected

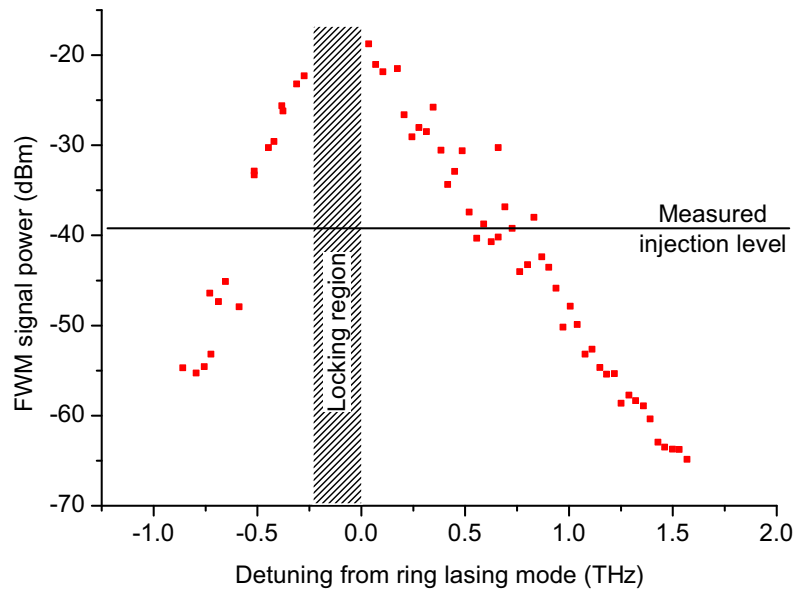


Figure 6.3: Measured power of the FWM signal as a function of detuning from the ring lasing mode. The injected power is kept constant and was measured to be -39 dBm at the output.

trend.

### 6.1.2 Unidirectional mode-locking

At smaller detuning values it was found that the external injection cascadingly locks several cavity modes of the SRL, as shown in an example spectrum in Fig. 6.5. Furthermore – as FWM is a phase dependent process –, it is expected that all the modes taking part in the FWM process are locked in phase. This assumption was confirmed by an external heterodyne measurement. First, the linewidth of the lasing mode was measured by beating the output with an external tunable laser with a linewidth of 100 kHz. The RF linewidth was measured to be 1.4 MHz, which corresponds to the linewidth of the SRL since the linewidth of the tunable laser is much lower than this value. On the contrary, the linewidth of the beat signal was observed to decrease from 1.4 MHz (the linewidth of the unlocked SRL) to less than 100 kHz, when the FWM was induced by external locking. In this case, the accuracy in the linewidth measurements is limited by the 100 kHz linewidth of the tunable laser due to the nature of the measurement technique.

Moving the injection to the adjacent cavity mode of the SRL's lasing mode

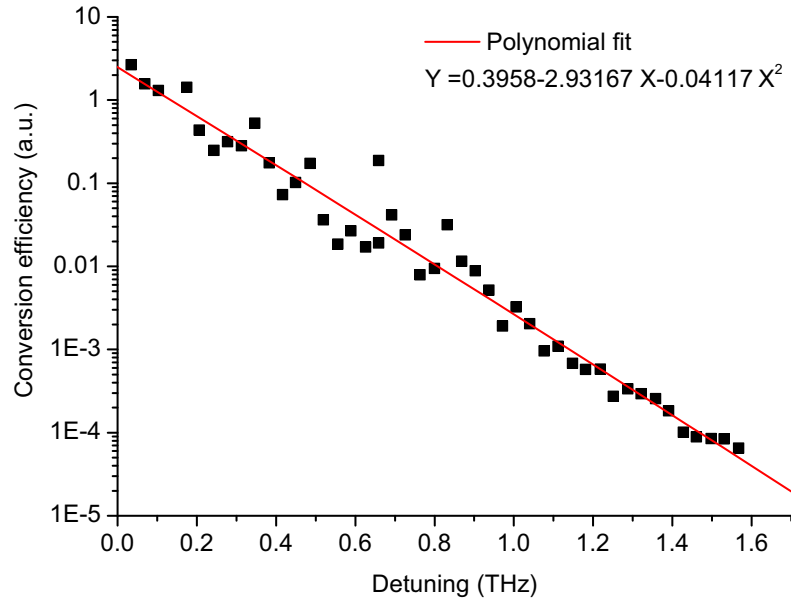


Figure 6.4: Measured and fitted conversion efficiency as a function of detuning.

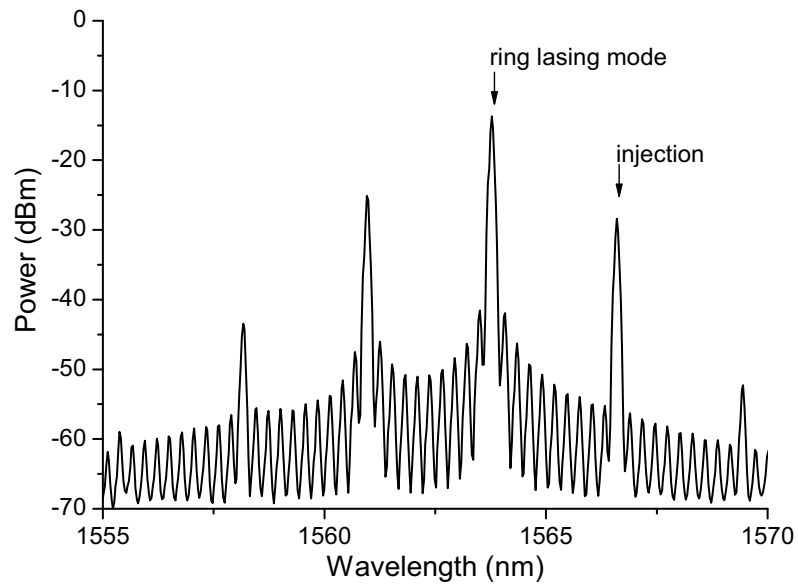


Figure 6.5: Cascaded locking of several cavity modes of the SRL by FWM.

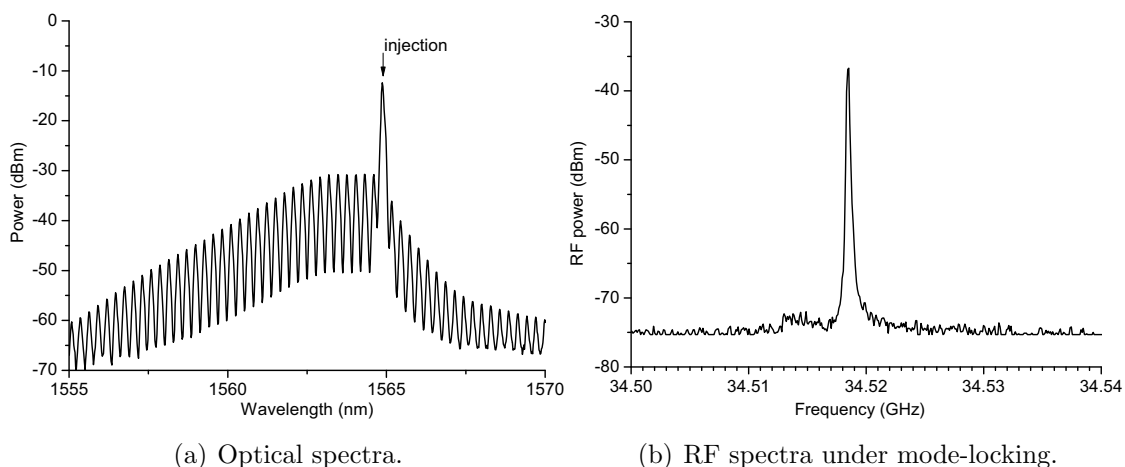


Figure 6.6: Optical and RF spectra when the injection is tuned to the adjacent cavity mode of the main lasing wavelength.

allows to directly observe the mode locking signal, since the FSR frequency of 34.5 GHz is within the measurable range of the fast photodiode and RF spectrum analyzer. In this case, all the cavity modes are locked in a range of 4 nm, considering the 3 dB full width at half maximum (FWHM) bandwidth, as shown in Fig. 6.6a. It can also be observed that the OSA spectrum gets flattened with a complete suppression of the main lasing mode.

The linewidth of the resulting electrical signal (plotted in Fig. 6.6b) was found to be around 5 kHz, being twenty times narrower than the linewidth of the injector (100 kHz) and two orders of magnitude lower than the linewidth of the single lasing line of the ring laser (1.5 MHz). When the linewidth of the tunable laser was increased to 500 MHz (using the built-in option of the tunable laser called coherence control), the linewidth of the resulting RF peak at 34.5 GHz was 2.2 MHz – two orders of magnitude lower than the linewidth of the injected signal. This phenomenon can only be explained by a locking of the cavity modes. In contrast with mode locking achieved by the nonlinearity of a saturable absorber, cavity enhanced FWM is the responsible nonlinearity. Mode-locking of a ring laser by an intra-cavity saturable absorber locks both the longitudinal and counter-propagating cavity modes, leading to bidirectional operation. While here, the counter-propagating direction remains suppressed, which is possible only by phase-locking of traveling waves without locking them spatially.

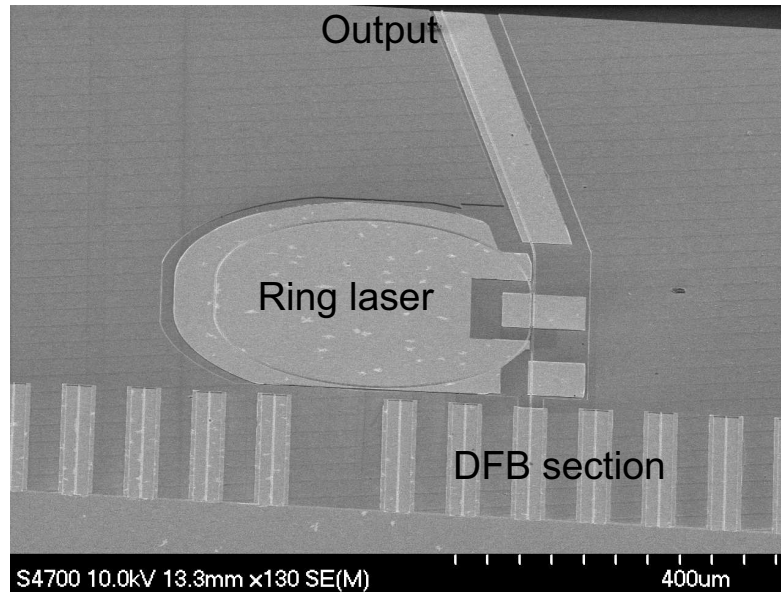


Figure 6.7: SEM image of an SRL integrated to a DFB. The additional DFBs that appear on the bottom cleaved facets were fabricated for testing purposes.

### 6.1.3 Integration of an SRL and a DFB

Monolithic integrated devices were also fabricated where the pump signal is generated by a DFB monolithically integrated next to the SRL. Fig. 6.7 shows an SEM image of the integrated device; an extra contact is added to control the injection level of the DFB.

The SRL and the DFB have threshold currents of 28 mA and 19.5 mA, respectively. The ring laser showed unidirectional, single mode operation with SMSR in excess of 25 dB, while the on chip DFB has an SMSR of 50 dB. The optical spectra of the individually operated SRL and DFB are plotted in Fig. 6.8.

The grating of the DFB was designed to match one of the cavity modes of the SRLs and fine tuning of the wavelengths was obtained by varying the injection currents of both the SRL and the DFB. Since the two lasers were fabricated on the same chip, and thus subjected to the same temperature changes, the long-term stability of the injection locking was strongly enhanced. Fig. 6.9 shows the generated FWM signal in the monolithically integrated device when the DFB wavelength is injected into one of the SRL cavity modes.

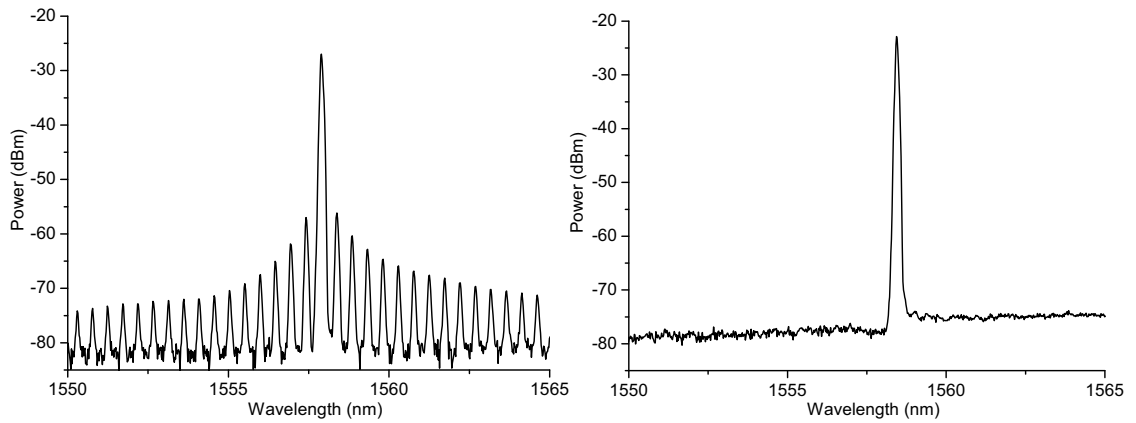


Figure 6.8: Optical spectra of the integrated SRL (left) and DFB (right) at a current of 98 mA and 60 mA, respectively.

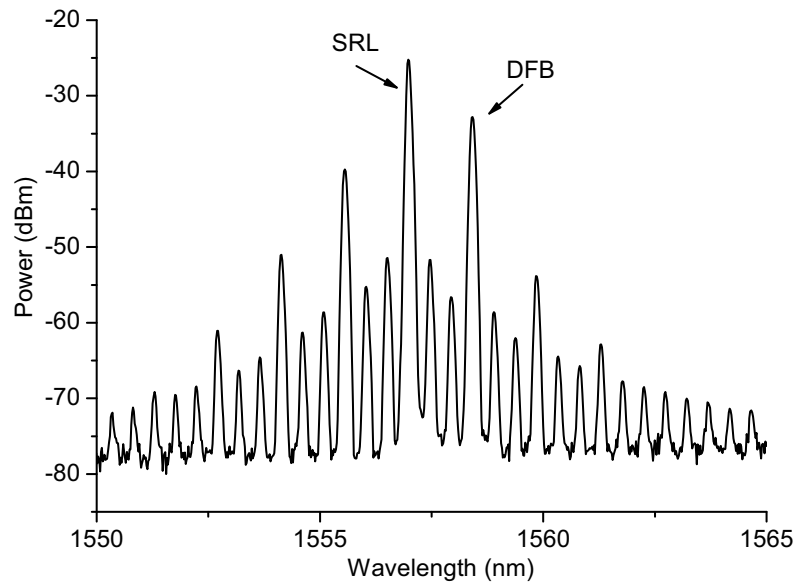


Figure 6.9: The resulting optical spectrum when the ring and DFB are operated together.

#### 6.1.4 Master-slave configuration

The previously presented device can be regarded as an integrated master-slave configuration, where the master laser (the DFB) optically injects the slave laser (the SRL) without getting influenced by the slave, thanks to the unidirectional operation. A similar configuration with FP or DFB lasers only would require a bulky optical isolator to protect the master from back reflection from the slave.

The high stability of the integrated device allowed for a precise mapping of the injection locking characteristics of the SRL. Using the intermediate contact pad (to change the injection level) and the current of the DFB (to change the lasing wavelength), a detailed injection locking curve can be plotted by examining the output spectra of the SRL.

The lasing mode was mapped around a wavelength of 1558.6 nm that corresponds to the lasing mode of the SRL. As a function of detuning and injection level, the following regimes were found (Fig. 6.10):

**Unlocked or beating zone.** Here the injection does not influence the SRL, only the beating of the two lasers is visible on the RF spectra. As the wavelength of the DFB approaches the ring's cavity mode at 1558.6 nm, occasional mode-jumps can be induced, where the SRL's lasing wavelength jumps to the cavity mode near to the injection wavelength.

**Stable locked zone.** The slave is stably locked to the wavelength of the injection. As expected, the SMSR of the SRL increases to value up to  $-45$  dB and no dynamics appear on the RF spectrum analyzer.

**Unstable locked or self pulsation.** Here, the locking is not stable, the field of the SRL shows a self pulsating signal around 1.9 GHz. In this case, the side-mode suppression is not increased.

**Chaotic regime.** The optical spectrum of the SRL becomes wider and the time-domain signal of the SRL becomes chaotic. The RF spectrum shows a flat and wide spectrum up to 2 GHz (Fig. 6.11).

**Mode-locking.** In the optical domain, a stable multi-mode spectrum appears that resembles very much the spectra previously measured in the mode-locking regime. However, the large FSR frequency of the device (64 GHz) did not allow for a more accurate analysis of the RF spectra.

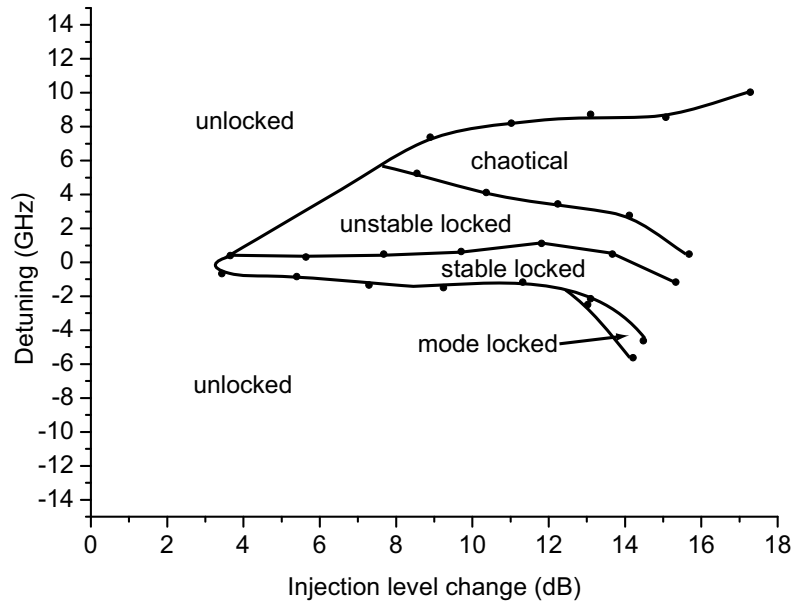


Figure 6.10: Optical injection locking map indicating the different regions at a ring current of 89 mA. The 0 dB, 0 GHz reference point corresponds to  $-30$  dBm injection level from the DFB at an SRL lasing wavelength of 1558.6 nm. Negative frequencies correspond to an injection below the lasing wavelength.

It must be emphasized, that the different regions and the shape of the locking curve show a very good agreement with the theoretical predictions for a master-slave configuration, described in [85]. In particular, the asymmetry of the locking region – i.e. stable locking is achieved only for negative detuning – is due to the linewidth enhancement factor.

Because of the very large parameter space, further investigation of the integrated device was not performed. To give an idea on the complexity of these measurements, the graph of Fig. 6.10 was obtained by processing as many as 4 million measurements points, since the output power is measured on a 3-D parameter space (wavelength, DFB bias and bias of the intermediate contact). Furthermore, this measurement corresponds to only one ring current and one cavity mode of the ring. Although most of the data processing was computer-controlled, the overall process was still very time-consuming. Future works will include the mapping of the locking characteristics of non-lasing ring cavity modes to gather a better understanding on the FWM stability and frequency bandwidth.

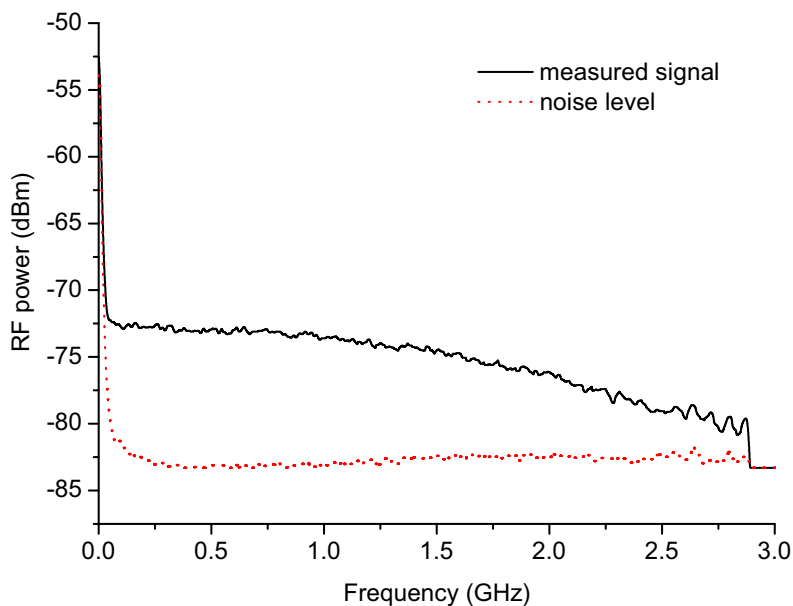


Figure 6.11: RF spectra in the chaotic regime.

### 6.1.5 Applications

#### Micro and mm-wave generation

An attractive way for generating coherent radiation in the microwave and mm-wave region is photomixing or optical heterodyne of two laser beams [86]. However, the temperature dependence of the emission wavelength together with the large free-running linewidth of semiconductor lasers set a severe limitation in the stability and spectral purity of the generated signal. The stability of the signal can be improved complicated phase-lock loop techniques [87, 88]. Alternatively, mode-locking can provide an improved linewidth [14, 82] but achieving high-power at high repetition rate is challenging because the repetition frequency scales with the device size.

The measurements presented here indicate that an integrated SRL+DFB configuration is viable and promising option for high-frequency (in the THz range), narrow-linewidth (in the kHz range) signal generation. Furthermore, this can be achieved in a compact, integrated fashion with step-tunability. Also, the viability of FWM for generating coherent THz radiation was already demonstrated in external cavity lasers [89], but no such configuration was achieved with integrated devices before.

### Wavelength conversion

Wavelength converters are key elements of wavelength division multiplexing (WDM) networks. There are a large number of approaches to achieve all-optical wavelength conversion such as cross-gain-modulation in SOAs, cross-phase-modulation in SOAs, FWM in SOAs or difference frequency generation [90].

The presented configuration has some advantages and disadvantages over existing wavelength converters. Advantages are:

- All the other techniques require an external pump-signal (with powers in the order  $> 10$  dBm), while here the SRL provides the intra-cavity pump signal.
- The device (SRL+DFB) size is a fraction of most of the other technologies, which require an additional external pump laser.
- High conversion efficiency because the cavity enhancement effect.
- Allows for simultaneous conversion of multiple input wavelengths into multiple output wavelengths, as shown in Fig. 6.12.
- After conversion, the chirp is reversed.
- It is a simple structure with the potential for further integration. As an example, electro-absorption modulators or SOAs can be integrated on the output waveguide.
- Multi-wavelength broadcasting is feasible.

The disadvantages are:

- The bandwidth in which FWM can be achieved is around 1 GHz, which is the price to pay for the non-linear enhancement provided by the ring resonant effect. Although this bandwidth is already sufficient for a number of LAN applications, it has to be largely increased if the device has to be used with WAN high-data rate signals. An option that is currently being investigated is the use of identical coupled SRLs with high coupling factors. The Q-factor of the single SRL is largely decreased, hence its linewidth and FWM bandwidth are largely increased. However, the strong non-linear enhancement is still provided by the resonant effect of the coupled chain of SRLs. A very similar approach is used in the design of slow-wave delay lines [91].
- Conversion wavelength range is not the best ( $\sim 10$  nm).

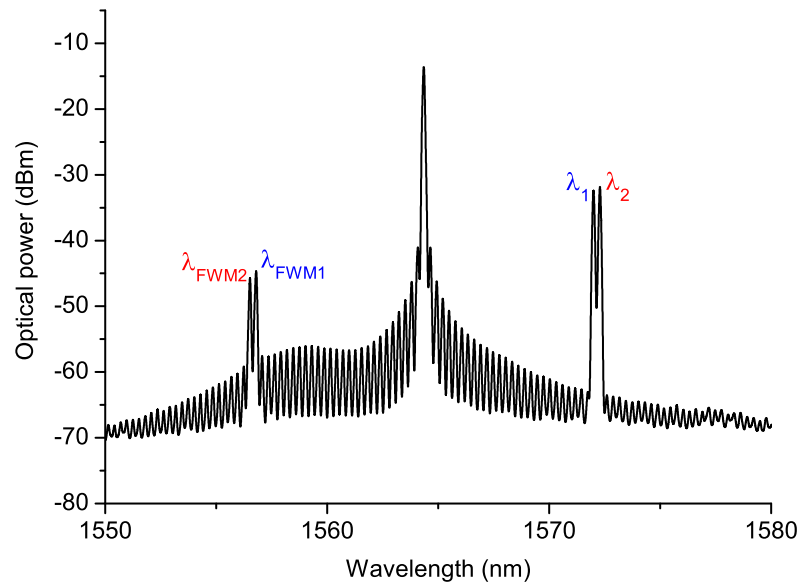


Figure 6.12: Optical spectra with two color injection showing simultaneous conversion of multiple input wavelengths.

- Conversion is limited to fixed wavelength spacing – usually it is not a problem.

In summary, this wavelength-conversion approach do not outperform the other techniques in many ways, but their simplicity, low cost, low power requirements offer possible applications in future end-networks.

### Optical logical functions

The observed cavity enhanced FWM allows for realizing all-optical logical functions. A FWM signal only appears at a cavity mode when both SRL and the input injection is at the correct wavelength, which realizes a logical *AND* function. Unfortunately, the bandwidth is still limited by the cavity lines<sup>1</sup>.

### Dynamics studies and encrypting

The use of chaotic systems was proposed for cryptographic applications [92] and a few interesting systems were already reported. Optical chaos is typically generated by a master-slave configuration at the transmitter and signal decryption is achieved by an identical chaotic system at the receiver. One of the major challenges

<sup>1</sup>Although, it was not confirmed experimentally.

is to generate two identical chaotic signals at the transmitter and receiver. This problem is exacerbated by the use of bulk systems with very tight alignment requirements; therefore, a completely integrated chaotic signal generator would prove very beneficial.

## 6.2 Rapid tunability by wavelength selective feedback

The following section presents the results on the fast tunability of SRLs subjected to wavelength-selective feedback. Tunability of the SRL is demonstrated on a completely integrated device, in which a DBR is defined on one of the output waveguides of the SRL. This device represents the main objective of the EPSRC grant RAPTOR, which funded most of the presented research activity.

### 6.2.1 Design and cw characterization

The devices employ a racetrack cavity ring (free spectral range of FSR=64 GHz) with a ring radius of 200  $\mu\text{m}$  and 100  $\mu\text{m}$ -long evanescent field couplers defined on both sides of the ring cavity, as shown in Fig. 6.13. Two additional electrical contacts are defined on the couplers to provide tunability of the coupling ratio (as described earlier in Section 2.2.4) and a fine control over the optical feedback from the DBR. One of the output arms is connected to a 200  $\mu\text{m}$ -long waveguide lateral grating with a grating period of 245 nm and 500 nm recess on each side. The DBR is terminated by a blind 10° tilted waveguide to avoid any unwanted backreflection from the end facet, while the other three outputs have 10° tilted output facets. The couplers, the output waveguides and the DBR were intermixed, with a measured bandgap shift of 35–40 nm. Due to the high temperature annealing step, the devices showed some gain degradation and a relatively large threshold current, in the range of 110–120 mA.

The DBR reflection peak and stopband can not be easily measured on the fabricated devices because the DBR does not have an accessible output for transmission measurements. However, an indication on the location of the reflection peak can be obtained by biasing the SRL below threshold and collecting the light from output1. Fig. 6.14a shows the spontaneous emission spectra filtered by the ring cavity modes and enhanced by the DBR peak reflection. A more precise assessment of the grating's coupling coefficient  $\kappa$  was performed by sub-threshold measurements on a separate 600  $\mu\text{m}$ -long DFB, fabricated on the same chip. Fig. 6.14b indicates that the width of the stop band is 1.02 nm. The estimation of the coupling coefficient was carried out by fitting the sub-threshold spectra with a freely distributed program called Laparex [93]. The fitting gave an estimated coupling coefficient of  $\kappa = 52 \text{ cm}^{-1}$ , which is a typical value for side-grating DBRs [94].

Injecting current into the DBR results in a continuous decrease of the reflec-

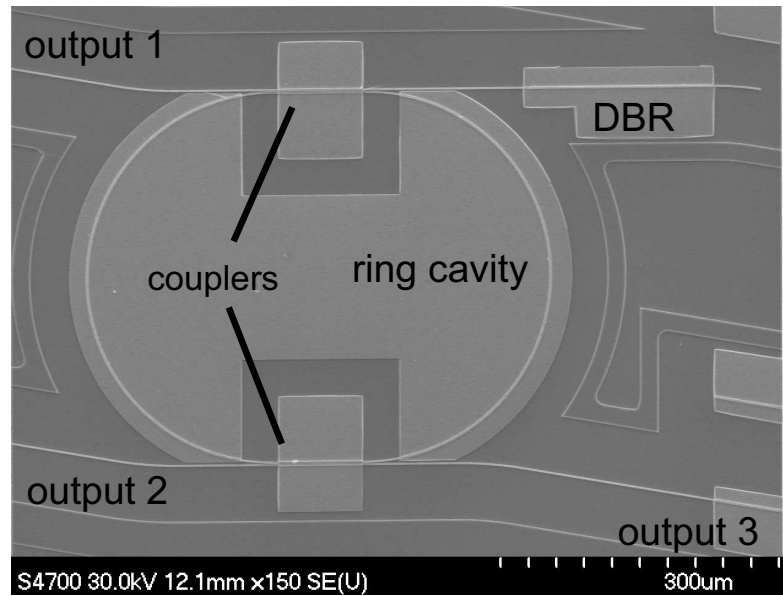
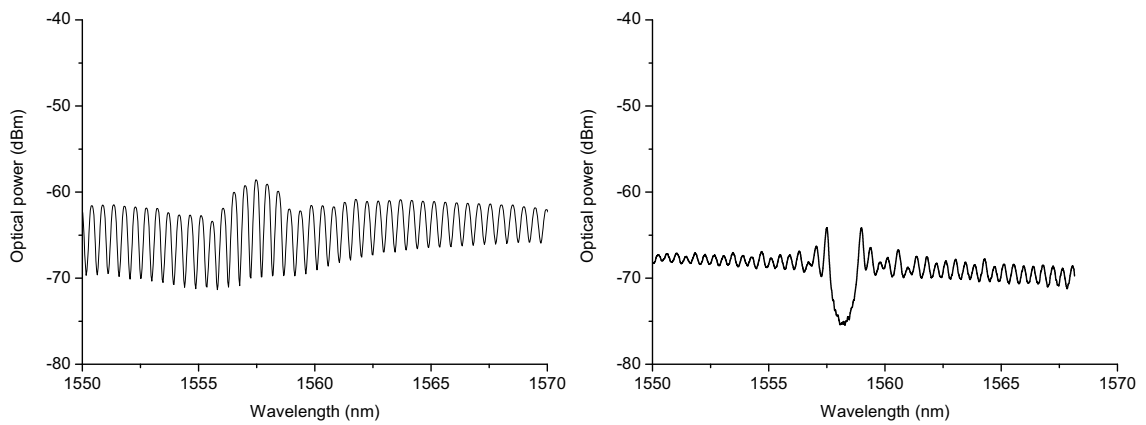


Figure 6.13: SEM image of the ring laser monolithically integrated next to a DBR.



(a) Subthreshold spectra of the integrated device measured from output1. .

(b) Subthreshold spectra of DFB.

Figure 6.14: Grating assessment.

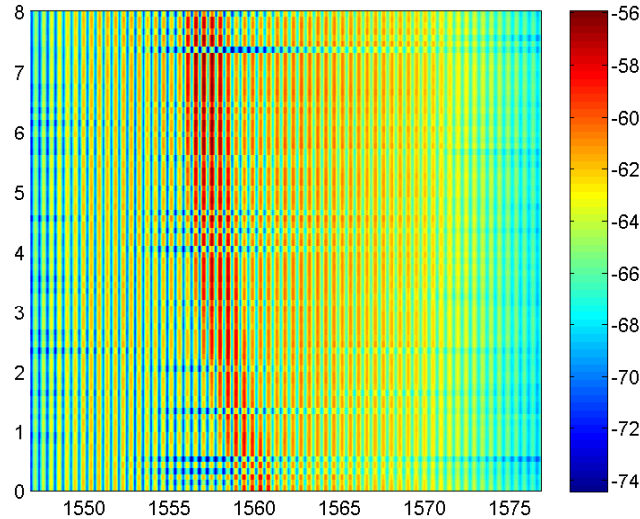


Figure 6.15: Subthreshold wavelength map taken from output1 at a ring current of 64 mA as a function of the DBR current.

tion wavelength due to the plasma effect. The tuning performance of the DBR as a function of the injected current can be extracted from the SRL subthreshold wavelength-map, shown in Fig. 6.15. It also must be noted that the shift in wavelength saturates above a current of 5 mA. The limited tunability can be explained by thermal heating, which causes red shift of the wavelength and decreases the blue-shift of the plasma effect.

The SRL's tunability was assessed by biasing the ring cavity at a constant current of 180 mA ( $1.5 I_{th}$  threshold current) and in a situation in which the DBR peak is perfectly matched to the SRL lasing mode. Here, the lasing wavelength of the SRL is locked to the reflection peak of the unbiased DBR. An optical spectrum was taken at every 0.1 mA of DBR current up to 5 mA from output3 while the ring current was kept constant. Fig. 6.16 shows exemplar optical spectra with the SRL lasing on three consecutive cavity modes. Both the wavelength of the SRL and the peak DBR reflection is plotted in Fig. 6.17 as a function of the DBR current. It can be seen that shifting the reflection peak of the DBR results in a step-like tuning of the SRL wavelength via consecutive ring cavity modes.

As expected, the asymmetric coupling between clockwise and counterclockwise modes induced by the grating favors unidirectional operation, which was confirmed by measuring a 15 dB power suppression from output2. It appears that for current

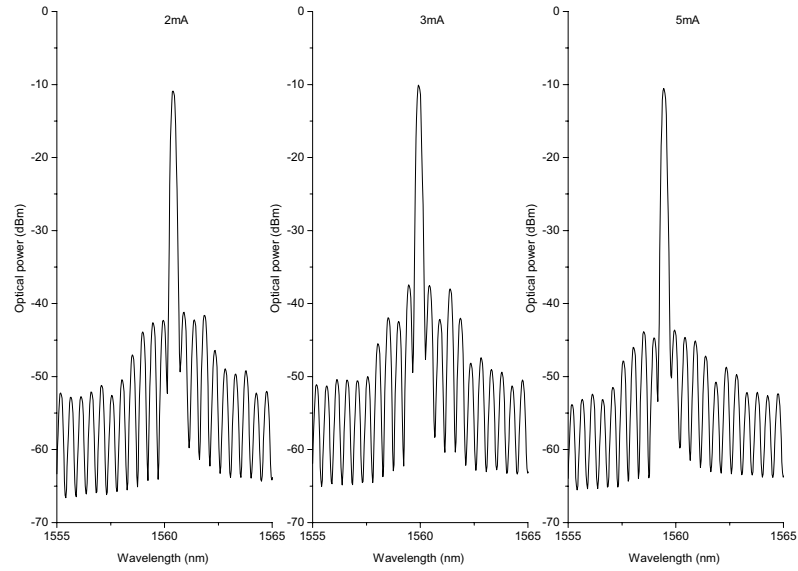


Figure 6.16: Optical spectra at 2 mA, 3 mA and 5 mA of DBR current.

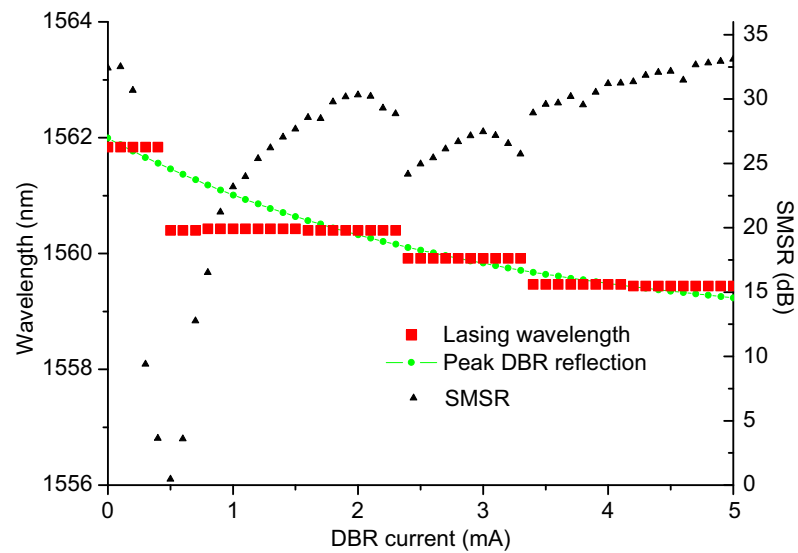


Figure 6.17: Lasing wavelength (squares), DBR peak reflection wavelength (circles) and SMSR (triangles) at a ring current of 180 mA as a function of DBR current.

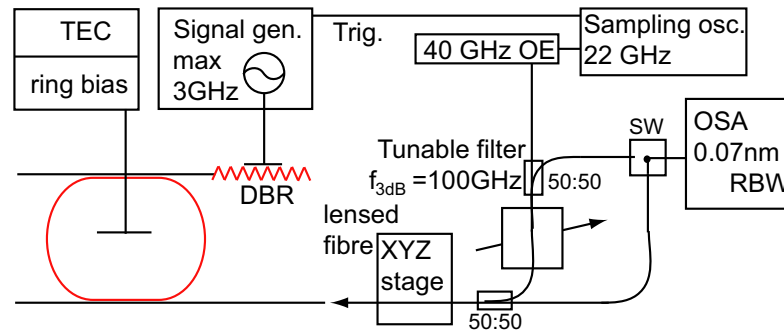


Figure 6.18: Setup to for high speed measurements.

levels smaller than 1 mA a multi-mode operation regime with a very low SMSR takes place. As soon as the DBR current exceeds 1 mA, the SRL exhibits stable and single mode behaviour with the maximum of the SMSR occurring where the SRL and DBR wavelengths are the same. In Fig. 6.17, this situation corresponds to a perfect overlap between the green and red curves. It was also found that tuning the wavelength of the DBR reflection peak only slightly affects its SMSR. Since current injection not only tunes the DBR wavelength but also marginal increases its reflectivity, this suggests that stronger value of feedback enhance the single-mode performance of the SRL. Since the coupling ratio of the coupler was already set at its maximum value, this effect could not be investigated any further. Future devices will be designed with either a stronger coupler or an SOA integrated between the DBR and the SRL to provide control over the total feedback level injected into the ring cavity.

### 6.2.2 High speed performance

High speed measurements were carried out using the setup shown in Fig. 6.18. Output3 of the device was collected by a lensed fiber and it was connected to a tunable filter. The output of the filter was then visualized on a sampling oscilloscope connected to a high-speed photo-detector. The DBR was modulated by a high-speed signal generator whose trigger output allowed the synchronization of the sampling oscilloscope.

Switching between two wavelengths was induced by injecting a 1 mA peak to peak sine wave (DC bias of 3.5 mA) into the DBR while keeping the ring current at a fixed value of 180 mA. As shown in the time traces in Fig. 6.19, the switching speed was found to be as fast as 450 ps and very robust against slower thermal

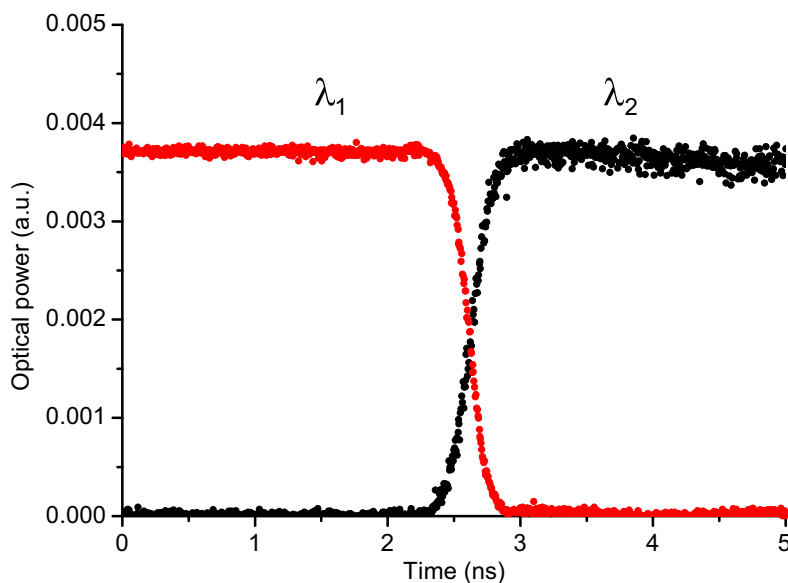


Figure 6.19: Measured time trace of switching from  $\lambda_1 = 1560.4$  nm to  $\lambda_2 = 1559.9$  nm by applying a 1 mA peak to peak sine wave (3.5 mA DC bias) to the DBR with a frequency of 50 MHz.

fluctuation of the DBR wavelength. The modulation frequency in this case was 50 MHz, and across the whole period of 10 ns, stable output signal was found. The maximum achievable modulation frequency of the DBR was 1.4 GHz, mainly limited by the electrical contacts that were not optimized for high-speed operation. At frequencies exceeding 1 GHz, a ringing appears on the time trace, indicating the presence of carrier recombination effects in the DBR.

Furthermore, a similar switching experiment was performed by injecting a 5 mA peak to peak sine wave with a DC bias of 3.5 mA. The resulting wavelength shift of the DBR tunes the SRL wavelength by up to four cavity modes, as shown by the optical spectrum of Fig. 6.20. The optical spectrum can not visualize the fast transition of the SRL through consecutive cavity modes and only shows the total output power of each mode.

### 6.2.3 Applications

Tunable lasers – offering fast tuning speed and low thermal wavelength drift – will be a key technology in realizing optical packet based networks [95]. The measurements on this device prove that this configuration is viable for applications requiring very stable and fast wavelength reconfiguration.

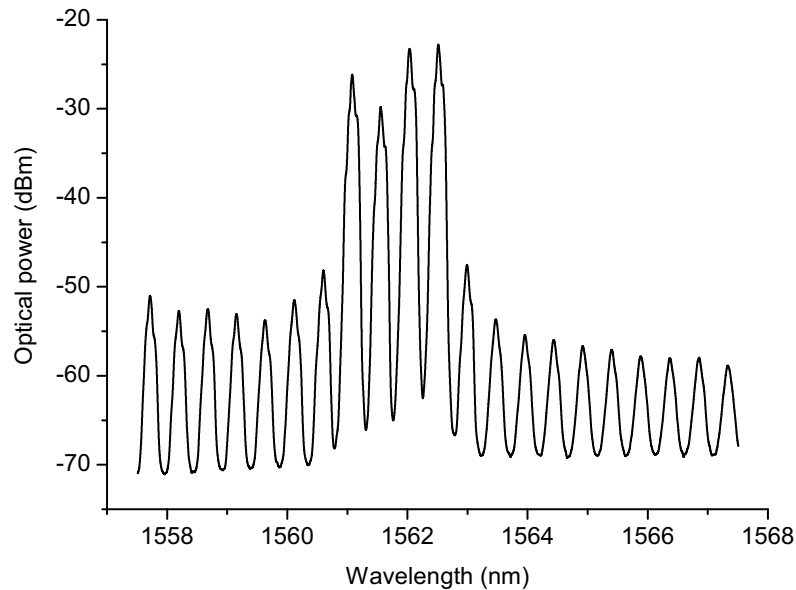


Figure 6.20: Optical spectrum during modulation when four wavelengths were addressed.

Standard and commercial technologies usually involve multi-section DBRs [96, 97] but their tuning speed is limited by the thermal drift occurring after changing the currents to the Bragg grating. An additional limitation to the tunability speed comes from the phase matching section, which is required to phase-match the cavity modes to the DBR wavelength. The complicated multi-variable look-up table controlling the tuning makes it difficult to predict the thermal load change and its effect associated with each tuning action, which limits the tuning speed to typically a few  $\mu\text{s}$  and increases the cost of devices.

The major novelty in the proposed configuration is that the tuning element is not part of the lasing cavity and that the output wavelength is stably defined by the ring cavity modes. The DBR is only employed to select one of the longitudinal modes of the ring cavity without affecting its stability. The concept therefore enables very fast tuning by separating the mechanism that defines stable lasing mode frequencies (the ring cavity) from the tuning mechanism (the grating) that only selects one of these stable frequencies. There is no need to tune simultaneously the laser current, the DBR current and the phase section element to achieve the desired output wavelength, as required by other configurations. The wavelength tuning is also digital in a step-wise manner, which is an added advantage for WDM applications. The FSR of the SRL can be precisely designed to match any wavelength

grid.

It is also worth to mention the possible applications for all-optical logics because the wavelength tuning speed figures are comparable to the directional switching between the counter-propagating SRL modes [98]. Injecting a signal at other wavelengths than the Bragg wavelength would injection-lock the SRL, providing a logical *NOT* function at the Bragg wavelength. Furthermore, by changing the feedback strength of the DBR, an *optical comparator* device can be easily achieved.

Even though, the values of the switching speed reported are very encouraging, a number of improvements can be made to the device. The limited tuning range can be increased by using sampled-grating technology, while the maximum modulation frequency can be enhanced by utilizing field effects such as the quantum-confined Stark effect and by fabricating the devices on semi-insulating substrates [99].

## 6.3 Q-switching in SRLs

This section presents findings about devices employing tunable couplers.<sup>2</sup> First, the cw properties then high-speed operation are presented.

### 6.3.1 Tunable coupler devices

To assess performance of devices with tunable couplers, a set of 200  $\mu\text{m}$  radius SRLs were fabricated with coupler length ranging from 0  $\mu\text{m}$  to 450  $\mu\text{m}$  (with intermixed couplers). The coupling length was designed to be about  $l_{100} = 400 \mu\text{m}$ . Therefore, the fabricated coupling gap width was 600 nm. Unfortunately, this set of devices was the first one that was fabricated using an HSQ mask. Despite all the testing, dry etching optimization and careful selection of etching time the couplers showed an RIE lag. As mentioned earlier in Section 3.5.2, using HSQ resist and large samples causes a decrease in etch speed due to higher load to the etching plasma. At the time this effect was unknown, so the RIE lag resulted in a shortening of the coupling. However, the large number of device versions still allowed for a thorough characterization of tunable couplers.

As shown in Fig. 6.21, the threshold currents show a periodic trend indicating a maximum at about 150  $\mu\text{m}$ . The coupling ratio was also measured on stand-alone couplers and the fitting indicated a coupling length of  $l_{145} = 400 \mu\text{m}$ . The same numerical analysis as described in Section 2.4 was applied for these structures. The result of the analysis is also plotted in Fig. 6.21 that matches well with the trend of the measured values. Surprisingly, both the measurement and analysis indicates that lasing is achievable even with coupling ratios close to 100%. Also it is worth to notice the increasing trend in threshold currents that is simply a result of longer and longer device length.

To assess the tunability performance, the device with a coupler length of 150  $\mu\text{m}$  was chosen. The LI curves of the device were taken with pumping current symmetrically into the couplers. The result is plotted in Fig. 6.22. It can be seen that the original threshold current of 180 mA quickly decreases to below 100 mA with pumping as small as 1 mA into the coupler. This result already gives some insight into the change in coupling coefficient. Fig. 6.23 shows the full trend of change in threshold currents. The current injection induces major reduction of the threshold current up to currents of 3 mA, a somewhat limited effect at higher values.

---

<sup>2</sup>To review the design and results on separate tunable couplers, one must page back to Section 2.2.4 and Section 4.3.2, respectively.

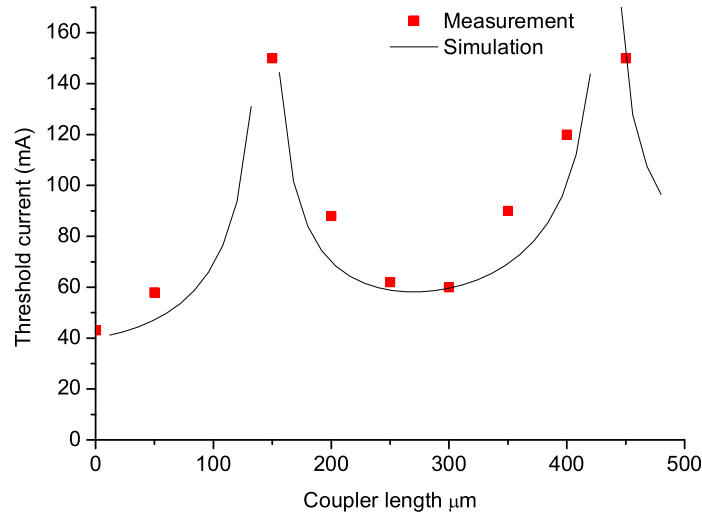


Figure 6.21: Measured and simulated threshold currents of 200  $\mu\text{m}$  ring radius SRLs with different coupler lengths.

One would expect that this effect can be accounted to the saturation of change in coupling, however, the analysis reveals that it is not necessarily true. Fig. 6.23 also contains the expected threshold currents as a function of the coupling ratio<sup>3</sup>. Despite the two curves were not attempted to be fitted for the coupling:current ratio, the expected trend also indicates a saturation of threshold current change. The fitting was not carried out because there are too many other unknown parameters, such as the nonlinearity of the coupling, the gain-loss figures induced by the coupler and the change in confinement, all of them are a function of both current and wavelength. On top of that, residual coupling and crosstalk were not even mentioned.

Furthermore, the output power was recorded when the ring current was kept constant and the current of one the couplers was slowly increased. Fig. 6.24 indicates that at around 3.6 mA the SRL suddenly starts to lase with a major increase in power.

This measurement alone supports the idea that there is an additional effect coming from the saturation of waveguide losses and not the change in coupling. To be able to efficiently relate these results, a few words must be said on the popular

<sup>3</sup>For consistency, it shows 1-coupling, left hand side corresponds to 100% coupling ratio.

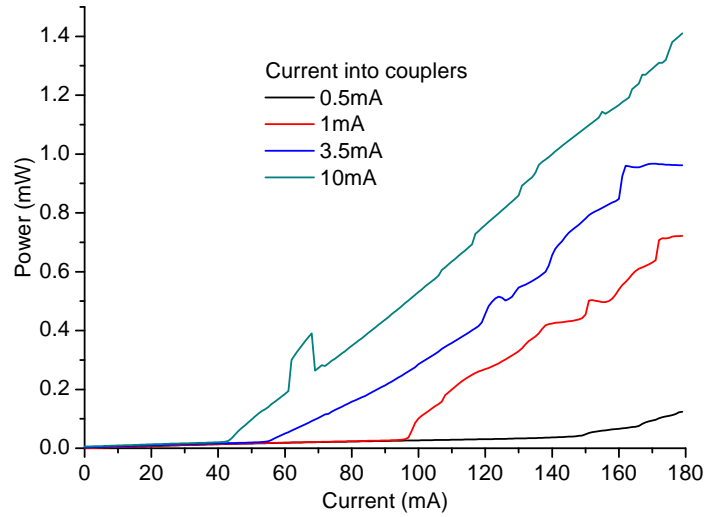


Figure 6.22: LI curves of the  $150\ \mu\text{m}$ -long coupler device at different coupler currents.

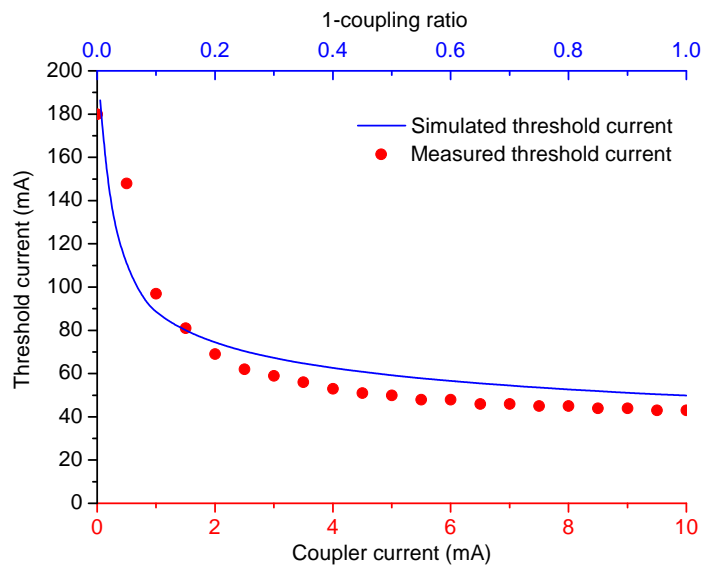


Figure 6.23: Measured and simulated threshold currents.

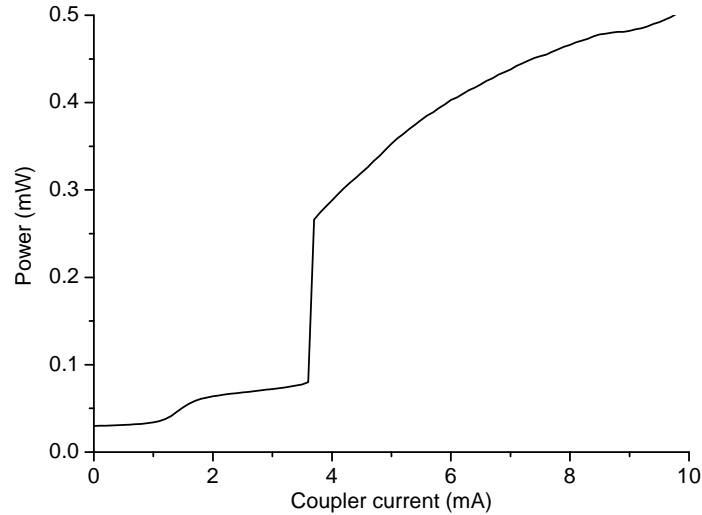


Figure 6.24: Output power as a function of coupler current when the SRL current is fixed to 120 mA.

cavity damping technique, namely when a saturable absorber is placed inside the cavity. In that case the following operation regimes can be observed:

1. At a certain current and reverse bias, the laser does not lase because of the strongly damped cavity.
2. Decreasing the voltage of the saturable absorber slowly decreases the losses.
3. At some point, the gain overcomes the losses, lasing action starts. At the same time, the increased intensity in the cavity saturates the absorber and the power suddenly increases.
4. Increasing again the voltage, at some point lasing action stops.

Because of the saturable of absorption, the two switching points are always at a different reverse bias values: the off-on and on-off transitions show a hysteresis. On top of that, at the off state the carriers accumulate to achieve a strong population inversion, which allows for passive Q-switching operation at the boundary of the states. During passive Q-switching or self pulsation, the energy is periodically released from the cavity, the repetition frequency can not be directly controlled,

it is a function of pump rate, cavity design and material parameters such as the carrier recovery time.

The measurement on the tunable couplers however indicates a completely different scenario: no measurable hysteresis was observed when the current was increased or decreased. Therefore, revealing the sudden switch-on/off of the laser requires a more careful analysis. Fig. 6.25 indicates the simulated output power of an SRL as a function of the coupling for different SRL currents. Even though, the figure plots the ideal case (no gain or loss in the couplers, no crosstalk), it allows to draw some very important conclusions. Most importantly, the change in coupling alone can explain the sudden increase in output power: a few percent changes in coupling allow the transition from no lasing to extract almost 80 % of the theoretical maximum power when the laser is strongly pumped. The analysis also revealed some extraordinary potential: with stronger gain (for example IQE with no degraded gain coming from annealing), the same figure can be achieved by a change in coupling from 0.1 % to 1 %. Furthermore, it is not necessary at all that a decrease in coupling decreases the output power, most of the time it is the other way around, depending on both the operating condition and the coupling. This observation was also confirmed by measurements, lower initial coupling resulted in almost no change or a slight decrease in output power while stronger couplers showed an increase in output power when the coupler was tuned. The limit of the device operation for Q-switching is also revealed. It seems that the maximum power change is limited not by the robustness of devices (how much current we can pump) rather the maximum coupling we can achieve: with a crosstalk of only 5 %, the laser in question would already start to lase at a current of 100 mA. Therefore, high pump rate without lasing and high output power with minimal change in coupling can only be achieved with an initial coupling ratio of 100 % with minimal crosstalk. This criterion requires the development of short and narrow gap evanescent field couplers.

Finally, comparing the simulation results with Fig. 6.24 allows us for the conclusion, that the measurement follows the expected trend: no lasing, sudden increase, then slow increase in power (without hysteresis). Therefore – even though it is similar to saturable absorption – it is a fundamentally different mechanism. It is worth to note that in this case only one coupler was pumped to reveal the fine structure of the switching mechanism, providing a zoom-in around the very strong couplings. Pumping both couplers with the smallest available current results in an immediate switch-on of the laser.

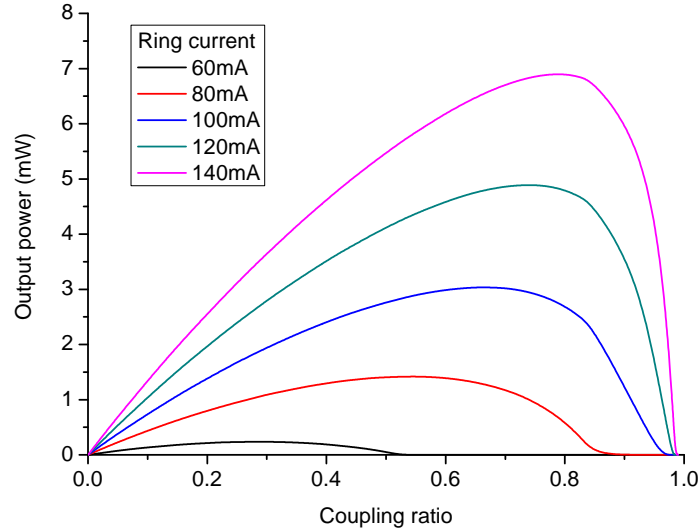


Figure 6.25: Simulated output power as a function of coupling coefficient for different ring currents.

### 6.3.2 Q-switched operation

According to the previous measurements, the  $150\ \mu\text{m}$ -long coupler device had the most potential for Q-switching applications. The SEM image of the device is plotted in Fig. 6.26.

The SRL exhibited a clear Q-switching behaviour when the current on the coupler was modulated at frequencies from a few tens of MHz up to 1.8 GHz. Fig. 6.27a and b shows the optical spectra and the corresponding time trace at a modulation frequency of 240 MHz, respectively. The multi-mode optical spectrum indicates that there might be a double effect: the strong output coupler can lock the cavity modes of the SRL at the same time. Therefore it might well be that the pulses consist of a train of ultra-short pulses with a repetition rate equaling the round-trip time of the ring. Nevertheless, the lack of equipment prevented proper pulse characterization. It must be noted that only one coupler was modulated (such as shown for the LI curve in Fig. 6.24). Also, the measurements were carried out by collecting the light from the output waveguides that are coupled to the unbiased SRL output to avoid any additional output intensity modulation.

Fig. 6.28 shows the zoom-in of the time traces obtained at modulation frequencies of 240 MHz and 1.8 GHz. A minimum pulse-width value of 120 ps was obtained

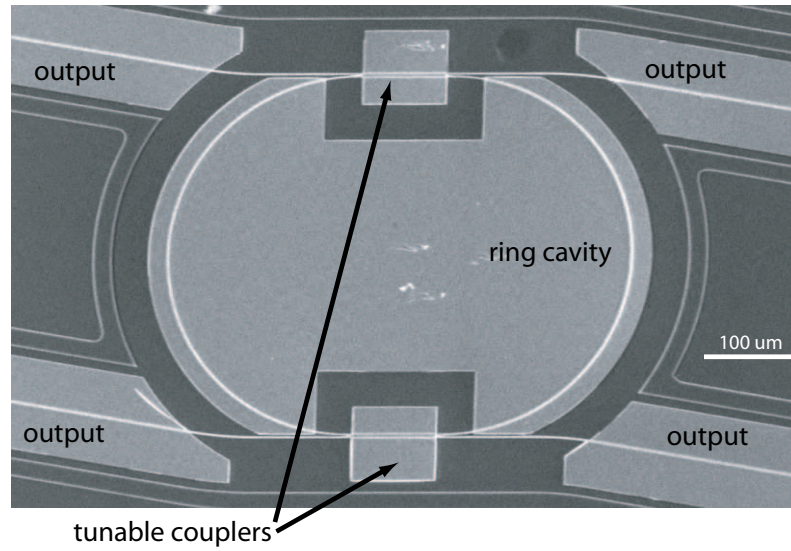


Figure 6.26: SEM image of the device, used for Q-switching experiments.

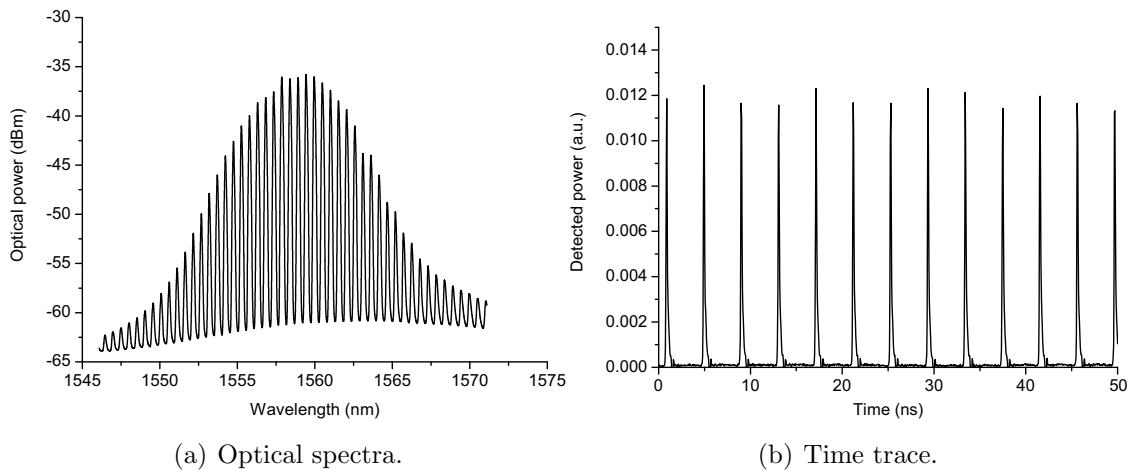


Figure 6.27: Optical spectra and time trace of 240 MHz switching

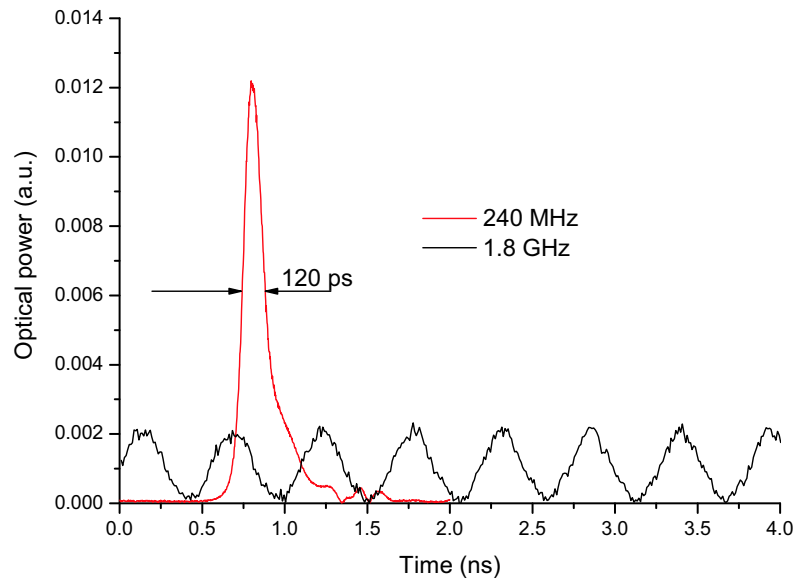


Figure 6.28: Time traces of Q-switching experiments.

at frequencies in the range 200–300 MHz. As expected, the energy of the pulses scales down with the increase of repetition frequency.

### 6.3.3 Applications

Tunable couplers alone can be regarded as electro-optic switches, however, the Mach-Zehnder interferometer is a more popular approach. Ring lasers with tunable output power could compete on the field of high-power lasers because their spectral purity, integrability and their power could be controlled with low currents. Furthermore – as seen earlier in this Section –, the optimal point of reflectance (coupling) value is current dependent. A high power laser with tunable coupler could be always tuned to provide the highest achievable power at a certain current. The possibility of tuning the cavity Q-factor can also be of great interest for controlling the linewidth of the lasing mode.

Q-switching is a popular technique for producing high energy pulses that finds applications in non-linear optics, sensing, spectroscopy. In fibre and solid-state lasers, the optical cavity can be actively Q-switched via an active control element that modulates the intra-cavity losses and thus the Q-factor of the cavity [100]. In semiconductor lasers, Q-switching is usually generated by placing a saturable absorber inside the lasing cavity. This technique, however, leads to the so called "passive Q-switching" or "self Q-switching" [101], where the pulse repetition rate

cannot be directly controlled. On the other hand, the tunable coupler approach provides an easy mechanism to damp the cavity of the SRL and to generate high energy pulses at any desired repetition rate by active Q-switching.

# Chapter 7

## Summary and conclusions

### 7.1 Summary and Conclusion

Design, technology development and characterization of SRL and SRL-based photonic integrated circuits were presented. A number of different coupling techniques as well as several device geometries were investigated and simulated: the racetrack geometry with evanescent field couplers proved to be the most promising because of the low intracavity perturbation, the design flexibility and the potential for tunability. Both simulations and measurements confirmed that the minimum size for shallow etched SRLs is limited to ring radii of  $150\ \mu\text{m}$  because of the bending losses.

The whole fabrication, consisting of more than sixty technological steps, was thoroughly optimized, with a major processing development being carried out in quantum well intermixing, electron beam lithography and dry etching. In particular, the developed dry etching technique allows for etching InP with a selectivity of over 30 against InAlAs. This provides a very precise control over the etching depth of the waveguides and minimizes the fabrication tolerances of evanescent field couplers. A reliable p-contact metallization process was developed, which ensures sidewall coverage and low resistance at the same time. The developed technology platform is now routinely used within the department for the fabrication of PICs with a yield of over 95%. Furthermore, lasers with the same size show only a few mA variance of threshold current with no measurable degradation or life-time problems.

A number of test devices and SRLs were fabricated and characterized to confirm and validate the design and simulation results. The measurements on half ring lasers showed a good agreement with the simulated figures for the bending losses, while measurements on directional couplers confirmed the robustness of the dry

etching process. Tunability of passive couplers was achieved either by injecting current or reverse biasing one of the waveguides of the coupler. Injecting a few mA of current (or applying a few V) results in tuning the coupling ratio from 100% down to a few percent. The characterization of SRLs showed the presence of a quite complicated mode dynamics, with some newly discovered operating regimes.

By investigating the high resolution spectra of SRLs, an explanation was given to the sudden mode jumps: this effect is originated by the weak filtering effect of the output waveguides. The effect of feedback on the modal properties was also investigated; even though, the fabricated SRLs possess world record high directional extinction ratios, stronger feedback can dramatically change the scenario and extinguish unidirectional operation. Furthermore, a new operational phenomenon, feedback induced mode-locking was observed for the first time. Despite the mode selection by the feedback from the output waveguides, it was also found that multiple wavelengths can stably lase in both directions.

Three examples of integrated devices were presented. An SRL+DFB configuration shows potential for integrated master-slave devices. Apart from the usual locking and chaotic regions, it was shown that when injecting into one of the side modes of the SRL, cavity enhanced four-wave mixing – up to detuning frequencies of 1.5 THz – was found for the first time. FWM also cascadingly locks several cavity modes of the SRL resulting in a narrow-linewidth electrical signal. Therefore, this configuration is a viable and promising option for high-frequency (in the THz range), narrow-linewidth (in the kHz range) signal generation in a step-tunable manner. Furthermore, unidirectional mode-locking (induced by FWM) is presented for the first time in semiconductor ring lasers.

Integrating a tunable Bragg reflector onto one of the output arms of an SRL resulted in a wavelength tunable device. The major novelty in the configuration is that the tuning element is not part of the lasing cavity and that the output wavelength is stably defined by the ring cavity modes that can be designed to any wavelength grid purely by lithography. The wavelength tuning is digital in a step-wise manner – only by changing a single current value –, and there is no need for a phase-matching section. The measurements showed a wavelength switching speed as low as 450 ps between consecutive cavity modes and an overall good thermal stability because the lasing wavelength is defined by the fixed-current pumped SRL and not by the tuning element. The configuration has some potential for realizing all-optical logical functions.

Integrating SRLs with tunable couplers provides an easy mechanism to damp the cavity of the SRL. This novel configuration allows high energy pulses generation

at any desired repetition rate by active Q-switching, which was demonstrated in semiconductor lasers for the first time. The realized device showed 180 ps pulses by applying only a few mA to the tunable coupler with speeds up to 1.8 GHz. The configuration is promising to generate high energy pulses for industrial applications or short pulses for telecommunication.

This work demonstrated that with careful technology development ring lasers can be fabricated in an integrated manner. Because of their inherent properties, SRLs can be integrated into devices with advanced functionalities, which can not be achieved otherwise.

## 7.2 Future work

This work provided a much better understanding of SRL operation, as well as a convincing demonstration on their potential for integration. However, on the device study side, there is a lot more to understand. In particular, the effect of the output waveguides and the coupling mechanisms on the device operation requires further investigations. The optical feedback, the intra-cavity reflections and the distributed waveguide scattering have a profound influence on the dynamics of the counter-propagating modes. Some additional work can be dedicated to investigating mode-locked operation of SRLs and to characterizing the emerging pulses. A number of SRLs with large cavity lengths (shown in Fig. 5.28) was already fabricated during this work and exhibited an extremely large mode-locking bandwidth in excess of 10 nm. Additional investigations should include:

- Traditional mode-locking with (one and two) saturable absorbers (pulse characterization in both directions).
- Mode-locking induced by feedback.
- Unidirectional mode-locking induced by FWM at the FSR frequency.
- Unidirectional mode-locking by FWM at multiples of the FSR frequency (18, 27, 36 GHz. . .).
- Mode-locking of an FP laser with absorber at one facet.
- Mode-locking of an FP laser with an absorber in the middle to achieve colliding pulse mode operation, similar to SRLs with saturable absorbers.

Furthermore, weak cavity filtering effects can lead to harmonic mode-locking which can be extended up to THz detuning frequencies [102].

Additional work could be dedicated to the SRL+DFB configuration: locking map of side-modes should be recorded to record a complete map on the FWM region (as a function of detuning and injection level). This would also provide the bandwidth of the FWM, while actual wavelength conversion with modulated signals could be also carried out.

On the SRL+DBR configuration, sampled grating technology should be developed to extend the tuning range. Another potential alternative to the tunable device is either coupling the ring to a short FP filter to achieve tunability or coupling two rings with similar size. The speed of the devices could be increased by designing contact shapes for high speed operation. The same applies to tunable coupler devices. Also the devices could be realized on the GaAs/AlGaAs material system to have high power devices whose power can be switched on or off just by injecting a few mA of current into the tunable coupler.

Most of the results achieved in this thesis constituted the framework for recently funded research grants and, hopefully, will be used to define future research activities. In the final year of this work, an EU-funded project called IOLOS started, with the objective of further studying SRL potential and realizing all-optical logical functions with micro-SRLs.

# Appendix A

## List of used materials

Table A.1: Material *3186*, a  $1.3\ \mu\text{m}$  wafer for fabrication assessment.

Thickness	Composition	Layer
200 nm	$\text{p}^+-\text{In}_{0.53}\text{Ga}_{0.47}\text{As}$	Cap layer
1650 nm	$\text{p}-\text{InP}$	Upper cladding
50 nm	$\text{In}_{0.52}\text{Al}_{0.48}\text{As}$	Electron confinement
50 nm	$\text{In}_{0.52}\text{Al}_{0.4}\text{Ga}_{0.08}\text{As}$	SCH
$6 \times 6$ nm	$\text{In}_{0.73}\text{Al}_{0.165}\text{Ga}_{0.105}\text{As}$	Strained QWs
$7 \times 10$ nm	$\text{In}_{0.52}\text{Al}_{0.36}\text{Ga}_{0.12}\text{As}$	Barriers
50 nm	$\text{In}_{0.52}\text{Al}_{0.4}\text{Ga}_{0.08}\text{As}$	SCH
50 nm	$\text{In}_{0.52}\text{Al}_{0.48}\text{As}$	Electron confinement
$\sim 600\ \mu\text{m}$	$\text{n}-\text{InP}$	Substrate

Table A.2: Structure of the 1.55  $\mu\text{m}$  wafers *2032*, *2254* and *2256* used for fabrication assessment and early results on ring lasers.

Thickness	Composition	Layer
200 nm	$\text{p}^+\text{-In}_{0.53}\text{Ga}_{0.47}\text{As}$	Cap layer
1400 nm	$\text{p-InP}$	Upper cladding
50 nm	$\text{In}_{0.52}\text{Al}_{0.48}\text{As}$	Electron confinement
80 nm	$\text{In}_{0.53}\text{Al}_{0.4}\text{Ga}_{0.07}\text{As}$	GRINSCH
$6 \times 7$ nm	$\text{In}_{0.53}\text{Ga}_{0.47}\text{As}$	Quantum wells
$5 \times 8$ nm	$\text{In}_{0.53}\text{Al}_{0.2}\text{Ga}_{0.27}\text{As}$	Barriers
80 nm	$\text{In}_{0.53}\text{Al}_{0.4}\text{Ga}_{0.07}\text{As}$	GRINSCH
50 nm	$\text{In}_{0.52}\text{Al}_{0.48}\text{As}$	Electron confinement
$\sim 350 \mu\text{m}$	$\text{p-InP}$	Substrate

## Appendix B

# Basic equations for semiconductor lasers

Three simple equations describe well the basic characteristics (threshold gain, slope efficiency and the relationship between gain and injected current) of a semiconductor laser [54]. The gain of a FP quantum well laser at threshold can be expressed as [103]:

$$n\Gamma_w g_{th} = \alpha_0 + \frac{1}{L} \ln \frac{1}{R}, \quad (\text{B.1})$$

where  $n$  is the number of quantum wells,  $\Gamma_w$  is the confinement factor per well,  $g_{th}$  is the gain at threshold,  $\alpha_0$  is the material loss,  $L$  is the cavity length and  $R$  is the reflectivity of the mirrors. The external quantum efficiency above threshold is:

$$\eta_{ext} = \eta_i \left( 1 - \frac{\alpha_0}{n\Gamma_w g_{th}} \right), \quad (\text{B.2})$$

where  $\eta_i$  is the internal quantum efficiency and the external quantum efficiency is defined by the  $\delta P/\delta I$  slope efficiency of the laser and the  $h\nu$  photon energy:

$$\eta_{ext} = \frac{2q}{h\nu} \left( \frac{\delta P}{\delta I} \right)_{I > I_{th}}. \quad (\text{B.3})$$

And finally, the relationship between the gain and the injected current can be approximated as

$$\frac{g_{th}}{g_0} = \ln \frac{J_{th}\eta_i}{J_t n}, \quad (\text{B.4})$$

where  $g_0$  and  $J_t$  are the gain factor and current density per quantum well, respectively.

Using Eqns. (1)–(4), one can also deduce that

$$\frac{1}{\eta_{ext}} = \frac{1}{\eta_i} - \left( \frac{\alpha}{\eta_i \ln(R)} \right) L \quad \text{and} \quad (\text{B.5})$$

$$\ln(J_{th}) = \ln(J_\infty) - \left( \frac{\ln(R)}{n\Gamma_w g_0} \right) \frac{1}{L}, \quad (\text{B.6})$$

where  $J_\infty$  is the threshold current density at infinite cavity length, and can be deduced as

$$\ln(J_\infty) = \frac{\alpha}{n\Gamma_w g_0} + \ln \frac{nJ_t}{\eta_i}. \quad (\text{B.7})$$

Eqns. (B.5) and (B.6) yield  $y = mx + b$  type linear relationships. The external quantum efficiency and the threshold current density can be measured as a function of the cavity length using broad area and ridge waveguide F–P lasers, while the confinement factor ( $\Gamma_w n$ ) and mirror reflectivity ( $R$ ) is usually known from simulation. These provide enough to calculate all the other parameters.

# Appendix C

## Measurements on the linewidth enhancement factor

The successful application of SRLs in real fiber optic transmission systems will also depend on the chirp introduced by the SRL during the switching operation. Therefore, the collaborating partners in Pavia carried out some measurements on the frequency response and the linewidth enhancement factor ( $\alpha$ -factor) on devices (with ring radii of  $150\ \mu\text{m}$  and coupler lengths of  $200\ \mu\text{m}$ ) which results are currently in publication [104], and are summarized here.

The measurements have been carried out using an all-optical modulation technique (i.e. injection of an external modulated laser into the SRL), because the SRL structure does not allow for direct current modulation up to high frequencies. Therefore, a tuneable external cavity laser was externally modulated by a Mach-Zehnder modulator, amplified by an L-band Erbium-doped fiber amplifier (EDFA), and injected into the SRL through an optical circulator and a lensed optical fibre. A 20 GHz electrical network analyzer was used to perform the frequency response measurement. The modulated light injected into the SRL generates a small signal modulation of the SRL carrier density and of the emitted optical power. The measured small-signal frequency response curves are shown in Fig. C.1 for varying injected current into the SRL.

For low currents, the response shows a clear resonance peak caused by relaxation oscillation, which gets damped and moves to higher frequencies as the current is increased. At 150 mA the RO are overdamped, and no resonance appears. In these conditions, the  $-3\ \text{dB}$  frequency is around 11 GHz. This value corresponds to a rise-time of 35 ps for a step-like transition. The question now arises about whether the SRL in the bistable regime used as all-optical Flip-Flop can really exhibit such

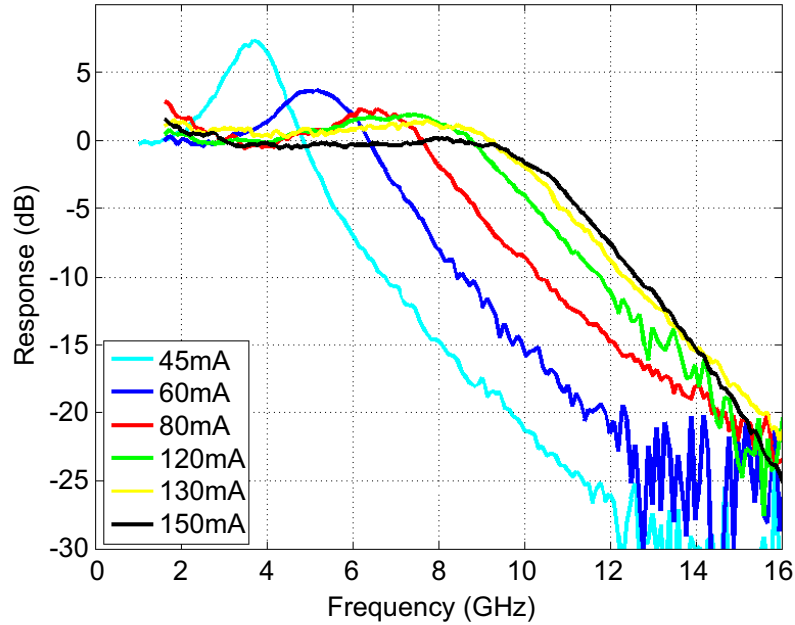


Figure C.1: Measured frequency response for varying SRL current.

a short switching time. In fact, the measured frequency response holds for small-signal modulation, whereas a complete directional switching in the bistable regime implies a large power variation. This is presently being investigated experimentally.

The same principle is used to measure the  $\alpha$ -factor, implementing a novel modified version of the fiber transfer function method (FTF) [105], where the carrier density modulation in the SRL is achieved by optical injection, similarly to the frequency response method described above. In this case, the modulated light was propagated along a DCF (Dispersion Compensating Fiber). Fitting to the results allows to extract the  $\alpha$ -factor. The measurement was repeated for different injection current values, and the results are summarized in Fig. C.2. The average value for the  $\alpha$ -factor is 2.4, and for higher currents the measured values are around 2.1. The low  $\alpha$  values are due to the intrinsic characteristics of the Al-quaternary material, and allow for a reduced chirp, favoring applications of the SRL device to fiber-optic transmission systems with reduced penalty due to frequency chirping.

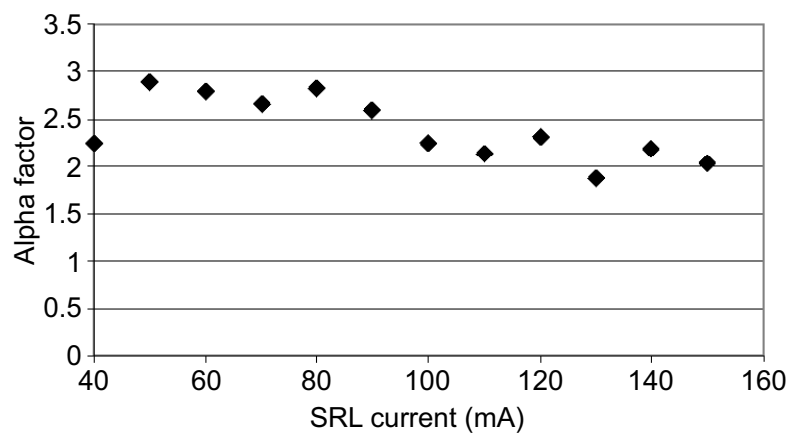


Figure C.2: Measured linewidth enhancement factor vs. SRL current

# Appendix D

## List of equipment used

### Chemicals

**Acetone:** dimethyl ketone,  $\text{CH}_3\text{COCH}_3$

**CW2400 conductive epoxy:** Chemtronics' two component silver epoxy

**HF:** hydrofluoric acid

**Hydrochloric acid:** aqueous solution of hydrogen chloride (HCl), strong acid

**Hydrogen peroxide:**  $\text{H}_2\text{O}_2$ , strong oxidizer

**IPA:** isopropyl alcohol

**MIBK:** Methyl isobutyl ketone, a solvent which develops PMMA after EBL

**OptiClear:** National Diagnostics wax, flux and grease removal solvent

**Orthophosphoric acid:**  $\text{H}_3\text{PO}_4$

**RO water:** water cleaned by reverse osmosis

**Sulphuric acid:**  $\text{H}_2\text{SO}_4$

### Resists

**HSQ:** hydrogen silsesquioxane, a spin-

on glass like negative tone electron-beam resist

**PMMA:** polymethylmethacrylate,  $(\text{C}_5\text{O}_2\text{H}_8)_n$ , positive electron-beam resist

**S1818:** Shipley positive photoresist

### Tools for fabrication

**BP80:** Plasma Technology's RIE machine mainly for etching  $\text{SiO}_2$  using fluorine chemistry

**EBPG5:** Vistec's (previously Leica) high resolution electron beam lithography tool

**ET340:** Electrotech's RIE machine using methane/hydrogen chemistry, used to etch InP

**JetFirst RTA:** Jipelec's rapid thermal annealing system

**MA6:** Karl Sss' mask aligner for UV lithography

**Plasmalab 80Plus:** PECVD tool used for depositing  $\text{SiO}_2$

*APPENDIX D. LIST OF EQUIPMENT USED*

---

**VB6:** Vistec's newest ultra-high resolution electron beam lithography tool      spectrum analyzer  
**Nd:YAG laser:** neodymium-doped yttrium aluminium garnet ( $\text{Nd:Y}_3\text{Al}_5\text{O}_{12}$ ) solid state laser

**Optical characterization equipment**

**Agilent OSA:** Agilents' 86140B optical

# Appendix E

## Acronyms

<b>AFM</b> atomic force microscope	<b>DER</b> directional extinction ratio
<b>APML</b> additive pulse mode-locking	<b>DFB</b> distributed feedback laser
<b>ARDE</b> aspect ratio dependent etching	<b>EDFA</b> Erbium-doped fiber amplifier
<b>ASE</b> amplified spontaneous emission	<b>EBL</b> electron beam lithography
<b>AWG</b> arrayed waveguide grating	<b>FP</b> Fabry-Perot
<b>BAL</b> broad area laser	<b>FSR</b> free spectral range
<b>CCD</b> charge-coupled device	<b>FTF</b> fiber transfer function method
<b>CCML</b> coupled-cavity mode-locking	<b>FWHM</b> full width at half maximum
<b>CCW</b> counter-clockwise	<b>FWM</b> four-wave mixing
<b>CDP</b> carrier density pulsation	<b>ICP</b> inductive coupled plasma
<b>CH</b> carrier heating	<b>MMI</b> multi-mode interference
<b>cw</b> continuous-wave	<b>MOCVD</b> metalorganic vapour phase epitaxy
<b>CW</b> clockwise	<b>OE</b> optical-electrical
<b>DBR</b> distributed Bragg reflector	<b>OSA</b> optical spectrum analyser
<b>DC</b> direct current	<b>PC</b> polarization control
	<b>PD</b> photo-detector

<b>PEC</b> proximity error correction	<b>SHB</b> spectral hole burning
<b>PECVD</b> plasma enhanced chemical vapor deposition	<b>SISA</b> selective intermixing in selective areas
<b>PIC</b> photonic integrated circuit	<b>SMSR</b> side mode suppression ratio
<b>PL</b> photoluminescence	<b>SOA</b> semiconductor optical amplifier
<b>QCSE</b> quantum confined Stark effect	<b>SPM</b> self-phase modulation
<b>QD</b> quantum dot	<b>SRL</b> semiconductor ring laser
<b>QW</b> quantum well	<b>SW</b> switch
<b>QWI</b> quantum well intermixing	<b>TE</b> transverse electric
<b>RBW</b> resolution bandwidth	<b>TEC</b> thermo-electric cooler
<b>RF</b> radio-frequency	<b>TLM</b> transmission line model
<b>RIE</b> reactive ion etching	<b>VCSEL</b> vertical-cavity surface-emitting laser
<b>RMS</b> real mean square	
<b>RWG</b> ridge wave-guide	<b>WDM</b> wavelength division multiplexing
<b>SEM</b> scanning electron microscope	

# Bibliography

- [1] D. R. Scifres, R. D. Burnham, and W. Streifer, “Grating-coupled GaAs single heterostructure ring laser,” *Applied Physics Letters* **28**(11), pp. 681–683, 1976.
- [2] N. Matsumoto and K. Kumabe, “AlGaAs-GaAs semiconductor ring laser,” *Japanese Journal of Applied Physics* **16**(8), pp. 1395–1398, 1977.
- [3] A. S.-H. Liao and S. Wang, “Half-ring (GaAl)As double-heterojunction injection lasers,” *Applied Physics Letters* **36**(5), pp. 353–356, 1980.
- [4] A. S.-H. Liao and S. Wang, “Semiconductor injection lasers with a circular resonator,” *Applied Physics Letters* **36**(10), pp. 801–803, 1980.
- [5] T. Krauss, P. Laybourn, and J. Roberts, “CW operation of semiconductor ring lasers,” *Electron. Lett.* **26**(25), pp. 2095–2097, 1990.
- [6] T. Krauss, R. M. DeLaRue, I. Gontijo, P. J. R. Laybourn, and J. S. Roberts, “Strip-loaded semiconductor ring lasers employing multimode interference output couplers,” *Applied Physics Letters* **64**(21), pp. 2788–2790, 1994.
- [7] T. Krauss, R. M. DeLaRue, and P. J. R. Laybourn, “Impact of output coupler configuration on operating characteristics of semiconductor ring lasers,” *Journal of Lightwave Technology* **13**(7), pp. 1500–1507, 1995.
- [8] T. F. Krauss, R. M. DeLaRue, P. J. R. Laybourn, B. Vogeleson, and C. R. Stanley, “Efficient semiconductor ring lasers made by a simple self-aligned fabrication process,” *IEEE Journal on Sel. Top. in Quantum Electronics* **1**(2), pp. 757–761, 1995.
- [9] J. P. Hohimer, D. C. Craft, G. R. Hadley, G. A. Vawter, and M. E. Warren, “Single-frequency continuous-wave operation of ring resonator diode lasers,” *Applied Physics Letters* **59**(26), pp. 3360–3362, 1991.

- [10] J. P. Hohimer, D. C. Craft, G. R. Hadley, and G. A. Vawter, “Cw room-temperature operation of y-junction semiconductor ring lasers,” *Electron. Lett.* **28**(4), pp. 374–375, 1992.
- [11] J. P. Hohimer and G. A. Vawter, “Unidirectional semiconductor ring lasers with racetrack cavities,” *Applied Physics Letters* **63**(18), pp. 2457–2459, 1993.
- [12] J. P. Hohimer, G. A. Vawter, D. C. Craft, and G. R. Hadley, “Improving the performance of semiconductor ring lasers by controlled reflection feedback,” *Applied Physics Letters* **61**(9), pp. 1013–1015, 1992.
- [13] J. P. Hohimer and G. A. Vawter, “Passive mode locking of monolithic semiconductor ring lasers at 86 GHz,” *Applied Physics Letters* **63**(12), pp. 1598–1600, 1993.
- [14] G. Vawter, A. Mar, V. Hietala, J. Zolper, and J. Hohimer, “All optical millimeter-wave electrical signal generation using an integrated mode-locked semiconductor ring laser and photodiode,” *IEEE Photon. Tech. Lett.* **9**(12), pp. 1634–1636, 1997.
- [15] H. Cao, H. Ling, C. Liu, H. Deng, M. Benavidez, V. Smagley, R. Caldwell, G. Peake, G. Smolyakov, P. Eliseev, and M. Osinski, “Large S-section-ring-cavity diode lasers: directional switching, electrical diagnostics, and mode beating spectra,” *IEEE Photon. Tech. Lett.* **17**(2), pp. 282–284, 2005.
- [16] A. Behfar-Rad, J. M. Ballantyne, and S. S. Wong, “Etched-facet AlGaAs triangular-shaped ring lasers with output coupling,” *Applied Physics Letters* **69**(12), pp. 1395–1397, 1991.
- [17] A. Behfar-Rad, J. M. Ballantyne, and S. S. Wong, “AlGaAs/GaAs-based triangular-shaped ring ridge lasers,” *Applied Physics Letters* **60**(14), pp. 1658–1660, 1992.
- [18] J. J. Liang, S. T. Lau, M. H. Leary, and J. M. Ballantyne, “Spatial beam switching and bistability in a diode ring laser,” *Applied Physics Letters* **70**(10), pp. 1192–1194, 1997.
- [19] M. F. Booth, A. Schremer, and J. M. Ballantyne, “Spatial beam switching and bistability in a diode ring laser,” *Applied Physics Letters* **76**(9), pp. 1095–1097, 2000.

- [20] S. Yu, T. F. Krauss, and P. J. R. Laybourn, “Mode locking in large monolithic semiconductor ring lasers,” *Optical Engineering* **37**(4), pp. 1164–1168, 1998.
- [21] M. Sorel, P. J. R. Laybourn, and S. D. G. Giuliani, “Control of unidirectional operation in semiconductor ring lasers,” in *The 14th Annual Meeting of the IEEE LEOS*, (San Diego, CA, USA), 12–13 November 2001.
- [22] M. Sorel, P. J. R. Laybourn, A. Scir, S. Balle, G. Giuliani, R. Miglierina, and S. Donati, “Alternate oscillations in semiconductor ring lasers,” *Optics Letters* **27**(22), pp. 1992–1994, 2002.
- [23] M. Sorel, P. J. R. Laybourn, G. Giuliani, and S. Donati, “Unidirectional bistability in semiconductor waveguide ring lasers,” *Applied Physics Letters* **80**(17), pp. 3051–3053, 2002.
- [24] M. Sorel, G. Giuliani, A. Scire, R. Miglierina, S. Donati, and P. Laybourn, “Operating regimes of GaAs-AlGaAs semiconductor ring lasers: experiment and model,” *IEEE Journal of Quantum Electronics* **39**(10), pp. 1187–1195, 2003.
- [25] R. van Roijen, E. C. M. Pennings, M. J. N. van Stalen, T. van Dongen, B. H. Verbeek, and J. M. M. van der Heijden, “Compact InP-based ring lasers employing multimode interference couplers and combiners,” *Applied Physics Letters* **64**(14), pp. 1753–1755, 1994.
- [26] J. den Besten, R. Broeke, M. van Geemert, J. Binsma, F. Heinrichsdorff, T. van Dongen, T. de Vries, E. Bente, X. Leijtens, and M. Smit, “A compact digitally tunable seven-channel ring laser,” *IEEE Photon. Tech. Lett.* **12**(6), pp. 753–755, 2002.
- [27] E. Bente, Y. Barbarin, J. den Besten, M. Smit, and J. Binsma, “Wavelength selection in an integrated multiwavelength ring laser,” *IEEE Journal of Quantum Electronics* **40**(9), pp. 1208–1216, 2004.
- [28] M. T. Hill, H. J. S. Dorren, T. de Vries, X. J. M. Leijtens, J. H. den Besten, B. Smalbrugge, Y.-S. Oei, H. Binsma, G.-D. Khoe, and M. K. Smit, “A fast low-power optical memory based on coupled micro-ring lasers,” *Nature* **432**, pp. 206–209, Nov. 2004.
- [29] Y. Barbarin, S. Anantathanasarn, E. A. J. M. Bente, Y. S. Oei, M. K. Smit, and R. Notzel, “1.55- $\mu\text{m}$  range InAs-InP (100) quantum-dot Fabry-Pérot

- and ring lasers using narrow deeply etched ridge waveguides,” *IEEE Photon. Tech. Lett.* **18**(24), pp. 2644–2646, 2006.
- [30] K. M. Dzurko, D. R. Scifres, A. Hardy, D. F. Welch, and R. G. Waarts, “Single mode broad area distributed bragg reflector ring oscillators,” *Applied Physics Letters* **61**(20), pp. 2389–2391, 1992.
- [31] H. Han, M. Favaro, D. Forbes, and J. Coleman, “ $\text{In}_x\text{Ga}_{1-x}\text{As}-\text{Al}_y\text{Ga}_{1-y}\text{As}-\text{GaAs}$  strained-layer quantum-well heterostructure circular ring lasers,” *IEEE Photon. Tech. Lett.* **4**(8), pp. 817–819, 1992.
- [32] H. Han, D. Forbes, and J. Coleman, “InGaAs-AlGaAs-GaAs strained-layer quantum-well heterostructure square ring lasers,” *IEEE Journal of Quantum Electronics* **31**(11), pp. 1994–1997, 2003.
- [33] P. Hansen, G. Raybon, M.-D. Chien, U. Koren, B. Miller, M. Young, J.-M. Verdiell, and C. Burrus, “A 1.54- $\mu\text{m}$  monolithic semiconductor ring laser: CW and mode-locked operation,” *IEEE Photon. Tech. Lett.* **4**(5), pp. 411–413, 1992.
- [34] H. S. Kim, Y. S. Kwon, and S. Hong, “Square ring laser diode with MMI coupler cavity,” *IEEE Photon. Tech. Lett.* **9**(5), pp. 584–586, 1997.
- [35] G. Griffel, J. H. Abeles, R. J. Menna, A. M. Braun, J. C. Connolly, and M. King, “Low-threshold InGaAsP ring lasers fabricated using bi-level dry etching,” *IEEE Photon. Tech. Lett.* **12**(2), pp. 146–148, 2000.
- [36] T. Higashi, S. J. Sweeney, A. F. Phillips, A. R. Adams, E. P. O’Reilly, T. Uchida, and T. Fujii, “Observation of reduced nonradiative current in 1.3  $\mu\text{m}$  AlGaInAs–InP strained MQW lasers,” *IEEE Photon. Tech. Lett.* **11**(4), pp. 409–411, 1999.
- [37] “1550 nm laser diode epiwafers.” <http://www.iqep.com/pdfs/1550nmLD.pdf>, 9.25am, 19 July 2007.
- [38] T. Mei, “Interpolation of quaternary III-V alloy parameters with surface bowing estimations,” *Journal of Applied Physics* **101**, pp. 013520 1–6, 2007.
- [39] S. Fürst, C. Farmer, L. Hobbs, R. DeLaRue, and M. Sorel, “Native oxidation of aluminum-containing III-V compound layers for increased current and optical confinement in semiconductor lasers,” in *The 19th Annual Meeting of the IEEE LEOS*, (Montreal, Canada), 28 October – 3 November 2006.

- [40] H. Y. Wong, M. Sorel, A. C. Bryce, J. H. Marsh, and J. M. Arnold, “Monolithically Integrated InGaAs–AlGaInAs Mach-Zehnder Interferometer Optical Switch Using Quantum-Well Intermixing,” *IEEE Photon. Tech. Lett.* **17**(4), pp. 783–785, 2005.
- [41] P. K. Tien, “Light waves in thin films and integrated optics,” *Applied Optics* **10**(11), pp. 2395–2404, 1971.
- [42] R. J. Deri and E. Kapon, “Low loss III-V semiconductor optical waveguides,” *IEEE Journal of Quantum Electronics* **27**(3), pp. 626–640, 1991.
- [43] F. P. Payne and J. P. R. Lacey, “A theoretical analysis of scattering loss from planar optical waveguides,” *Optical and Quantum Electronics* **26**, pp. 977–986, 1994.
- [44] W. S. Hobson, F. Ren, U. Mohideen, R. E. Slusher, M. L. Schnoes, and S. J. Pearton, “Silicon nitride encapsulation of sulfide passivated GaAs/AlGaAs microdisk lasers,” *Journal of Vacuum Science Technology* **13**, pp. 642–645, 1995.
- [45] M. Sorel, G. Giuliani, A. Scirè, R. Miglierina, S. Donati, and P. J. R. Laybourn, “Operating regimes of GaAs–AlGaAs semiconductor ring lasers: Experiment and model,” *IEEE Journal of Quantum Electronics* **39**(10), pp. 1187–1195, 2003.
- [46] M. Sorel, P. J. R. Laybourn, G. Giuliani, and S. Donati, “Unidirectional bistability in semiconductor waveguide ring lasers,” *Applied Physics Letters* **80**(17), pp. 3051–3053, 2002.
- [47] D. L. Lee, *Electromagnetic principles of integrated optics*, Wiley, New York, 1986.
- [48] D. Yanson, M. Silver, G. Masterton, O. Vassalli, M. Campbell, S. McDougall, and J. Marsh, “Technology development for photonic integration in InP,” in *International Conference on Indium Phosphide and Related Materials*, pp. 512–515, (Glasgow, UK), 8–12 May 2005.
- [49] M. Guden and J. Piprek, “Material parameters of quaternary III-V semiconductors for multilayer mirrors at 1.55  $\mu\text{m}$  wavelength,” *Modelling Simul. Mater. Sci. Eng.* **4**, pp. 349–357, 1996.

- [50] D. A. B. Miller, D. S. Chemla, T. C. Damen, A. C. Gossard, W. Wiegmann, T. H. Wood, and C. A. Burrus, “Electric field dependence of optical absorption near the band gap of quantum-well structures,” *Phys. Rev. B* **32**(2), pp. 1043–1060, 1985.
- [51] J.-I. Shim, M. Yamaguchi, P. Delansay, and M. Kitamura, “Refractive index and loss changes produced by current injection in InGaAs(P)-InGaAsP multiple quantum-well (MQW) waveguides,” *IEEE Journal on Sel. Top. in Quantum Electronics* **1**(2), pp. 408–415, 1995.
- [52] F. Hernandez-Gil, T. L. Koch, U. Koren, R. P. Gnall, and C. A. Burrus, “Tunable MQW-DBR laser with monolithically integrated GaInAsP/InP directional coupler switch,” *Electron. Lett.* **25**(19), pp. 1271–1272, 1989.
- [53] R. F. Nabiev, D. Francis, and C. J. Chang-Hasnain, “Lateral and Longitudinal Mode Discrimination in Index-Guided Circular Ring Semiconductor Lasers,” *IEEE Photon. Tech. Lett.* **5**(9), pp. 975–978, 1993.
- [54] H. Y. Wong, *InGaAs/InAlGaAs Monolithically Integrated Mach-Zender Interferometer Devices*. PhD Thesis, Department of Electronics and Electrical Engineering, University of Glasgow, 2005.
- [55] H. Abe, S. G. Ayling, J. H. Marsh, and R. M. DeLaRue, “Single-mode operation of surface grating distributed feedback GaAs-AlGaAs laser with variable-width waveguide,” *IEEE Photon. Tech. Lett.* **7**(5), 1995.
- [56] J. Wiedmann, K. Ebihara, H. Kim, B. Chen, M. Ohta, K. Matsui, S. Tamura, J.-I. Shim, and S. Arai, “1.5  $\mu\text{m}$  wavelength distributed reflector lasers with vertical grating,” *Electron. Lett.* **37**(13), pp. 831–832, 2001.
- [57] D. Roberts, J. Roberts, C. Button, M. Pate, G. Hill, P. Claxton, and P. Robson, “Aspects of selective area epitaxy and their application to integrated optics,” *Integrated Optics, IEE Colloquium on* , pp. 7/1–7/6, 1989.
- [58] V. Aimez, J. Beauvais, J. Beerens, D. Morris, H. Lim, and B.-S. Ooi, “Low-energy ion-implantation-induced quantum-well intermixing,” *IEEE Journal on Sel. Top. in Quantum Electronics* **8**(4), pp. 870–879, 2002.
- [59] H. S. Djie, T. Mei, J. Arokiaraj, and D. Nie, “Single step quantum well intermixing with multiple band gap control for III-V compound semiconductors,” *Journal of Applied Physics* **96**(6), pp. 3282–3285, 2004.

- [60] M. Cohen, H. Tan, C. Jagadish, and R. Cohen, “Al<sub>x</sub>O<sub>y</sub> induced intermixing in GaAs/AlGaAs quantum wells,” *Lasers and Electro-Optics Society 1999 12th Annual Meeting. LEOS '99. IEEE* **2**, pp. 433–434, 1999.
- [61] O. P. Kowalski, C. J. Hamilton, S. D. McDougall, J. H. Marsh, A. C. Bryce, R. M. DeLaRue, B. Vögele, C. R. Stanley, C. C. Button, and J. S. Roberts, “A universal damage induced technique for quantum well intermixing,” *Applied Physics Letters* **72**(5), pp. 581–583, 1998.
- [62] Y. P. Varshni, “Temperature dependence of the energy gap in semiconductors,” *Physica* **34**, p. 149, 1967.
- [63] B. S. Ooi, K. McIlvaney, M. W. Street, A. S. Helmy, S. G. Ayling, A. C. Bryce, J. H. Marsh, and J. S. Roberts, “Selective quantum-well intermixing in GaAs-AlGaAs structures using impurity-free vacancy diffusion,” *IEEE Journal of Quantum Electronics* **33**(10), pp. 1784–1793, 1997.
- [64] S. Park, S.-S. Kim, L. Wang, and S.-T. Ho, “InGaAsP-InP nanoscale waveguide-coupled microring lasers with submilliampere threshold current using Cl<sub>2</sub>-N<sub>2</sub>-based high-density plasma etching,” *IEEE Journal of Quantum Electronics* **41**(3), pp. 351–356, 2005.
- [65] R. Grover, J. V. Hryniewicz, O. S. King, and V. Van, “Process development of methane–hydrogen–argon-based deep dry etching of InP for high aspect-ratio structures with vertical facet-quality sidewalls,” *J. Vac. Sci. Technol. B* **19**(5), pp. 1694–1698, 2001.
- [66] M. B. Stern and P. F. Liao, “Reactive ion etching of gaas and inp using sicl<sub>4</sub>,” *J. Vac. Sci. Technol. B* **1**(4), pp. 1053–1055, 1983.
- [67] M. M. Raj, J. Wiedmann, S. Toyoshima, Y. Saka, K. Ebihara, and S. Arai, “High-reflectivity semiconductor/benzocyclobutene bragg reflector mirrors for GaInAsP/InP lasers,” *Journal of Applied Physics* **40**, pp. 2269–2277, 2001.
- [68] J. E. Schramm, D. I. Babić, E. L. Hu, J. E. Bowers, and J. L. Merz, “Fabrication of high-aspect-ratio InP-based vertical-cavity laser mirrors using CH<sub>4</sub>/H<sub>2</sub>/O<sub>2</sub>/Ar reactive ion etching,” *J. Vac. Sci. Technol. B* **15**(6), pp. 2031–2036, 1997.

- [69] S. K. Murad, S. P. Beaumont, M. Holland, and C. D. W. Wilkinson, “Selective reactive ion etching of InGaAs and InP over InAlAs in  $\text{SiCl}_4/\text{SiF}_4/\text{HBr}$  plasmas,” *J. Vac. Sci. Technol. B* **13**(6), pp. 2344–2349, 1995.
- [70] K. Shinoda, K. Nakahara, and H. Uchiyama, “InGaAlAs/InP ridge-waveguide lasers fabricated by highly selective dry etching in  $\text{CH}_4/\text{H}_2/\text{O}_2$  plasma,” in *International Conference Indium Phosphide and Related Materials*, pp. 550–553, (Santa Barbara, CA, United States), May 12–16 2003.
- [71] A. Katz, B. E. Weir, and W. C. Dautremont-Smith, “Au/pt/ti contacts to p-In<sub>0.53</sub>Ga<sub>0.47</sub>As and n-InP layers formed by a single metallization common step and rapid thermal processing,” *Journal of Applied Physics* **68**(3), pp. 1123–1128, 1990.
- [72] C. Henry, “Theory of the linewidth of semiconductor lasers,” *IEEE Journal of Quantum Electronics* **18**(2), pp. 259–264, 1982.
- [73] M. Sargent, “Theory of a multimode quasiequilibrium semiconductor laser,” *Phys. Rev. A* **48**, pp. 717–726, Jul 1993.
- [74] R. J. C. Spreeuw, R. C. Neelen, N. J. van Druten, E. R. Eliel, and J. P. Woerdman, “Mode coupling in a he-ne ring laser with backscattering,” *Phys. Rev. A* **42**, pp. 4315–4324, Oct 1990.
- [75] C. Born, M. Sorel, and S. Yu, “Linear and nonlinear mode interactions in a semiconductor ring laser,” *IEEE Journal of Quantum Electronics* **41**(3), pp. 261–271, 2005.
- [76] S. Furst, A. Perez, A. Scire, S. Balle, and M. Sorel, “Modal structure, directional and wavelength jumps of integrated semiconductor ring lasers: Experiment and theory,” *submitted to Applied Physics Letters*, 2008.
- [77] E. D’Angelo, E. Izaguirre, G. B. Mindlin, G. Huyet, L. Gil, and J. Tredicce, “Spatiotemporal dynamics of lasers in the presence of an imperfect  $\text{O}(2)$  symmetry,” *Phys. Rev. Lett.* **68**(25), pp. 3702–3705, 1992.
- [78] J. Mulet, J. Javaloyes, and S. Balle, “Mode-locking of VECSELs by crossed-polarization gain modulation,” *IEEE Journal of Quantum Electronics* **43**(9), pp. 786–793, 2007.

- [79] E. P. Ippen, H. A. Haus, and L. Y. Liu, “Additive pulse mode locking,” *J. Opt. Soc. Am. B* **6**(9), p. 1736, 1989.
- [80] R. Lang, “Injection locking properties of a semiconductor laser,” *IEEE Journal of Quantum Electronics* **18**(6), pp. 976–983, 1982.
- [81] H. Soto and D. Erasme, “Identification of the nonlinear effects involved in a four-wave mixing experiment in a semiconductor optical amplifier,” *Summaries of papers presented at the Conference on Lasers and Electro-Optics, 1998. CLEO 98. Technical Digest.*, pp. 168–169, 3-8 May 1998.
- [82] H. Kasuya, M. Mori, R. Goto, T. Goto, and K. Yamane, “All optical mode locking of Fabry–Perot laser diode via mutual injection locking between two longitudinal modes,” *Applied Physics Letters* **75**(1), pp. 13–15, 1999.
- [83] H. Kuwatsuka, H. Shoji, M. Matsuda, and H. Ishikawa, “THz frequency conversion using nondegenerate four-wave mixing process in a lasing long-cavity  $\lambda/4$ -shifted DFB laser,” *Electron. Lett.* **31**(24), pp. 2108–2110, 1995.
- [84] A. Mecozzi, “Analytical theory of four-wave mixing in semiconductor amplifiers,” *Optics Letters* **19**(12), p. 892, 1994.
- [85] V. Annovazzi-Lodi, A. Scire, M. Sorel, and S. Donati, “Dynamic behavior and locking of a semiconductor laser subjected to external injection,” *IEEE Journal of Quantum Electronics* **34**(12), pp. 2350–2357, 1998.
- [86] S. M. Masahiko Tani, Osamu Morikawa and M. Hangyo, “Generation of terahertz radiation by photomixing with dual- and multiple-mode lasers,” *Semicond. Sci. Technol.* **20**(7), pp. S151–S163, 2005.
- [87] C. Walton, A. C. Bordonalli, and A. J. Seeds, “High-performance heterodyne optical injection phase-lock loop using wide linewidth semiconductor lasers,” *IEEE Photon. Tech. Lett.* **10**(3), pp. 427–429, 1998.
- [88] L. A. Johansson and A. J. Seeds, “Millimeter-wave modulated optical signal generation with high spectral purity and wide-locking bandwidth using a fiber-integrated optical injection phase-lock loop,” *IEEE Photon. Tech. Lett.* **12**(6), pp. 690–692, 2000.
- [89] S. Hoffmann, M. Hofmann, E. Brundermann, M. Havenith, M. Matus, J. V. Moloney, A. S. Moskalenko, M. Kira, S. W. Koch, S. Saito, and K. Sakai,

- “Four-wave mixing and direct terahertz emission with two-color semiconductor lasers,” *Applied Physics Letters* **84**(18), pp. 3585–3587, 2004.
- [90] S. Yoo, “Wavelength conversion technologies for wdm network applications,” *Journal of Lightwave Technology* **14**(6), pp. 955–966, 1996.
- [91] F. Morichetti, A. Melloni, A. Breda, A. Canciamilla, C. Ferrari, and M. Martinelli, “A reconfigurable architecture for continuously variable optical slow-wave delay lines,” *Optics Express* **15**(25), pp. 17273–17282, 2007.
- [92] V. Annovazzi-Lodi, S. Donati, and A. Scire, “Synchronization of chaotic injected-laser systems and its application to optical cryptography,” *IEEE Journal of Quantum Electronics* **32**(6), pp. 953–959, 1996.
- [93] T. Nakura and Y. Nakano, “LAPAREX—An automatic parameter extraction program for gain- and index-coupled distributed feedback semiconductor lasers, and its application to observation of changing coupling coefficients with currents,” *IEICE Trans. Electron.* **E83-C**(3), pp. 488–495, 2000.
- [94] F. Pozzi, R. M. De La Rue, and M. Sorel, “Dual-wavelength InAlGaAs-InP laterally coupled distributed feedback laser,” *IEEE Photon. Tech. Lett.* **18**(24), pp. 2563–2565, 2006.
- [95] L. A. Coldren, G. A. Fish, Y. Akulova, J. S. Barton, L. Johansson, and C. W. Coldren, “Tunable semiconductor lasers: A tutorial,” *Journal of Lightwave Technology* **22**(1), pp. 193–203, 2004.
- [96] D. Reid, D. Robbins, A. Ward, N. Whitbread, P. Williams, G. Busico, A. Carter, A. Wood, N. Carr, J. Asplin, M. Kearley, W. Hunt, D. Brambley, and J. Rawsthorne, “A novel broadband DBR laser for DWDM networks with simplified quasi-digital wavelength selection,” *Optical Fiber Communication Conference and Exhibit, 2002. OFC 2002*, 17-22 Mar 2002.
- [97] S. Matsuo, S.-H. Jeong, T. Segawa, H. Okamoto, Y. Kawaguchi, Y. Kondo, H. Suzuki, and Y. Yoshikuni, “Stable and fast wavelength switching in digitally tunable laser using chirped ladder filter,” *IEEE Journal on Sel. Top. in Quantum Electronics* **13**(5), pp. 1122–1128, 2007.
- [98] S. Yu, Z. Wang, G. Giuliani, S. Furst, and M. Sorel, “Optically triggered monostable and bistable flip-flop operation of monolithic semiconduc-

- tor ring laser,” in *Photonics in Switching*, (San Francisco, CA, USA), 19–22 Aug. 2007.
- [99] M. Pantouvaki, C. Renaud, P. Cannard, M. Robertson, R. Gwilliam, and A. Seeds, “Fast tuneable InGaAsP DBR laser using quantum-confined Stark-effect-induced refractive index change,” *IEEE Journal on Sel. Top. in Quantum Electronics* **13**(5), pp. 1112–1121, 2007.
- [100] B. T. Hansson and A. T. Friberg, “Eye-safe actively q-switched microchip laser with an electro-absorbing semiconductor modulator,” *Optics Letters* **26**(14), pp. 1057–1059, 2001.
- [101] P. Gavrilovic, N. Stelmakh, J. Zarrabi, and D. Beyea, “High energy CW Q-switched operation of multicontact semiconductor laser,” *Electron. Lett.* **31**(14), pp. 1154–1155, 1995.
- [102] E. Avrutin, J. Marsh, J. Arnold, T. Krauss, H. Pottinger, and R. De la Rue, “Analysis of harmonic (sub) THz passive mode-locking in monolithic compound cavity Fabry-Perot and ring laser diodes,” *Optoelectronics, IEE Proceedings -* **146**(1), pp. 55–61, 1999.
- [103] P. W. A. Mc Ilroy, A. Kurobe, and Y. Uematsu, “Analysis and application of theoretical gain curves to the design of multi-quantum-well lasers,” *IEEE Journal of Quantum Electronics* **QE-21**, pp. 1958–1963, 1985.
- [104] M. Zanola, G. Mezosi, S. Fürst, M. Sorel, and G. Giuliani, “Dynamic characterization of semiconductor ring lasers: Frequency response and linewidth enhancement factor,” in *submitted to International Semiconductor Laser Conference*, (Sorrento, Italy), 14–18 Sept. 2008.
- [105] R. Srinivasan and J. Cartledge, “On using fiber transfer functions to characterize laser chirp and fiber dispersion,” *IEEE Photon. Tech. Lett.* **7**(11), pp. 1327–1329, 1995.